STUDIES AND EXPERIMENTS ON EFFECT OF ATMOSPHERIC CHANGE DURING FREE SPACE OPTICS (FSO) COMMUNICATION USING LASERs

A thesis submitted towards partial fulfilment of the requirements for the degree of

Master of Technology in Laser Technology

Course affiliated to Faculty of Engineering and Technology and offered by
Faculty Council of Interdisciplinary Studies, Law and Management,
Jadavpur University

submitted by

SUJOY PAUL
Examination Roll No. - M4LST22009
Registration No. - 154564 of **2020-2021**

Under the guidance of

Prof. (Dr.) Saswati Mazumdar
Department of Electrical Engineering
Jadavpur University, Kolkata – 700032

School of Laser Science and Engineering

Faculty Council of Interdisciplinary Studies, Law and Management

Jadavpur University

Kolkata – 700032

2022

Jadavpur University
Faculty of Engineering and Technology
offered by Faculty Council of Interdisciplinary Studies, Law and Management

CERTIFICATE OF RECOMMENDATION

This is to certify that the thesis entitled "**STUDIES AND EXPERIMENTS ON EFFECT OF ATMOSPHERIC CHANGE DURING FREE SPACE OPTICS (FSO) COMMUNICATION USING LASERs**" submitted by **SUJOY PAUL, (Examination Roll No.M4LST22009, Registration No.154564 of 2020-2021)** of this University in partial fulfilment of requirements for the award of degree of Master Of Technology in School of Laser Science & Engineering, Department of Mechanical Engineering, is a bonafide record of the work carried out by his under our guidance and supervision during the academic session 2021-2022.

………………………………………...

(Thesis Supervisor)
Prof.(Dr.) Saswati Mazumdar
Professor
Electrical Engineering Department
Jadavpur University
Kolkata – 700032

………………………………….…

Prof.(Dr.)Dipten Misra
Director
School of Laser Science and Engineering
Jadavpur University, Kolkata – 700032

………………………….……….

Dean
FISLM/FET
Jadavpur University, Kolkata – 700032

Jadavpur University
Faculty Council of Interdisciplinary Studies, Law and Management

CERTIFICATE OF APPROVAL

This foregoing thesis is hereby approved as a creditable study of an engineering subject, carried out and presented by SUJOY PAUL, in a manner of satisfactory warrant its acceptance as a pre-requisite to the degree for which it has been submitted. It is notified to be understood that by this approval, the undersigned do not necessarily endorse or approved the thesis only for the purpose for which it has been submitted.

FINAL EXAMINATION FOR EVALUTION OF THESIS

BOARD OF EXAMINERS

………………………………………

.…………………………………..…

………………………………………

………………………………………

(Signature of Examiners)

DECLARATION OF ORIGINALITY AND COMPLIANCE OF ACADEMIC ETHICS

I hereby declares that this thesis contains original research work by the undersigned candidate, as part of my **Master of Technology** in **Laser Science and Engineering** studies during academic session 2021-2022.

All information in this documents has been obtained and presented in accordance with academic rules and ethical conduct.

I also declare that, as required by this rules and conduct, I have fully cited and referred all material and results that are not original to this work.

NAME : SUJOY PAUL

EXAMINATION ROLL NO. : M4LST22009

THESIS TITLE : "STUDIES AND EXPERIMENTS ON EFFECT OF ATMOSPHERIC CHANGE DURING FREE SPACE OPTICS (FSO) COMMUNICATION USING LASERs"

SIGNATURE WITH DATE :

ACKNOWLEDGEMENT

I would like to take this opportunity to humbly express my gratitude for innumerable gesture of help, cooperation and inspiration that I have received from my teachers, friends and well-wishers during this course.

I fill honoured to express my profound regard and deep sense of gratitude to my guide **Prof. (Dr.) SASWATI MAZUMDAR,** Head of the Department, Electrical Engineering Department, Jadavpur University, Kolkata, for allowing me to do my work in this exciting field. She has been person to in still in me a sense commitment, dedication and optimism. I am very much obliged for her continuous guidance and support throughout this thesis.

I express my sincere gratitude to **Prof. (Dr.) DIPTEN MISRA**, Director, School of Laser Science and Engineering, Jadavpur University, for his proper guidance for sending me to Electrical Engineering Department and support throughout this thesis.

I would like to acknowledge project **Free Space Laser Communication for Data & Voice (FSLCDV)** sponsored by Defence Research and Development Organisation (DRDO), India, in Electrical Engineering Department, Jadavpur University for using the project stuff.

I would like to give special thanks to **Mr. SHIBABRATA MUKHERJEE** and **Mr. BASUDEB DAS** research scholars, Jadavpur University for their spontaneous support and inspiration to carrying out this work.

I give my special thanks to **Mr. SAYAN MISTRY**, M.E. scholar, who helped me directly in completing my thesis successfully.

Last but not the least, I wish convey my gratitude to my parents, all of my friends, whose support and guidance have brought me this far.

Date :

Place : Jadavpur University
Kolkata – 700032

………………………………..
SUJOY PAUL

Content Table

List of Figures

Chapter 6

Chapter 1 – INTRODUCTION

1.1. General Introduction

In the last ten years, the amount of traffic carried by telecommunications networks, especially wireless networks, has grown significantly. The need for more innovation, research, and development in the new, developing communication technologies capable of providing extremely high data rates has been driven by the steadily rising demand for broadband internet services. One of the biggest success stories in the history of technology development is the creation of wireless technologies, which made it possible for people to communicate at any time and from any place. When it comes to services, wireless data and mobile internet have replaced voice communications as the main option, replacing them with considerably richer multimedia material, than anybody could have anticipated ten years ago. Already, the way we live, work, and socialise has been drastically altered by wireless gadgets, applications, and services. There is a huge increase in demand for mobile data transmission due to the development of new bandwidth-hungry apps. By 2020, mobile data traffic is anticipated to increase by three orders of magnitude over what it did in 2010, and the available spectrum for mobile services will almost double [1]. In the context of fifth generation (5G) wireless communication, this is also known as the mobile spectrum crunch, and it is being addressed [2-4]. The emerging idea of the Internet of Things (IoT), which has been most closely linked to machine-to-machine (M2M) communication, further wireless connectivity among naturally occurring and artificial object sensors, etc. in the environment realising ubiquitous machine-to-machine and machine-to-human communications. By doing so, wireless communications would become an integral part of daily life and further alter how we interact with the physical environment.

Due to radio frequency (RF) technologies' dominance in today's technology landscape, the term "wireless" is frequently used as a synonym for RF technologies. The radio frequency band is a portion of the electromagnetic spectrum that ranges from 30 kHz to 300 GHz, and both national and international agencies have tight regulations on its usage. Sub-bands are frequently leased solely to operators, such as mobile phone companies, television networks, and point-to-point microwave lines, among others. Due to an imbalance between the supply and demand for radio frequency wireless spectrum, a bottleneck or congestion has developed.

In high-density settings, multi-path effects in a congested urban environment cause user wireless communication systems (WCS) to perform worse on links, which leads to the emergence of such a situation. Given the bandwidth of these systems and the spectrum congestion, only a small number of HD channels can be supported in a given area. This issue is especially prevalent in applications that take place inside since there isn't enough bandwidth to accommodate all of the users. According to estimates, more than 70% of wireless traffic occurs inside, such as at homes, workplaces, and other indoor locations. Therefore, to provide a seamless indoor wireless communication system, low-cost and highly dependable technologies are needed.

There are just two options: using an alternative, such optical technology, or getting greater use out of radio frequency-based technologies. There are only three ways to enhance the capacity of wireless radio networks, regardless of the technology (such as 3G, 4G, 5G, or Wi-Fi) that are adopted:

I. release of a new spectrum and therefore more bandwidth,
II. more nodes,
III. eliminated of the interference, and
IV. highly improved frequency reuse of the available frequency resources.

Finding extra bandwidth is not a significant challenge, but it is obviously not enough because it is finite. Acquiring new spectrum is quite expensive. Cell splitting, which is a somewhat expensive method, might contain more nodes. Aside from that, interference problems prevent two nodes from providing double the capacity of one. Additionally, expanding the infrastructure won't increase income by that same amount. Finally, while wireless technology's spectrum efficiency has increased over time, it has recently slowed at less than 20%.

The optical wireless communication (OWC), which offers virtually an unlimited bandwidth (400THz) and includes infrared (IR), visible (VL), and ultraviolet (UV) sub-bands, is one potential complementary alternative technology that can address and overcome these limitations. This technology is shown in fig.1.1. Unique prospects that have so far mostly gone untapped are presented by the use of these bands for communications.

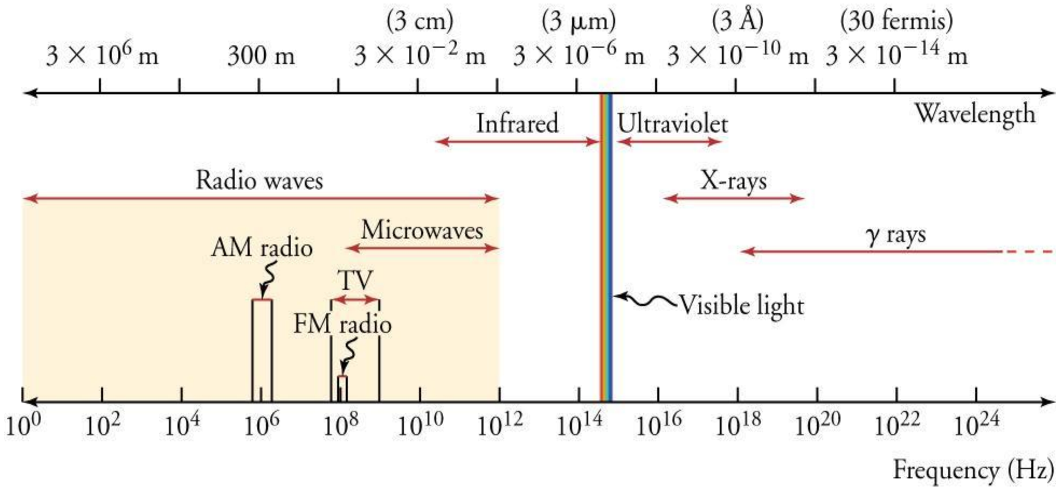

Fig.1.1. The electromagnetic spectrum

Optical wireless communication (OWC) [5,6] boasts superior characteristics to its radio frequency (RF) counterparts, including ultra-high bandwidth, robustness to electromagnetic interference, a high degree of spatial confinement bringing virtually unlimited frequency (or wavelength) reuse, and inherent physical security. Additionally, as OWC technologies may operate in the unlicensed spectrum, no licencing charge is necessary, making them a cost-effective choice for a variety of applications. For instance, instead of employing a high power RF based outside base station to deliver services in an indoor setting, a wireless link can considerably benefit from the high signal-to-noise ratio (SNR) supplied by the LED-based lighting room. Accordingly, under such situations, the appropriate course of action would be to deploy RF base stations to efficiently serve outside users, particularly fast-moving mobile users, and to use LED lights to serve interior slow-moving mobile users. This strategy has four essential qualities:

I. entirely avoiding the interference between the outdoor and indoor users,
II. with no interference, lower power RF base station, thus ‘greener’ mobile networks,
III. most effectively utilization of the scarce wireless transmission resources,
IV. improved user experience and reduced costs.

Since there are no radios or antennae in OWC systems, modulation and demodulation are direct, making the addition of extra nodes simple because they do not cause interference like in RF-based systems. With enough resources, OWC's spectrum efficiency is less sensitive, allowing for the adoption of techniques established for RF spectral efficiency. Path management is necessary when using higher frequencies in RF-based technologies to offer the required capacity, increasing the likelihood that OWC will be used under 'managed' circumstances. Although its variants dependent on the operating wavelength or frequency could have varied uses, as detailed in the following, the term OWC refers to any optical transmission in an unguided medium. Visible light communication is the term used to describe optical wireless communication (OWC) devices that operate in the visible band (390nm–780nm) (VLC). Both laser diodes and LEDs are used in VLC systems because they can be turned on and off at extremely fast speeds without having any discernible influence on the illumination output or the human eye. A sustainable and energy-efficient strategy that has the potential to alter how we use lighting in the future is the many uses of visible LEDs for illumination, data transfer, and indoor location. Wireless access point, wireless local area networks, wireless personal area networks, and vehicle networks are just a few of the many applications that VLC for data transfer may be employed in.

On the other side, near IR frequencies are used by terrestrial point-to-point OWC systems, sometimes referred to as free space optical (FSO) systems [7]. These technologies, which commonly employ laser transmitters, enable high data speeds (10Gbps per wavelength) via cost-effective protocol-transparent links and may be able to alleviate the backhaul bottleneck [8]. There have been reports of LED-based FSO systems where the data transfer rate via VLC is constrained and greatly relies on the environment. The property that is used for rough pointing, the visible light's irradiation angle, determines the transmission span. For satellite-based combinations, low bit rate free space data transfer utilising VLC has been accomplished without accurate pointing between the transmitter and receiver [9]. Similar to RF technology, FSO linkages in outdoor applications encounter a number of difficulties that will limit their widespread use. These difficulties are caused by atmospheric factors (such as fog, turbulence, and building sway), which will constantly impair the link's availability. Nevertheless, these issues can be solved by utilising hybrid FSO and RF radio communications. Despite having a number of field applications, this technology is mostly used outside. FSO may be utilised to offer high bandwidth connection in multi-point scenarios in indoor environments (i.e., large organisations). This is a fantastic way to bridge optical fibre connectivity across a number of places across wide areas without having to make significant infrastructure adaptations. In this regard, FSO may also present the finest options for upgrading and replacing fibre optic systems in contemporary structures. It might also have a big impact on another expanding area of study, radio-over-FSO, which has many characteristics with the well-known radio-over-fibre systems.

1.2. Literature Survey

The credibility of the experiment is derived by the utilization of the knowledge absorbed by reading following scientific journals, books and papers about free space optical (FSO) communication, attenuation, laser, link budget, and other parameters which are colossally important for the following experiment and findings.

Eswaravaka Mahesh Reddy *et al.* [10] described the demand on communication network as the increases for bandwidth change the scenario of the communication world and influenced the need of wireless communication and free space communication with increased bandwidth and other advantages over the frequently used normal fiber optics communication system. The scientific paper also discusses on some major systematic problems and parametric problems regarding free space optical communication which are not solved and improved, a proposal system of M-ary Quadrature Amplitude Modulation (MQAM) being used as to show which type of modulating way is beneficial for the outdoor environment and also for multiple users. The paper has also provided insight on the data transmission in longer distance as it shown less loss of data due to high attenuation rate.

Abu Bakar Mohammad [11] discussed about the through applications of the free space communication systems its advantages and dis advantages of the system. The main focus of the scientific paper was to first analysed and identified the problems of the free space communication and minimized the existing problems. The main problem identified by the paper was the problem of data attenuation which is occurred due to rain, and the effect of scintillation effect on free space communication. To overcome this problem this problem a unique system was developed as they have successfully managed to incorporate not only the use of one single beam of diode laser but multiple usage of the diode laser. This process was done to observed the effect which occurred due to the rainfall and other parameters of attenuation in the conduction of the experiment. The experiment was done at a distance of 1141.2 meter between two buildings and in total of 4 different laser beam was used. The whole experiment was conducted with single beam to observe the notion of the solution, then it was conducted with 4 beam in a multiplexing method. The accumulated result was very promising as the optical power was measured and data rate of the transmission was more than the data received in the case of the single beam. The basic reason behind the improvement of the data was the rate of blockage in the link which was being established in the whole process but in the case of the multiple beam process there were less chances of blockage in single, as the blockage of all 4 beam simultaneously is high unlikely thus giving a more added advantaged in this process. In this paper the tracking of the last mile problem and different weather conditions which were very problematic for free space communication was also improved by the hybrid wavelength division multiplexing.

Maged Abdullah Esmail*et al.* [12] discussed that the fog was the primary challenged for the free space optics communication (FSO) system, It might be cause of attenuation that was up to hundreds of decibels per kilometre. The main focus of this scientific journal was fog measurement data coming from several locations in Europe and United States and derived a unified channel attenuation model and they also compared with existing attenuation models. Proposed model achieved a minimum of 9db, which was lower than the average root-mean-square error (RMSE). They had been investigated the statistical behaviour of the channel and developed a probabilistic model under stochastic fog conditions. Scientists are also discussed that the performance of the free space optics communication system addressing various performance metrics, including signal-to-noise ratio (SNR), bit-error rate (BER), and proposed channel capacity. The accumulated result was show that in communication environments with frequent fog, FSO would have been preferred market segment in future wireless fifth-generation/sixth-generation (5G/6G) networks having cell sizes that were lower than a 1km diameter, this model and result could be applied in determining the switching/thresholding conditions in highly reliable hybrid FSO/radio frequency (RF) networks.

Yamac Dikmelik*et al.* [13] measured the inter-sub band absorption loss as mid-infrared quantum cascade lasers which actually operates on the normal function as in continuous wave at room temperature and have a high power levels as it also has wall plug efficiencies. In this paper they have also calculated the wave guide loss in this paper for the two high-performance mid-infrared quantum cascade laser designs. The laser has the intersub band absorption loss which makes it very important of the wave guide loss for these structures. In this paper the main emphasis was given on the improvement of the wave guide loss as the loss of that parameter have huge effect on the current densities as it limits the efficient extraction of generated light out of the laser cavity. In this paper the resultant feature described as the conduction band diagram for a QCL structure which is made to have less voltage defect for the improvement of voltage efficiency.

Martin Grabner*et al.* [14] discussed the technology achievements of the free space optical communications and the merits of which, it has the upper hand on other forms of communication which are radio frequency and fiber optics. But in this paper the technical drawbacks of free space communication were also uphold like the atmospheric attenuation as they have mainly discussed in this paper. In this paper multiple scattering of light in atmospheric hydrometer was numerically simulated and presented. The paper has also used the concept of Mie scattering and Mount Carlo method as to find the relation of the optical attenuation and the physically parameter of hydrometers. The hydrometers were also described by their drop size distribution (DSD) in this particular paper, as they have formulated some of the reasons for which desired data may not be recorded as there are many way of attenuation which can hamper the experiment. The paper has also performed the DSD simulation on the concept of rain as to found out the signal attenuation rate with the help of classical Marshal-Palmer (MP) model but they have found out that distro-meter measurements also decrease as the drop number density of the smallest drops in which a slightly modified MP model was used in this particular paper. The relation between rain droplet size and the geometric scattering is also mentioned as the simulation results were discussed. Another simulation was also conducted with DSD of fog and the simulated experiment was done. The result of the rain simulation hinted that optical attenuation which occurs due to rain has a direct relationship with the intensity of the rain rate and the size of the rain droplet. They have concluded that the multiple scattering attenuation is less than be single scattering attenuation in both the cases of the rain simulation and fog simulation. They have also concluded that in dense fog, attenuation is also lesser but the comparative difference between single and multiple scattering calculations were not that great when compared with rain. The primary attributing factor is the different sizes of droplets in rain and fog.

Milica I. PETKOVIC *et al.* [15] observed the performance of intensity-modulated with direct detection (IM/DD) free space optical (FSO) system using the on-off keying (OOK) and avalanche photodiode (APD) receiver. They used gamma-gamma model to describe the effect of atmospheric turbulence since it provides good agreement in the wide range of atmospheric condition, in addition, the same FSO system with equal gain combining applied at the reception was analysed. In this paper the theoretical derivation of the expression for the bit error rate (BER), numerical integration with previously specified relative calculation error was performed. The result of this paper was presented and confirmed by Monte Carlo simulations, also the effects of the FSO link and receiver parameters on the BER performance also discussed. From the result of this paper we know that the optimal APD gain in the minimum BER sense depends considerably on the link distance, atmospheric turbulence strength and receiver temperature and the value of this optimal gain was slightly different in the case of spatial diversity application compared with single channel reception.

Dhanya Devarajan*et al.* [16] proposed a lasercom or a laser communication prototype system mainly for the satellite communication as the laser communication has many merits over its contest like the means of radio frequency and other types. As the system consists of prospective features like terahertz transmission, compact size, weight and power (SWaP) components, which can be a divisive issue in designing space missions. But the lasercom also comes with its disadvantages as it is very expensive, and the atmospheric conditions are to be considered as an optimum loss phase factor. The lasercom also requires line of sight in all conditions as to communicate data, thus ensuing in pointing loss. In this paper they have proposed a test bed prototype of the lasercom which can be used in the communication of the deep space communication. As the test bed shared with an optimizer, named as lasercom system optimizer (LSO) that helps the system designer to calculate and create an optimum set of the design parameter values. The paper also discussed the design, work, finishing prototype, features and the improvements which could happen. In this paper the link margin, fade margin was also discussed with other atmospheric parameters such as turbulence, wind and the need of laser satellite communication.

1.3. Outline of Thesis

Chapter 1 provides the overall introduction of Optical Wireless Communication (OWC).

Chapter 2 describes the Free Space Optics (FSO) communication and different types of lasers sources, i.e. the lasers are used in this project. Basic design of laser is also discussed in this chapter.

Chapter 3 describes in details of the atmospheric channel effects on Free Space LASER communication. Advantages and disadvantages of FSO communication are also discussed in this chapter.

Chapter 4 provides the design of single input and single output (SISO) block diagram and functional block diagram of data communication channel and voice communication channel.

Chapter 5 describes in details of the design of artificial simulation setup of temperature, fog and rain.

Chapter 6 contains the experimental result of the system. This chapter has two parts, first one is optical power attenuation and another one is channel attenuation.

Chapter 7 describes the theoretical overview of Multiple Input Multiple Output (MIMO) system.

Chapter 8 deals with the conclusion and the future scope of the thesis.

Reference

Appendix A contains the brief discussion of the instruments used in this project.

Appendix B contains the brief discussion of the components used in this project.

Chapter 2 – Different Types of LASER Sources

2.1. Introduction

One of the most important phenomena in the history of technology is the idea of wireless communications. More quickly than anybody could have predicted thirty years ago, wireless gadgets and technologies are already widely used, and they will likely continue to play a significant role in contemporary culture for some time to come. Due to the widespread deployment and usage of wireless RF devices and systems, the term "wireless" is now nearly always used to refer to radio-frequency (RF) technology. However, because the majority of the sub-bands are licenced exclusively, the RF band of the electromagnetic spectrum is essentially expensive and restricted in capacity. The time has come to carefully investigate additional potential choices for wireless communication employing the upper regions of the electromagnetic spectrum as RF spectrum is in short supply due to the steadily increasing popularity of data-intensive wireless communications.

In unguided propagation media, optical carriers, such as those in the visible, infrared (IR), and ultraviolet (UV) bands, are used for optical wireless communication (OWC). These optical beams are used to transmit data via the atmosphere or a vacuum to carry out data transfer. In light of this, OWC link topologies are quite similar to optical fibre communication point-to-point links with the difference that no optical fibres are used as a transmission medium. In OWC, light replaces radio waves and photo-detectors are replaced with free-space optical transceivers, which makes it very similar to RF wireless.

The Semiconductor Inter-Satellite Laser Experiment (SILEX) research programme was started by the European Space Agency (ESA) in the mid-1980s. OWC was evaluated for use in satellite-to-satellite links. The French SPOT-4 Earth observation satellite was launched into a sun-synchronous low earth orbit in 2001, and a 50 Mbps OWC link was successfully established between it and the geostationary ARTEMIS satellite [17]. Data speeds in the order of Gbps have been successfully attained thanks to the development of coherent modulation methods [18][19][20]. In order to transmit data to and from non-geostationary satellites, spacecraft, other vehicles, and permanent Earth stations, a satellite system called the European Data Relay System (EDRS) is currently being developed. It launches three GEO satellites that are outfitted with Ka-band connectivity for the space-to-ground link as well as OWC inter-satellite communications. For deep-space applications, the Jet Propulsion Laboratory (JPL) of NASA (National Aeronautics and Space Administration) and the ESA have also given optical communication between Earth and a spacecraft some thought. Aiming to show off optical communications at data speeds between 1 and 10 Mbps from Mars to the Earth, the Mars Laser Communications Demonstration (MLCD) is one project that specifically intends to do this [21]. With a scheduled launch in 2018, the Laser Communication Relay Demonstration (LCRD) project is another new NASA endeavour that attempts to show how OWC lines may be deployed for deep space inter-satellite transmission and deep space -to- Earth transmission.

Other than satellite-to-satellite and satellite-to-ground communication links, some significant work on terrestrial free space optical communication links has been ongoing since the 1960s. The first demonstration of long-distance laser communication through the atmosphere was carried out by the Hughes group in November 1962 across a distance of 30 km using a 632 nm He-Ne laser. Then, in May 1963, a collection of electro optics systems used a 632nm laser to broadcast voice-modulated data over a 190km distance from Panamint Ridge near Death Valley, California, to a site in the San Gabriel mountains close to Pasadena. A group at North America Aviation claimed to have received the first TV transmission in March 1963. The modulation bandwidth was 1.7 MHz [22].

Amplitude modulation (AM) of Laser beams with analogue information was found to be impractical in the presence of air turbulence after the initial burst of activity in 1962 and 1963. However, in the current environment, there are commercially viable terrestrial free space Laser communication links that have a data throughput of 1.25 Gbps and can go up to 2 km [23].

OWC may be examined in five different ways depending on the transmission range:

(1) OWC with an ultra-short range, such as chip-to-chip communications in multi-chip devices that are tightly packed and stacked [24].

(2) Short-range OWC, such as applications for wireless body area networks (WBAN) and wireless personal area networks (WPAN), as well as communications underwater [25].

(3) Medium-range OWC, such as indoor IR and VLC, inter-vehicle communications, and vehicle-to-infrastructure communications (WLANs) [26].

(4) Long-range OWC, such as connections between buildings.

(5) Ultra-long range OWC, such as deep space connectivity and inter-satellite links [27].

The fourth type of outdoor terrestrial OWC lines, also known as free space optical (FSO) communication, is the only one on which we are concentrating in this article. This language will be used moving forward.

2.2. History of Laser

The laser is a development of Albert Einstein's 1916 hypothesis that, under the right conditions, atoms may spontaneously or in response to light stimulation, release excess energy as light. Rudolf Walther Ladenburg, a German scientist, made the first observation of stimulated emission in 1928, albeit it didn't appear to have any application at the time.

Charles H. Townes came up with the idea to produce stimulated emission at microwave frequencies in 1951 while studying at Columbia University in New York City. He showed a functioning apparatus that concentrated "excited" (see below Energy levels and stimulated emissions) ammonia molecules in a resonant microwave cavity, where they released a pure microwave frequency, at the end of 1953.For "microwave amplification via the stimulated emission of radiation," Townes gave the gadget the name maser. The theory of maser operation was separately developed by Aleksandr Mikhaylovich Prokhorov and Nikolay Gennadiyevich Basov of the P.N. Lebedev Physical Institute in Moscow. The 1964 Nobel Prize in Physics was shared by the three of them for their efforts.

Midway through the 1950s saw a surge in maser development, although these devices were only used for a small number of things, such as atomic clocks and low-noise microwave amplifiers. In 1957, Townes suggested that he and Arthur L. Schawlow, his brother-in-law and a former postdoctoral student at Columbia University who was working at Bell Laboratories at the time, attempt to extend maser action to the considerably shorter wavelengths of infrared or visible light. Townes also spoke with Gordon Gould, a PhD student at Columbia University, who created his own laser-related concepts quite rapidly. In a ground-breaking study that appeared in the Physical Review issue of December 15, 1958, Townes and Schawlow presented their concepts for a "optical maser." Gould simultaneously created the term "laser" and submitted a patent application.Thus, the question of who should be given credit for "inventing" the laser—Townes or Gould—became the subject of heated discussion and years of court battles. In the end, Gould was granted four patents beginning in 1977, which brought in millions of dollars in royalties for him.

The Townes-Schawlow idea prompted a number of groups to attempt laser construction. A secret military contract was built on the Gould concept. Theodore H. Maiman, who adopted a different strategy at Hughes Research Laboratories in Malibu, California, first achieved success. He used a synthetic ruby crystal as the target because he had carefully examined how it absorbed and emitted light and determined that it should function as a laser. To excite the chromium atoms in the ruby crystal, he shot intense pulses using a photographer's flash lamp. He created red pulses on May 16, 1960, using a ruby rod that was approximately the size of a fingertip. At Bell Labs in December 1960, Ali Javan, William Bennett, Jr., and Donald Herriott created the first gas laser, which used a combination of helium and neon to produce a continuous infrared beam. The first semiconductor laser was created in 1962 by Robert N. Hall and colleagues at the General Electric Research and Development Centre in Schenectady, New York.

In a wide range of applications, lasers are already commonplace instruments. In lecture rooms, laser pointers emphasise presentation points, and laser target designators direct smart bombs to their intended targets. Lasers can remove undesirable hair, draw patterns on manufacturing line products without touching them, solder razor blades, and bleach tattoos. Incomparable detail was profiled on the surfaces of Mars and the asteroid Eros by laser rangefinders in spacecraft. Lasers have enabled scientists to chill atoms in the lab to within a minuscule fraction of a degree of absolute zero.

2.3. Basic Design of Laser

A gain medium, an approach to lifting it, and a mechanism to provide optical feedback make up a fundamental laser structure [11]. The gain medium is a material having characteristics that enable it to increase light using the stimulated emission method. When light of a specific wavelength passes through the gain medium, it is amplified (increase in power).

The gain medium has to be supplied with energy through a process known as pumping in order to magnify light. Typically, the energy is provided as a current of electricity or as light with a certain wavelength. A second laser or a flash bulb can provide pump light. A pair of mirrors on opposite end of the gain medium make up an optical cavity, which is used as feedback in the most common kind of laser. Each time the light passes through the gain medium and is amplified, it bounces back and forth between the mirrors. Usually, the output coupler, one of the two mirrors, is partially transparent. Depending on how the cavity is constructed (whether the mirrors are flat or curved), some of the light escapes via this mirror, which can result in a broadened or restricted beam of light coming from the laser. Occasionally, this device is referred to as a laser oscillator in comparison to electronic oscillators. The polarisation, wavelength, and beam shape of the light emitted are additional factors that affect the qualities of the light released by most practical lasers.

Consequently, it may be assumed that the basic components of a laser structure are a gain medium, laser pumping energy, output coupler, high reflector, and laser beam. Given the variety of systems and sources available for the many types of lasers that may be produced or constructed, the laser's architecture is subject to change. The Fig. 2.1. shows the basic laser structure.

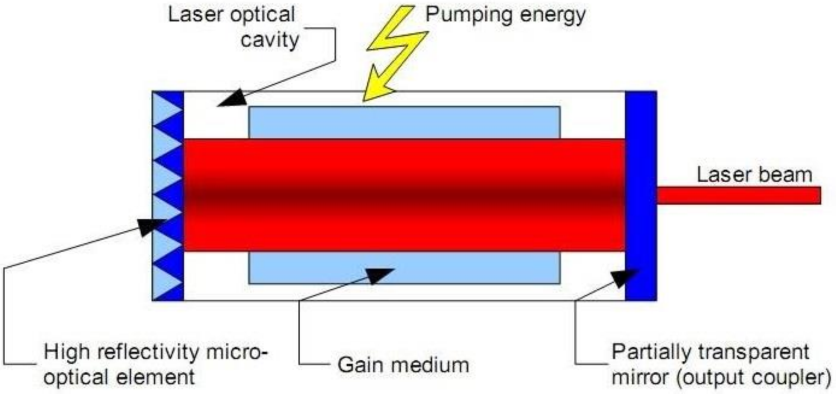

Fig. 2.1. Basic Laser structure

2.4. Different types of lasers based on their Gain Medium

There are four categories of lasers: semiconductor, solid, liquid, and gas. The laser medium that is used determines this categorization. The first laser to be created was the solid laser, of which the ruby laser is an example. The gas laser, of which the He-Ne laser is an example, was introduced immediately after that. Then came the glass and Nd-YAG lasers, followed by the GaAs junction diode, carbon dioxide lasers, nitrogen lasers, argon ions, and dye lasers. Due to their features in terms of wavelengths, excitation methods, tenability, power levels, cost, etc., additional variations, such as chemical lasers, excimer lasers, gas dynamic lasers, free electrons lasers, colour centre lasers, etc., also gained prominence.

2.4.1. Solid State Lasers

A solid state laser was the first laser to be built in this scientific society. Solid state lasers are part of the laser systems involving high-density gain media. Liquid (dye) lasers also fall in this category. Similarly, semiconductor lasers also form part of lasers with high-density gain media. In this scientific community, a solid state laser was the first laser to be constructed. The high-density gain media-using laser systems include solid state lasers. Also included in this group are liquid (dye) lasers. Similar to gas lasers, semiconductor lasers are also used in gas lasers that have high-density gain medium. Neodymium, chromium, erbium, thulium, or ytterbium are frequently used as the mixed element. LIDAR technology and a number of medical procedures, such as kidney stone removal, tissue ablation, and tattoo and hair removal, also make use of solid-state lasers. The Fig. 2.2. shows an example of a solid state laser where as in this section we will briefly cove the characteristics and basic parameters of the following lasers:

(a) Ruby lasers
(b) Nd-YAG and Nd-Glass lasers
(c) Chromium LiSAF and Chromium LiCaf lasers
(d) Uranium Cadmium lasers
(e) Titanium-Saphire lasers
(f) Alexandrite lasers
(g) Colour Centre lasers
(h) Fiber glass lasers

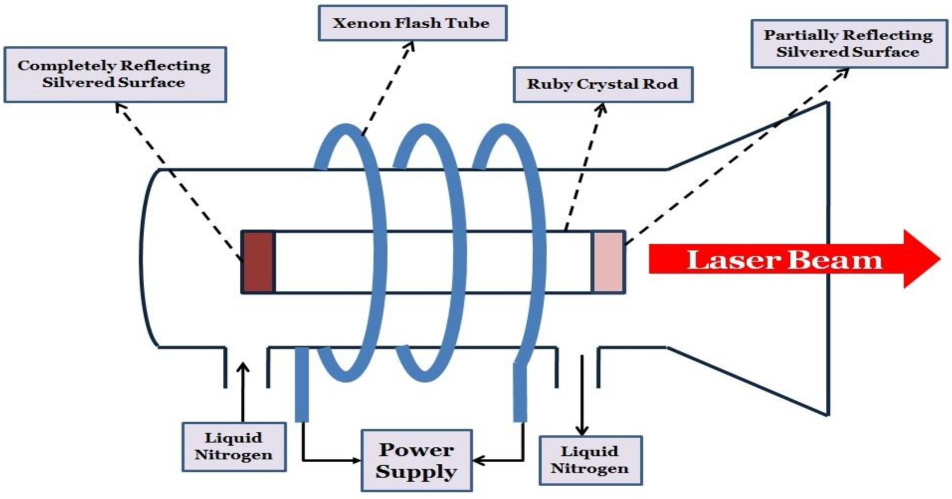

Fig. 2.2. Solid state laser (Ruby Laser)

2.4.2. Liquid Lasers

Building optimal quantities of high-quality, expensive laser crystals is difficult. Crystals are prone to flaws, imperfections, and optical strain. Damages inside, etc. Homogeneous liquids, on the other hand, have better optical properties and won't break or collapse with varying output power. Liquid lasers are those whose active medium is made up of solutions of certain organic dyes dissolved in liquids like alcohols (methyl and ethyl) or water are known as liquid lasers. These dye lasers belong to the following classes:

(a) Polymethine dyes
(b) Xanthene dyes
(c) Coumarin dyes and other dyes.

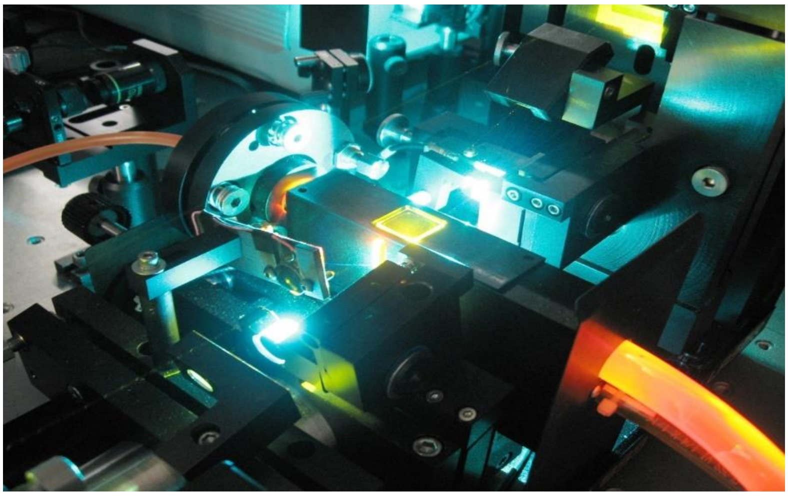

Fig.2.3. Close-up view of a table-top dye laser

2.4.3. Gas Lasers

Gas lasers are included in the category of lasers for low-density gain medium. Roughly half of the commercial lasers now on the market employ gas media. However, the majority of gaseous laser applications will undoubtedly continue for a very long time. Some gas lasers may disappear from the scene in the future due to the development of solid state lasers, which are more compact and have more potential. The three types of gas lasers—atomic, ionic, and molecular lasers—can be divided based on the properties of the active medium. High density lasers are not the same as gas lasers. Since there are no optical in homogeneities, the optical quality is superior scientifically. Other characteristics include the line width of the optical transition being smaller, the laser emission being narrower, spectrally, the Q-factor of the modes being higher, the mono-chromaticity being higher, and the coherence properties being better. A large number of laser transitions have been demonstrated among the different gaseous lasers, including the helium-neon laser, the argon-ion laser, the krypton-ion laser, the helium-cadmium laser, the copper vapour carbon dioxide laser, excimer laser. The fig.2.4. shows the basic of gas laser.

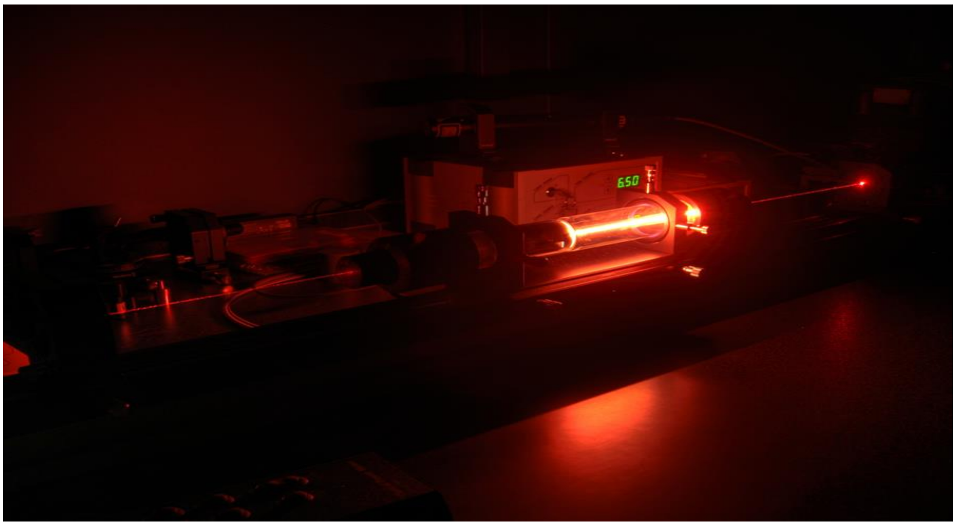

Fig.2.4. Gas laser

2.4.4. Chemical Lasers

In chemical lasers, the energy for pumping is obtained from a chemical reaction. Typical chemical lasers operate on molecular transitions. Majority of chemical users operate in near-infrared (NIR) to middle-infrared portion of the spectrum. The most common chemical lasers are hydrogen chloride (HCL) lasers and hydrogen fluoride (HF) laser. The Fig.2.5. shows the basic structure of chemical laser.

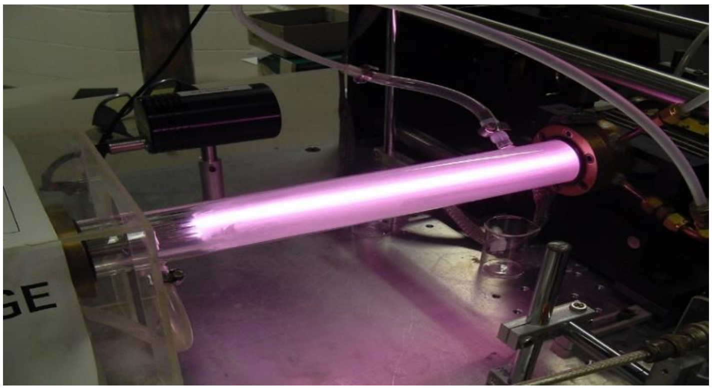

Fig.2.5. Chemical laser

2.4.5. X-Ray Lasers

An X-Ray laser is a device that produces or amplifies electromagnetic radiation in the region of the X-ray or extreme ultraviolet sector of the spectrum via stimulated emission. This electromagnetic radiation is typically on the scale of tens of nanometres (nm) in wavelength.

Coherent diffraction imaging, X-ray microscopy, phase-resolved medical imaging, material surface research, and armament are some examples of coherent X-ray radiation's applications. The Fig.2.6. shows an X-Ray laser.

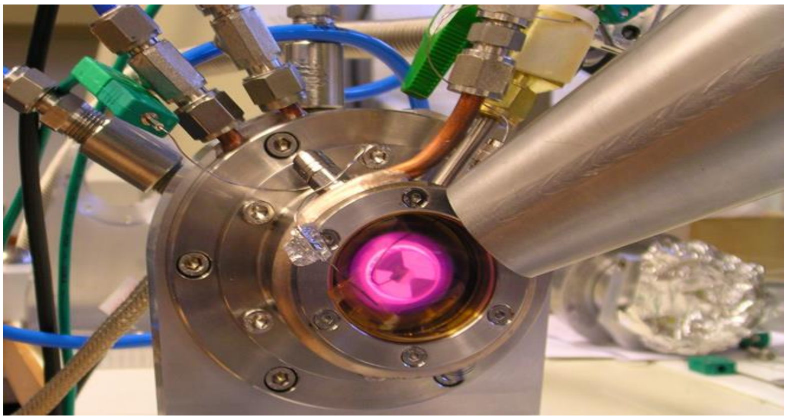

Fig.2.6. X-Ray laser

2.4.6. Free Electron Lasers

An electron stream serves as the laser's active medium in free electron lasers. These lasers can be continually tweaked by varying the energy of the electrons. Unlike with solid or liquid lasers, they provide extremely high power operating science without causing medium damage. The Fig.2.7. shows a free electron laser.

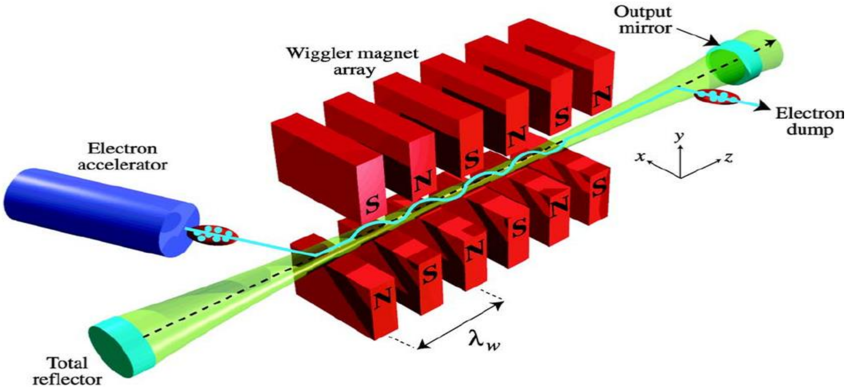

Fig.2.7. Free Electron laser

2.4.7. Semiconductor Lasers

In that they feature a positively-negatively (PN) charged junction, laser diodes, also known as diode lasers and semiconductor lasers, are comparable to normal diodes. The main distinction is that spontaneous emission-producing elements are present in a layer inherent to laser diodes near the PN junction. The intrinsic layer is polished to enable the produced photons to be amplified and finally transform the electric current into laser light. The fig.2.8. shows a semiconductor laser.

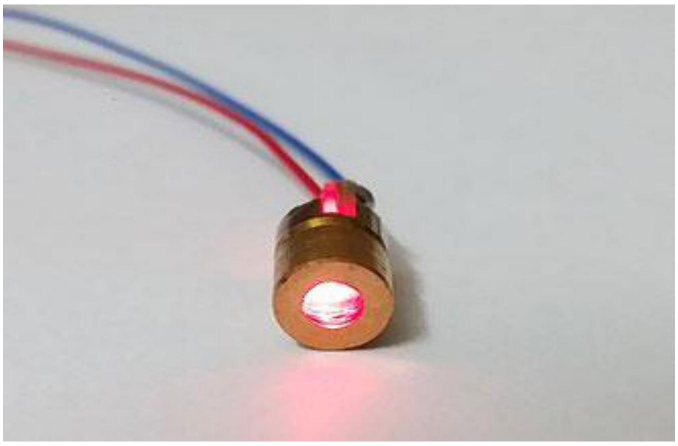

Fig.2.8. Semiconductor laser

2.5. Types of Lasers for Free Space Optical (FSO) Communication

Multiple requirements must be met for light sources used in fibre optic transmission: they must have the correct wavelength, be able to modulate quickly enough to send data, and be effectively coupled with fibre. Because of their high bandwidth capacity and restricted spectrum output, lasers have proven to be the best light sources.

2.5.1. Vertical-Cavity Surface-Emitting Laser

The vertical-cavity surface-emitting laser, or VCSE, is a type of semiconductor laser diode with laser beam emission perpendicular from the top surface, contrary to conventional edge-emitting semiconductor lasers (also in-plane lasers) which emit from surfaces formed by cleaving the individual chip out of a wafer. VCSELs are used in various laser products, including computer mice, fiber optic communications, laser printers, Face ID, and smart glasses.

There are several advantages to producing VCSELs, in contrast to the production process of edge-emitting lasers. Edge-emitters cannot be tested until the end of the production process. If the edge-emitter does not function properly, whether due to bad contacts or poor material growth quality, the production time and the processing materials have been wasted. VCSELs however, can be tested at several stages throughout the process to check for material quality and processing issues. For instance, if the visa, the electrical connections between layers of a circuit, have not been completely cleared of dielectric material during the etch, an interim testing process will flag that the top metal layer is not making contact to the initial metal layer. Additionally, because VCSELs emit the beam perpendicular to the active region of the laser as opposed to parallel as with an edge emitter, tens of thousands of VCSELs can be processed simultaneously on a three-inch gallium arsenide wafer. Furthermore, even though the VCSEL production process is more labor and material intensive, the yield can be controlled to a more predictable outcome. Fig.2.9. shows a vertical-cavity surface-emitting laser.

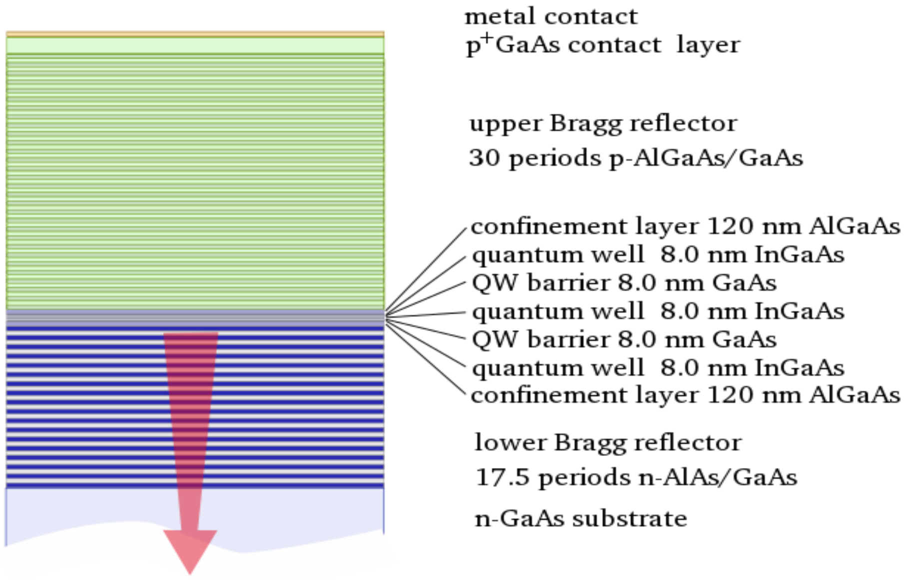

Fig.2.9. The vertical-cavity surface-emitting laser

2.5.2. Fabry Perot Laser

The most popular kind of laser diode has a laser resonator that is a Fabry-Perot interferometer, and is known as a Fabry-Perot laser diode (FP laser diode). This indicates that significant light reflections take place at both ends but not inside the gain medium. The resonator of a distributed Bragg reflector laser, in contrast, displays a scattered reflection throughout the gain medium, often produced by a grating structure.

The end reflections in a Fabry-Pérot laser, in their most basic form, are Fresnel reflections at the junction of the semiconductor device structure and air. It should be noted that the refractive index contrast at these sites is rather strong, resulting in a significant reflectivity even without extra measures. The threshold pump power may already be low enough if that concept is used on both sides, and each side will provide roughly half of the optical output power.

One frequently enhances the reflectivity on the side opposite to the output side, e.g. with a semiconductor Bragg mirror structure, in order to acquire the complete output power on one side, which is typically desirable, or to optimise the output power via a lower threshold pump power. Increased reflectivity is achieved with Bragg mirrors, or with a Bragg mirror on only one side, in the specific instance of a distributed Bragg reflector laser (DBR laser).

The beam quality of a Fabry-Perot laser diode can be either relatively good when it emits just on basic spatial resonator modes, or it can be worse when it emits on higher-order spatial modes. The latter scenario is most frequently shown with a large area laser diode. When allowing for spatially multimode emission, often in an active region with expanded dimensions, greater output power (several watts) may be generally produced.

Even though lasing is only possible on basic spatial modes, it may also happen on several longitudinal modes. The free spectral range of the laser resonator may be sufficiently limited in comparison to the gain bandwidth to support such phenomena despite the comparatively short length of the laser resonator. As a result, there are many optical frequencies visible in the laser output spectrum. (These have spacing that is normally in the range of 100 GHz.) It is also possible for emission to take place on a single mode at a time, however temperature fluctuations can occasionally cause mode hops to nearby resonator modes or oscillation on two different modes. Fig.2.10. shows a Fabry-Perot laser.

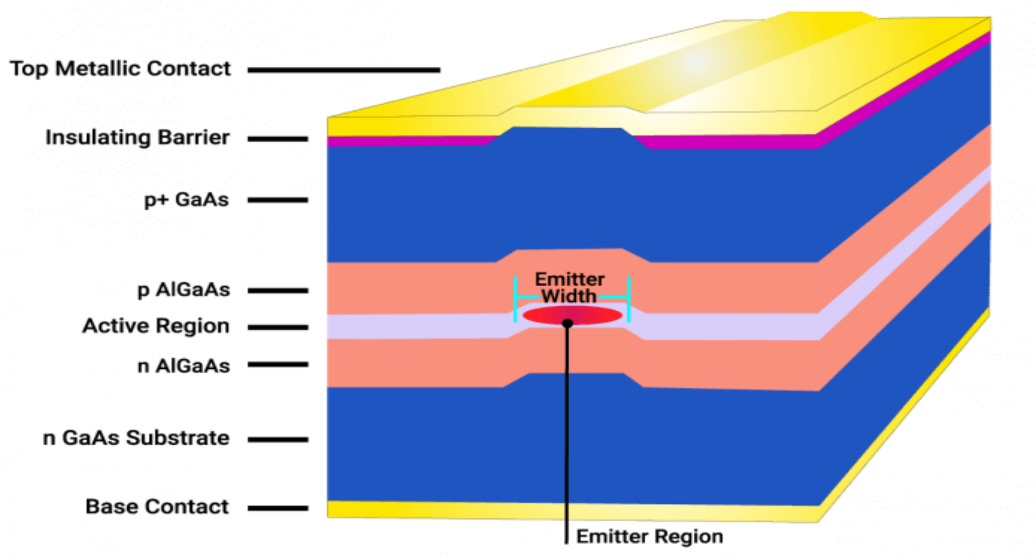

Fig.2.10. Fabry-Perot laser

2.5.3. Distributed Feedback Laser

When a regularly structured element or diffraction grating is included in the active zone of a laser diode, quantum cascade laser, or optical fibre laser, the device is referred to as a distributed feedback laser (DFB). A one-dimensional interference grating is created by the structure (Bragg scattering), and the grating gives the laser optical feedback. Periodic variations in the refractive index of this longitudinal diffraction grating result in reflection back into the cavity. The refractive index's periodic change might occur in either the real or imaginary parts (gain or absorption). The first order, where the periodicity is one-half wave and the light is reflected backwards, is where the strongest grating works. When clean single mode operation is required, especially in high speed fibre optic telecommunications, DFB lasers are typically utilised since they have a tendency to be significantly more stable than Fabry-Perot or DBR lasers. The market for long-distance communication is dominated by semiconductor DFB lasers operating in the lowest loss window of optical fibres at about 1.55um wavelength, amplified by erbium-doped fibre amplifiers (EDFAs), while DFB lasers operating in the lowest dispersion window at 1.3um are used for closer ranges.

The configuration is referred to be a DBR laser if either one or both of these end mirrors are replaced by a diffraction grating (Distributed Bragg Reflector). Similar to a multi-layer mirror coating, these longitudinal diffraction grating mirrors reflect the light back into the cavity. The number of standing waves that can be maintained by the gain in the cavity is constrained by the fact that diffraction grating mirrors have a tendency to reflect a smaller band of wavelengths than typical end mirrors. Therefore, compared to Fabry-Perot lasers with broadband coatings, DBR lasers are often more spectrally stable. But the laser can "mode-hop," switching from one standing wave to another, when the temperature or current varies. However, because the longitudinal modes of DBR lasers are chosen by the mirrors and shift with the refractive index rather than the peak gain, the total alterations with temperature are less.

Instead of being restricted to the two ends of the cavity, the grating and reflection are often continuous throughout the cavity in a DFB laser. The laser becomes much more steady as a result of the significant modal behaviour shift. DFB lasers come in a variety of designs, each having somewhat unique characteristics. Fig.2.11. shows a distributed feedback laser.

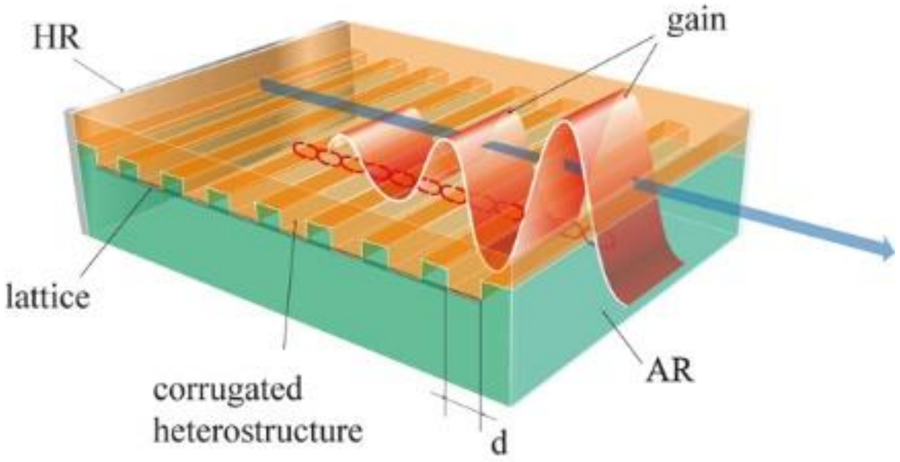

Fig.2.11. Distributed feedback laser

2.5.4. Quantum Cascade Laser

Precision sensing, spectroscopy, medicinal, and military applications are finding new uses for quantum cascade lasers (QCL), semiconductor lasers that emit in the mid- and long-wave IR bands (1). They are replacing slower and bigger FTIR, mass spectroscopy, and photo thermal micro spectroscopy systems with quicker and more accurate small trace element detectors and gas analysers due to their wide tuning range and quick reaction time.

Since the first QCL was put into service in 1994, a lot of work has gone into making them more durable, adaptable, and manufacture able. Quantum cascade lasers are employed in a wide range of sensing and spectroscopic applications, including medical diagnostic breath analysers, safe-distance explosives detectors, light sources for infrared imaging systems, and industrial exhaust sensing. As researchers and manufacturers get more expertise with QCLs, the number of markets for them is expanding at an ever-increasing rate.

An electron from the conduction band recombines with a hole from the valence band, and a single photon is released as a result. This mechanism is the foundation of electron-hole recombination, which is how diode lasers work. Because the recombination energy, or bandgap, of the material system used to make the device limits the wavelength, diode lasers can only operate at a maximum wavelength of roughly 2.5 µm. There are a finite number of materials that can be combined to create a diode laser, and these combinations provide a finite number of bandgaps. Fig.2.12. shows a quantum cascade lasers.

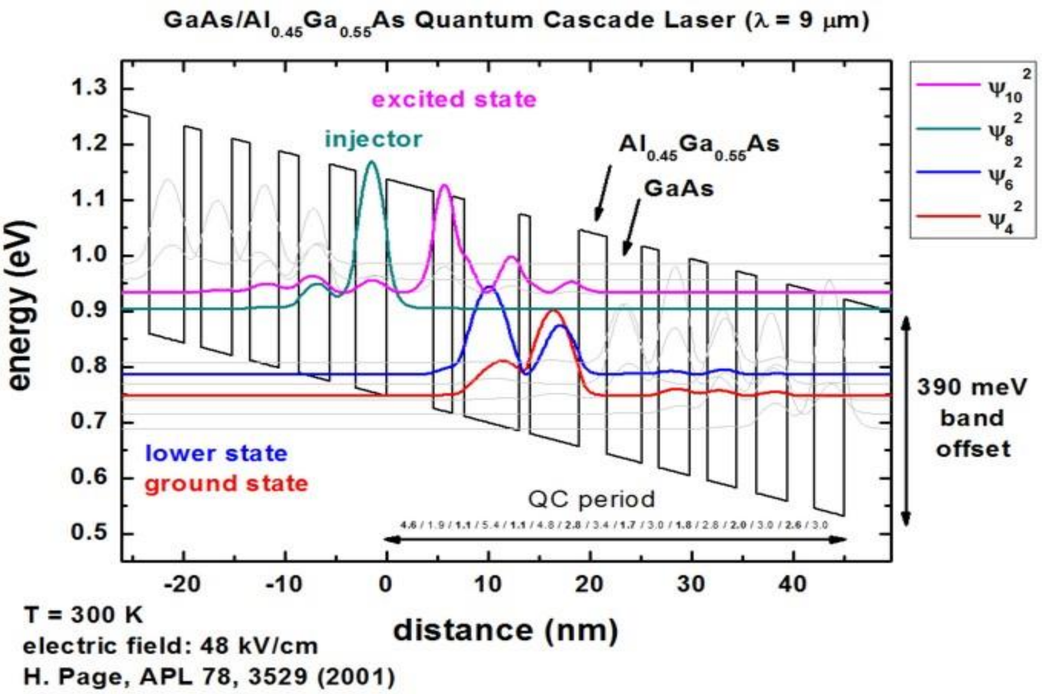
GaAs/$Al_{0.45}Ga_{0.55}As$ Quantum Cascade Laser (λ = 9 µm)

T = 300 K
electric field: 48 kV/cm
H. Page, APL 78, 3529 (2001)

Fig.2.12. Quantum cascade lasers

2.5.5. Fiber Laser

A fibre laser is a laser in which an optical fibre doped with rare-earth elements including erbium, ytterbium, neodymium, dysprosium, praseodymium, thulium, and holmium serves as the active gain medium. They share a connection with lasing-free doped fibre amplifiers, which amplify light. In addition to providing gain, fibre nonlinearities such stimulated Raman scattering and four-wave mixing may also act as gain media for a fibre laser.

Fiber lasers have an advantage over other types of lasers in that the laser light is produced and delivered via a medium that is naturally flexible, making it simpler to deliver the laser light to the target and concentrating point. This can be crucial for metal and polymer laser cutting, welding, and folding. High output power in comparison to other laser types is another benefit. Since the active zones of fibre lasers can be many kilometres long, they can offer extremely high optical gain. The large surface area to volume ratio of the fibre, which enables effective cooling, enables them to maintain kilowatt levels of continuous output power. The optical path's heat distortion is reduced or completely eliminated by the fiber's waveguide capabilities, leading to a usually high-quality, diffraction-limited optical beam. Because the fibre may be twisted and coiled, with the exception of thicker rod-type systems, fibre lasers are smaller than solid-state or gas lasers of equivalent power. Their ownership costs are cheaper. Fiber lasers are dependable, have a high level of vibrational and thermal stability, and have a long lifespan. Both engraving and marking are improved by high peak power and nanosecond pulses. Cleaner cut edges and quicker cutting rates are made possible by the increased power and greater beam quality. The processing of materials, telecommunication, spectroscopy, medicine, and directed energy weaponry are further uses for fibre lasers.

Contrary to most other types of lasers, fibre lasers are built monolithically by fusion splicing several fibre types; fibre Bragg gratings take the role of traditional dielectric mirrors to offer optical feedback. In situations where a phase-shifted Bragg grating overlaps the gain medium, they may also be created for single longitudinal mode operation of ultra-narrow distributed feedback lasers (DFB). Fiber lasers can be pumped by other fibre lasers or semiconductor laser diodes. Fig.2.13. shows the fiber laser.

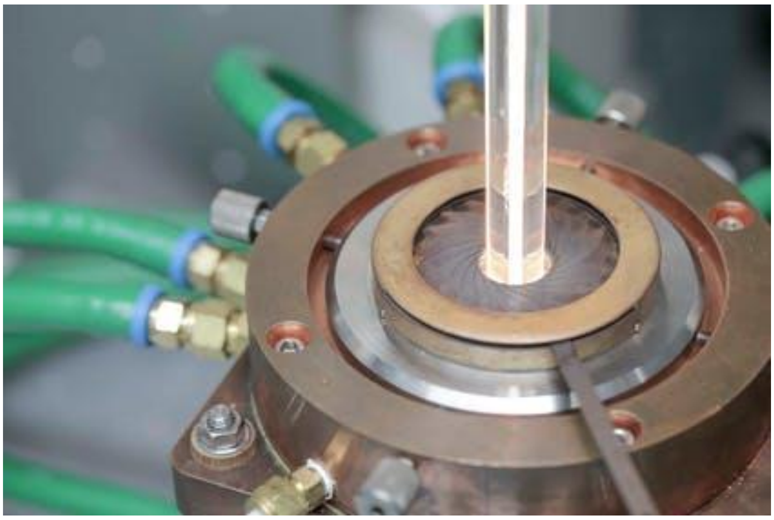

Fig.2.13. Fiber Laser

2.5.6. Diode Pumped Solid State Laser

A diode-pumped solid-state laser (DPSSL) is a solid-state laser created by pumping a solid gain medium, such as a ruby or a neodymium-doped YAG crystal, with a laser diode. High power DPSSLs have supplanted ion lasers and flash lamp-pumped lasers in many scientific applications and are now routinely found in green and other colour laser pointers. DPSSLs offer benefits over other kinds in terms of compactness and efficiency. Temperature is used to adjust the wavelength of laser diodes to provide the best possible trade-off between the absorption coefficient in the crystal and energy efficiency (lowest possible pump photon energy). Higher power densities as compared to high-intensity discharge lamps are possible since waste energy is constrained by the thermal lens.

The green laser pointer with a wavelength of 532 nm is the most widely used DPSSL. Neodymium-doped yttrium aluminium garnet (Nd:YAG) or yttrium orthovanadate (Nd:YVO4) crystals emit 1064 nm wavelength light from the primary spectral transition of neodymium ions when pumped by a powerful (>200 mW) 808 nm infrared GaAlAs laser diode. Then, this light undergoes a nonlinear optical process in a KTP crystal to produce 532 nm light, which is frequency doubled. Although some lasers may achieve up to 35 percent efficiency, green DPSSLs typically have an efficiency of approximately 20 percent. To put it another way, a green DPSSL employing a 2.5 W pump diode should produce between 500 and 900 mW of 532 nm light.

The process for making blue DPSSLs is essentially the same, with the exception that a Nd:YAG crystal converts the light from 808 nm to 946 nm (selecting this non-principal spectral line of neodymium in the same Nd-doped crystals), which is then frequency-doubled to 473 nm by a beta barium borate (BBO) crystal or an LBO crystal. Blue lasers are only around 3-5 percent efficient, which makes them rather weak due to the lower gain for the materials. Bismuth triborate (BiBO) crystals were found to be more effective than BBO or LBO in the late 2000s and to not be hygroscopic, which causes the crystal to deteriorate when exposed to moisture.

Yellow DPSSLs employ an even trickier method: an 808 nm pump diode generates 1,064 nm and 1,342 nm light, which are then added parallel to produce 593.5 nm. Due to its complexity, most yellow DPSSLs have efficiency levels of only 1% or less and are typically more expensive per unit of electricity. Fig.2.14. shows the internal structural diagram of DPSS laser and fig2.15. shows different wavelengths DPSS Laser.

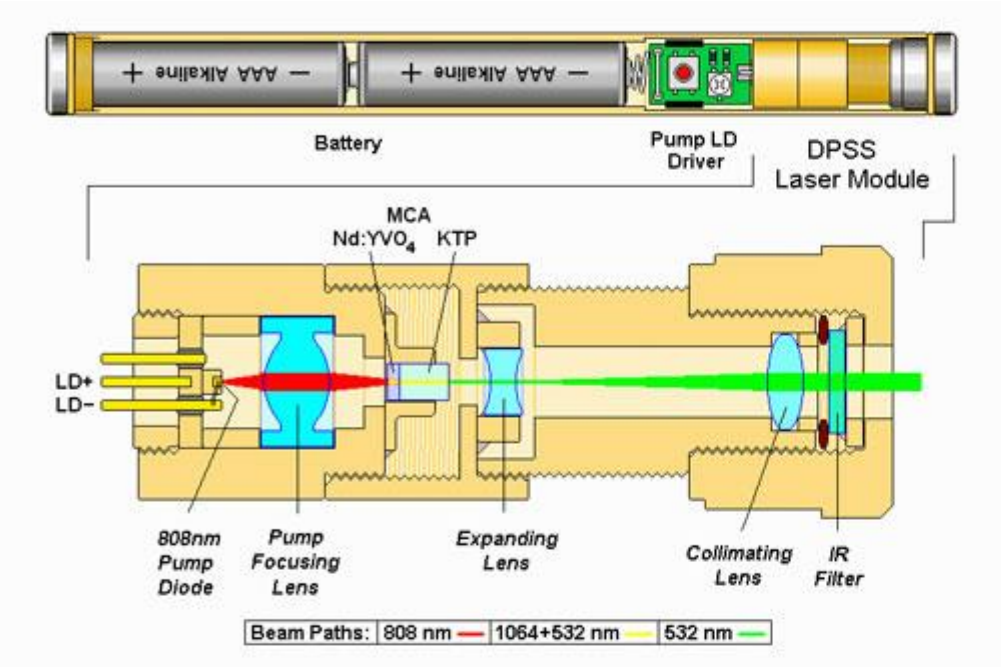

Fig.2.14. Internal structural diagram of DPSS Laser

Fig.2.15. Different wavelengths DPSS Laser

Chapter 3 – Atmospheric Channel Effects on Free-Space Optical Communication

3.1. Introduction

Attenuating factors for the signal-carrying laser beam include fog, rain, dust, snow, smoke, and other aerosol particulate matter. To some extent, this attenuation can be compensated for by raising the signal gain. By choosing the right optical wavelength, one may reduce molecule absorption. On the other hand, optical turbulence caused by random variations in the atmosphere's refractive index always leads to higher bit error rates in the system, particularly for propagation pathways that pass over extended segments of the Earth's atmosphere near horizontally. Longer wavelengths perform better, but there is no wavelength "window" where these effects can be avoided. Additionally, increasing signal gain does not always result in better laser beam quality because optical turbulence-induced signal losses increase as the transmitter to receiver distance increases. The persistent existence of optical turbulence in the air channel is the limiting factor for dependable wireless optical communication connection performance in many circumstances of practical importance. With the goal of equipping the reader with the skills needed to assess and forecast the expected performance of laser communication systems, we make an effort to provide some understanding of the physical processes underlying optical extinction and optical turbulence-induced signal losses in this paper. We start with a summary of the fundamental physics concepts behind the mechanisms that molecules and aerosol particles utilise to absorb and scatter light, which create optical extinction. There are different models in use for molecular extinction and for aerosol extinction, and we survey those that are the most useful in the prediction of signal loss. The creation of optical turbulence and its relationship to atmospheric characteristics are then covered. To enable the estimate of optical turbulence strength at various atmospheric levels, a complete collection of optical turbulence models is offered. The behaviour of the signal beam as it propagates in optical turbulence is explored, and this discussion results in equations for calculating bit error rates in optical communication systems as functions of both communication system and optical turbulence characteristics. It is possible to compute projected system performance for ground-to-ground, ground-to-air/air-to-ground, and satellite uplink/downlink optical communication scenarios with the use of the information supplied, which is suitable for both system designers and users.

3.2. Advantages and Applications of FSO

For high-speed communication across lengths of up to several kilometres between two fixed sites, FSO systems are employed. The FSO link's extremely high accessible optical bandwidth allows for significantly greater data speeds as compared to RF equivalents. Systems for FSO utilise extremely thin laser beams. The high reuse factor, built-in security, and electromagnetic interference resistance of this spatial confinement are all advantages. Additionally, the frequency that the FSO technology uses is over 300 GHz, which is globally unlicensed. As a result, no licence costs are needed for FSO systems [30]. Deploying and reinstalling FSO systems is extremely simple and doesn't require a separate fibre optic connection, which saves money. Fig.3.1. shows FSO optical connection link.

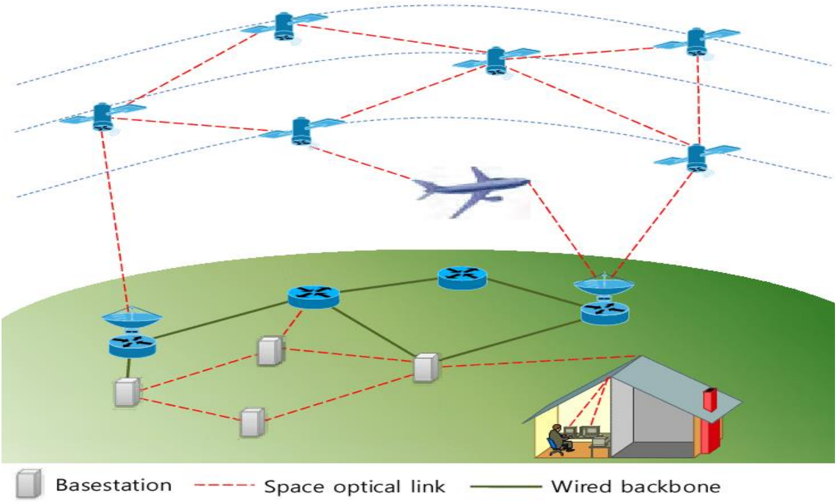

Fig.3.1. FSO optical communication link

3.2.1. Enterprise/Campus Connectivity

The conventional connections are being overwhelmed by the varied network traffic that is currently being experienced by businesses and college/university campuses (i.e., phone, data, fax, and multimedia traffic). Corporate and campus networks that enable ultra-high speeds can connect several buildings with FSO systems without having to pay for separate fibre optic connections. Fig.3.2. shows campus/enterprise connectivity.

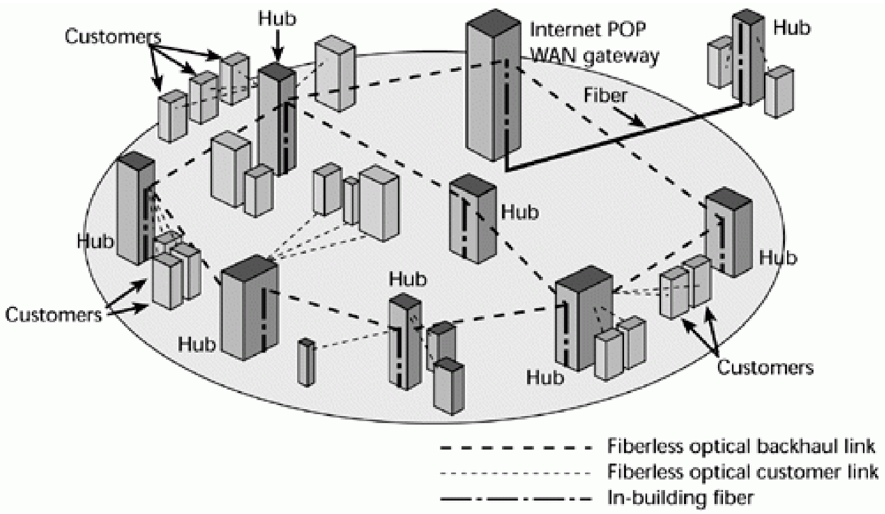

Fig.3.2. Campus/Enterprise Connectivity

3.2.2. Video Surveillance and Monitoring

In commercial, law enforcement, public safety, and military purposes, surveillance cameras are frequently used. Although wireless video is quick and simple to set up, traditional wireless technologies fall short of meeting the high throughput requirements for video broadcasts. An effective solution to enable high quality video transmission is FSO technology.

3.2.3. Back-Haul for Cellular Systems

In a cellular system, wire line connections, such as T1/E1 leased lines and microwave links, are frequently used between the base stations and the mobile switching centre. It is now necessary to implement technologies like FSO that allow for substantially higher throughput due to the increase in the number of bandwidth-intensive mobile phone services.

3.2.4. Redundant link and disaster recovery

Emergency circumstances, terrorist assaults, and natural calamities all call for adaptable and creative solutions. In such catastrophic circumstances when local infrastructure may be destroyed or unreliable, temporary FSO linkages can be easily installed within hours. The efficacy of the FSO deployment as a redundant connection was tragically demonstrated in the wake of the 9/11 terrorist attacks in New York City. For the financial corporations that were left behind without landlines, FSO linkages were swiftly implemented in this area.

3.2.5. Security

The advent of quantum computers, for instance, would render electronic money suddenly useless because current cryptosystems can only provide computational security within the bounds of available conventional computing power. Quantum cryptography, which is based on the unchanging principles of physics, offers an entirely new approach to encryption and ensures complete security. Usually, fibre optic infrastructure is taken into account in combination with quantum cryptography systems. In situations where the deployment of fibre optics is expensive and/or impractical, FSO linkages offer a flexible substitute.

3.2.6. Broadcasting

Signals from the camera (or cameras) must be transmitted to the broadcasting truck, which is connected to a central office via satellite uplink, in order to broadcast live events like sports and ceremonies or television reporting from remote locations and conflict zones. A FSO link may be used to transmit data at the needed high quality between the cameras and the vehicle. High definition television (HDTV) broadcasting applications currently have throughput requirements that can be met even by FSO lines. For instance, the UK TV station BBC used FSO lines for the 2010 FIFA World Cup to carry high quality footage between temporary studio facilities built up in Cape Town, South Africa, using Ethernet.

Several businesses, including Canon (Japan), Cassidian (Germany), fSONA (Canada), GeoDesy (Hungary), Laser ITC (Russia), Light Pointe Communications (USA), MRV (USA), Northern Hi-Tec (UK), Novasol (USA), Omnitek (Turkey), Plain tree Systems (Canada), and Wireless Excellence (UK), among others, are currently developing and manufacturing FSO systems as outdoor wireless transmission solutions.

3.3. Disturbance in FSO channel

Before it reaches the receiver, the optical power released from the transmitter is impacted by a number of things. These include ambient noise, system loss, geometric loss, misalignment loss, atmospheric loss, and fading caused by air turbulence. The design parameters, which are typically supplied by the manufacturers, have a significant impact on the system loss. The next paragraphs address losses that are included into the FSO channel.

3.3.1. Geometric and Misalignment Losses

The geometric loss is brought on by the beam's divergence during atmospheric propagation. Given the divergence angle, link length, and receiver lens aperture size, it may be determined. The optical wave propagation model is a crucial component in determining the geometric loss. A useful approximation for horizontal FSO broadcasts is to think of the beam intensity as having a Gaussian profile [31]. A Gaussian beam's statistical characteristics resemble those of a point source when the divergence is reasonably big [32]. The approximations of a plane wave or spherical wave can be employed successfully in this situation. The alignment of the transmitter and receiver as well as beam tracking at the reception are both impacted by the degree of beam divergence misalignment happens in real life most often as a result of beam wander, structural issues with structures, or tracking system mistakes. Beam wander is the result of large-scale atmospheric eddies that are not homogeneous, which leads to random deflections of the optical beam, which causes the beam to diverge from its intended direction [33] [34]. For long distance routes, this phenomenon is very significant. In contrast, building sway is caused by a number of variables, such as thermal expansion, wind loads, minor earthquakes, and vibrations [35]. Building sway has the potential to effectively stop communication due to the narrow transmission beam and often short receiver field of vision (FOV). The use of automated pointing and tracking at the receiver becomes important over long distances (i.e., one kilometre or more), since a narrower beam should be employed to avoid suffering from a significant geometric loss, in order to eliminate or limit the consequences of pointing mistakes.

3.3.2. Atmospheric Loss

In the visible and near-IR wavelength ranges, the physics and transmission characteristics of the radiation penetrating the atmosphere are extremely similar. As a result, visibility may also be used to describe particles that scatter or absorb near-IR radiation. Rain, snow, and fog are examples of the particles that can reduce visibility, but they also include pollution, dust, aerosols, smoking, etc. They partially absorb the energy of the laser light, which reduces the optical power. Water vapour plays a major role in near-IR absorption [36]. They produce spatial, angular, and temporal dispersion by inducing light scattering, which is the deflection of incoming light from its initial direction. The size of the particles in rain and snow is substantially bigger than the wavelength, which has the effect of leaving the FSO transmission mostly untouched. Rain attenuation levels on the order of 3dB/km are typical for

FSO systems deployed in urban areas across distances of less than one kilometre. In deployments beyond the distance scale of a normal metropolitan region, the attenuation can only become a problem during very severe rain. Snow has far bigger droplets than rain, hence attenuation can be more severe with snowfall. As a matter of fact, the effects of light snow to blizzards lie roughly between light rain and moderate fog. The scattering coefficient that results is particularly high when the particle diameter is on the order of the wavelength. Fog and haze, which are made up of tiny particles with radii close to near-IR wave lengths, are thus the environmental conditions that are most harmful. Even light fog can significantly weaken IR transmissions over shorter distances. About 90% of the transmit power is lost over a distance of 50 m in moderate fog, according to experimental studies. In this study, channel modelling for FSO communication during fog is investigated. According to the experimental findings, atmospheric attenuation for fog is essentially wavelength independent between 785 and 1550 nm, whereas for haze, it is wavelength dependant. As haze particles typically range in size from 0.01 to 1 m, whereas fog droplets have a radius of 1 to 20 m, haze circumstances result in less attenuation of the beam light [37]. Additionally, under hazy and thick fog situations, various scattering sizes lead to wavelength dependency of light extinction. A wavelength dependent attenuation coefficient model is suggested for fog and haze conditions in a thorough study based on the Mie scattering theory that is provided [38]. It's noteworthy to notice that rain has a negative effect on RF wireless systems that employ frequencies above around 10 GHz, but that fog has less of an effect.

The attenuation of laser power through the atmosphere is described by the exponential Beers-Lambert Law [19][62][64],

$$\tau\,(L) = P(\mathrm{L})/P(0) = e^{-\alpha L} \qquad (1)$$

Where $\tau\,(L)$ = transmittance at range L,

$P(\mathrm{L})$ = laser power at R,

$P(0)$ = laser power at the source, and

α = attenuation or total extinction coefficient (per unit length).

Different particles and gaseous molecules in the atmosphere absorb and scatter laser photons, which affects the attenuation coefficient. Since saleroom wavelengths (usually 785 nm, 850 nm, and 1550 nm) are selected to lie inside transmission windows within the ambient absorption spectra, the contributions of absorption to the overall attenuation coefficient are quite minor [39]. The overall attenuation coefficient is thus dominated by the effects of scattering. The size of a certain air particle in relation to the transmission laser wavelength determines the kind of scattering. The size parameter x_0 is a dimensionless number that expresses this [40][41].

$$x_0 = 2\pi r/\lambda \qquad (2)$$

Where, r = radius of the scattering particle, and

λ = laser wavelength.

If $x_0 << 1$, the scattering process is classified as Rayleigh scattering.

If $x_0 \simeq 1$, it is Mie scattering.

If $x_0 >> 1$, the scattering process can then be explained using the diffraction theory (geometric optics).

Type	Radius(μm)	Size Parameter x_0	Scattering process
Air Molecules	0.0001	0.00074	Rayleigh
Haze particle	0.01-1	0.074-7.4	Rayleigh- Mie
Fog droplet	1-20	7.4-147.8	Mie- Geometrical
Rain	100-10000	740-74000	Geometrical
Snow	1000-5000	7400-37000	Geometrical
Hail	5000-50000	37000-370000	Geometrical

Table 1 Typical atmospheric scattering particles with their radii and scattering process at λ= 850nm [41]Rayleigh scattering changing as -4 means that for the saleroom wavelengths of interest, the effect of Rayleigh scattering on the overall attenuation coefficient is quite little [42]. The radiation scattering from bigger particles becomes more pronounced in the forward direction as compared to the backward direction as the particle size approaches the laser wavelength. Mie scattering is the name for this kind of scattering, in which the size parameter fluctuates between 0.1 and 50. Aerosol, haze, and tiny fog particles scatter the laser light at its wavelengths. The atmospheric attenuation co-efficient for Mie-scattering is given by [41] [43] [44]

$$\alpha = 3.91/V\ (\lambda/550\text{nm})^{-q} \quad (3)$$

Where:

V= Visibility in kilometres

q=the size distribution of the scattering particles.

According to Kim Model value of q is given by [41][44]

$$q = \{\begin{array}{ll} 1.6 & V>50km \\ 1.3 & 6km<V<50\ km \\ 0.16V + 0.34 & 1km<V<6km \\ V-0.5 & 0.5km<V<1km \\ 0 & V<0.5km\} \end{array}$$

Weather condition	**Visibility range (m)**
Thick fog	200
Moderate fog	500
Light fog	770-1000
Thin fog/heavy rain (25 mm/hr)	1900-2000
Haze/ medium rain (12.5 mm/hr)	2800-40000
Clear/ drizzle (0.25 mm/hr)	18000-20000
Very clear	23000-50000

Table.2. Weather conditions and their visibility range values [41]

The channel coherence bandwidth, which is the inverse of the channel delay spread, is a crucial factor to be taken into account in the FSO channel modelling process. Fog, moderate cloud cover, and rain have the ability to cause the temporal widening of optical pulses, whereas the FSO channel has a negligibly small delay spread in clear weather. Inter-symbol interference (ISI) and a reduction in system performance are the outcomes of this [45]. The channel delay spread brought on by beam dispersion because of fog or rain is, however, essentially insignificant given the average data rates of FSO lines. The channel root mean square (RMS) delay spread was recently quantified using numerical Monte Carlo-based simulations, which demonstrates this. In example, the RMS delay spread caused by rain for a 1 kilometre link is less than 10 picoseconds under practical conditions. Additionally, the delay spread is often no greater than 50 picoseconds in conditions of moderate and severe fog [46]. As a result, the channel may be thought of as being frequency on-selective in any situation and not introducing ISI. Fig.3.3. shows atmospheric turbulence in FSO.

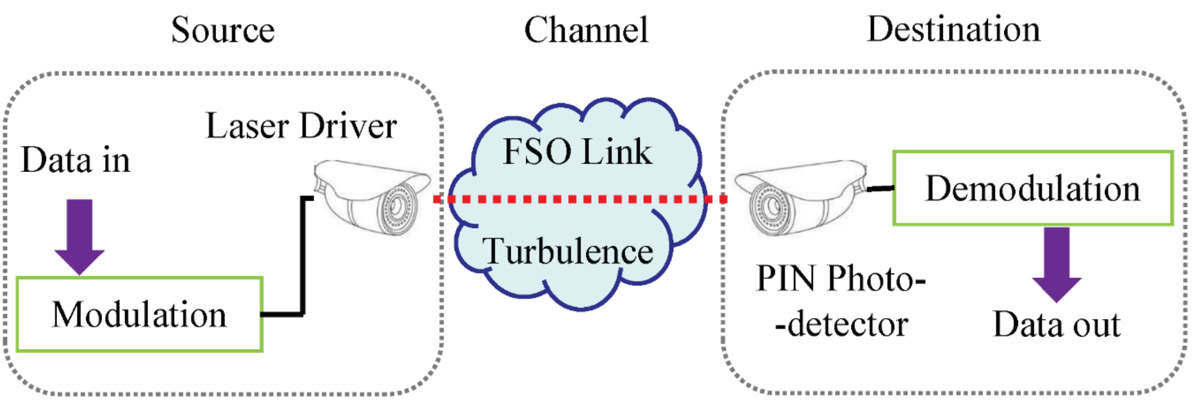

Fig.3.3. Atmospheric Turbulence in FSO

3.3.3. Atmospheric Weather Conditions

In an FSO connection, the transmission medium is the atmosphere. It can weaken an object under a variety of circumstances. The primary reason for attenuation is weather. For example, fog and heavy snow are the two main weather conditions in temperate zones, and these circumstances are peculiar to the place where a link is being constructed and allow for the acquisition of the prior knowledge of attenuation. The two primary meteorological conditions in tropical areas are heavy rain and haze, both of which have a significant impact on the region's FSO link availability [50]. Fig.3.4. Different physical and weather condition effect on FSO link.

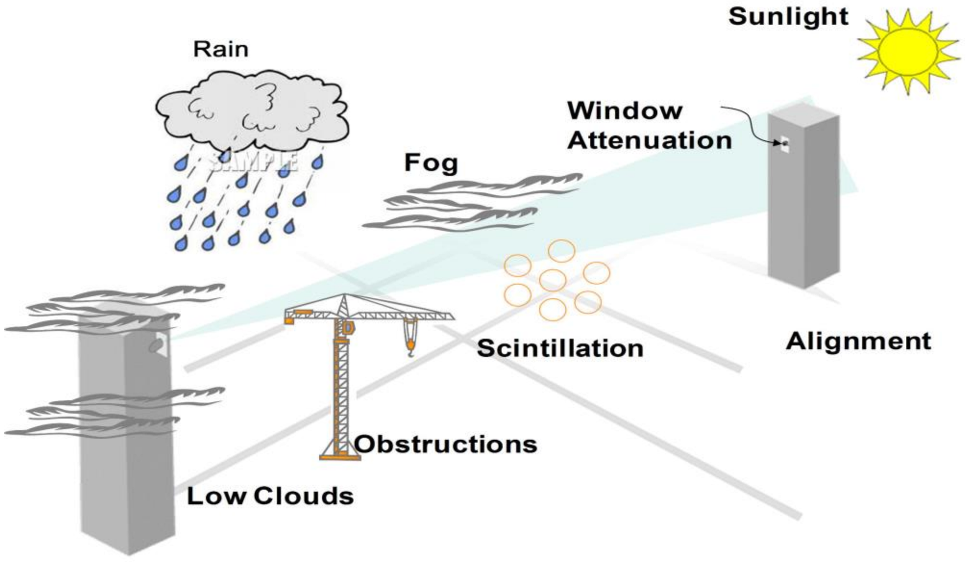

Fig.3.4. Different physical and weather condition effect on FSO link

The following lists a few weather conditions.

3.3.3.1. Fog

Visible light is significantly attenuated by fog. The obstruction brought on by fog causes an optical beam of light to be absorbed, dispersed, and reflected. The majority of fog-related scattering, also known as Mie scattering [51], involves increasing the transmitted power. Some models are used to calculate the signal attenuation caused by fog. There are several methods that provide precise attenuation calculations for various wavelengths based on visibility data. The Kruse model and the Kim model are the two most often used models in optical attenuation.

$$\Gamma(\upsilon, \lambda) = \left(\frac{17}{\upsilon}\right)\left(\frac{\lambda}{550}\right)^{-q} \text{ ....(viii)}$$

Where q is the size distribution coefficient of scattering, (nm) is the operating wavelength, and v(km) is the visibility range.

In practical, according to **KIM model**

$$q = \begin{cases} 1.6 & V>50\text{km} \\ 1.3 & 6\text{km}<V<50\text{ km} \\ 0.16V + 0.34 & 1\text{km}<V<6\text{km} \\ V-0.5 & 0.5\text{km}<V<1\text{km} \\ 0 & V<0.5\text{km} \end{cases}$$

Different weather conditions can be specified based on their visibility range values. Table 3, Table 4, Table 5 and Table 6 summarizes the visibility range and maximum loss for different weather conditions for 532nm, 650nm, 808nm and 980nm respectively [69].

For λ=532nm

Table.3

Sl. No.	Weather Condition	Visibility Range (Km)	Loss(Db/Km) for 532 nm
1.	Extremely Clear Weather	50	0.075
2.	Very Clear	25	0.15

3.	Clear	10	0.37
4.	Light haze	5	0.75
5.	Haze	2	1.91
6.	Thin Fog	1	3.85
7.	Light Fog	0.500	7.78
8.	Moderate Fog	0.250	15.64
9.	Thick Fog	0.1	39.1
10.	Dense Fog	0.05	78.2

For λ=650nm

Table.4

Sl. No.	**Weather Condition**	**Visibility Range (Km)**	**Loss(Db/Km) for 650 nm**
1.	Extremely Clear Weather	50	0.1
2.	Very Clear	25	0.19
3.	Clear	10	0.5
4.	Light haze	5	0.93
5.	Haze	2	2.2
6.	Thin Fog	1	4.2
7.	Light Fog	0.500	8.01
8.	Moderate Fog	0.250	15.64
9.	Thick Fog	0.1	39.1
10.	Dense Fog	0.05	78.2

For λ=808nm

Table.5

Sl. No.	Weather Condition	Visibility Range (Km)	Loss(Db/Km) for 808 nm
1.	Extremely Clear Weather	50	0.14
2.	Very Clear	25	0.26
3.	Clear	10	0.65
4.	Light haze	5	1.21
5.	Haze	2	2.52
6.	Thin Fog	1	4.74
7.	Light Fog	0.500	8.32
8.	Moderate Fog	0.250	15.64
9.	Thick Fog	0.1	39.1
10.	Dense Fog	0.05	78.2

For λ=980nm

Table.6

Sl. No.	Weather Condition	Visibility Range (Km)	Loss(Db/Km) for 980 nm
1.	Extremely Clear Weather	50	0.2
2.	Very Clear	25	0.33
3.	Clear	10	0.83
4.	Light haze	5	1.51
5.	Haze	2	2.87
6.	Thin Fog	1	5.22
7.	Light Fog	0.500	8.58
8.	Moderate Fog	0.250	15.64

9.	Thick Fog	0.1	39.1
10.	Dense Fog	0.05	78.2

3.3.3.2. Rain

Rainfall-related attenuation, which is a nonselective scattering, occurs. This kind of attenuation does not rely on the wavelength [53]. Rain has the capacity to create laser delivery fluctuation effects. The amount of rain affects how visible the FSO system is. As a result of the optical beam being absorbed, dispersed, and reflected in cases of heavy rain, water droplets have a solid composition and can either change the optical beam properties or hinder the passage of the beam [52]. When it rains, the rain's water droplets disrupt the free space optical connection. With an increase in rainfall, attenuation also rises. Because the radius of a raindrop (200 m to 2000 m) is significantly larger than the optical signal utilised in FSO communication, it generally has less of an influence on optical signals.

The attenuation due to rainfall rate of W is given by,

A_{min}= 1.076 $W^{0.67}$ ....(ix)

Case-1.Rainfall W= 25mm/hr

A_{min}= 1.076X$25^{0.67}$

Attenuation (dB/km)= 9.29 dB/km

Case-2, Rainfall =50mm/hr

A_{min}= 1.076X$50^{0.67 =}$ 13.75 dB

Case-3. Rain rate 100mm/hr

A_{min}= 1.076 X $100^{0.67}$ = 23.47 dB/km

loss resulting from based on the computation above and Table 7, which summarises the loss for various rain rates, several rain rates can be determined.

Table.7. Attenuation due to Rain

Sl. No.	**Rain Rate(mm/hr)**	**Loss(dB/Km)**
1.	5	3.16
2.	10	5.03
3.	15	6.6
4.	20	8.0
5.	25	9.29
6.	30	10.5
7.	35	11.7
8.	40	12.74
9.	45	13.75
10.	50	14.80
11.	55	15.77
12.	60	16.72
13.	65	17.65
14.	70	18.53
15.	75	19.41
16.	80	20.27
17.	85	21.11
18.	90	21.93
19.	95	22.74
20.	100	23.47

SNR and BER calculated with the help of following formula [55],

$$\text{SNR} = \frac{P_R}{\text{NEP}\sqrt{\Delta f}} \qquad \text{(x)}$$

and

$$BER_{NRZ-OOK} = \left(\frac{1}{2}\right) erfc\left(\left(\frac{1}{2\sqrt{2}}\right)\sqrt{SNR}\right) \qquad \text{(xi)}$$

3.3.3.3. Haze

Haze particles can linger in the atmosphere for a longer period of time, which causes atmospheric attenuation. As a result, attenuation values depend on the current visibility level. There are two approaches to collect data on attenuation for evaluating the effectiveness of FSO systems: first, by temporarily installing system at the site and evaluating its efficacy; and second, by utilising Kim and Kruse model [53].

3.3.3.4. Smoke

It is produced from the burning of several chemicals, including carbon, glycerol, and home emissions. It has an impact on the medium's visibility [54].

3.3.3.5. Sandstorms

The most common issue with outside connection communication is sandstorms. These may be identified in two ways: first, by the size of the wind particles, which relies on the texture of the soil, and second, by the required wind speed to blow the particles up in the shortest amount of time [55].

3.3.3.6. Clouds

The majority of Earth's atmosphere is made up of cloud layers. Water condenses or deposits itself above the earth's surface to create clouds. The optical beam portions that are transferred from the earth to space might be fully blocked by it. Because of the variety and inhomogeneity of the cloud particles, it is challenging to determine the attenuation brought on by clouds [56].

3.3.3.7. Snow

The bigger particles in snow are what contribute to the geometric scattering. The impact of the snow particles is comparable to Rayleigh scattering [57].

3.3.4. Atmospheric Turbulence Induced Fading

The air loss related to vision is minimal when there is a clear sky, but there is additional negative consequence known as scintillation or fading. Variations in the air's refractive index along the transmission channel are brought on by in homogeneities non the temperature and pressure of the atmosphere, which are brought on by solar heating and wind [47] [48].

Channel fading, also known as random changes in the amplitude and phase of the received signal, is the result of the resultant air turbulence. This causes a significant decrease in system performance, especially for transmissions over long distances of several kilometres [47] [49].

3.4. Scattering of Light

Due to the non-uniformities in the medium, certain radiation forms diverge from their intended course. Scattering is the name for this deviation process.

One of the most significant phenomena we see every day is light scattering. Everyone has witnessed these phenomena since they were little, just like they did with the colour of the rainbow and the blue sky. In contrast to reflection and refraction, light dispersion is a totally separate phenomenon. Light travels in a straight line when it is reflected, however when it is dispersed, the medium it is travelling through scatters the light in many directions.

The scattering of light, which we refer to as an optical phenomenon like the sky's blue colour, is a result of the process by which microscopic particles in the atmosphere cause the light to go in different directions.

As an illustration, when light strikes airborne particles, some of the light is absorbed and the remainder is radiated in all directions other than the one from which it originated. The term "scattering of light" describes this. The light's wavelength and the size of the particle that dispersed it both have a role in determining how strong the scattering is.

For instance, when the sun's rays hit airborne particles on Earth, they are impacted. In addition to being scattered in all directions, some of these photons are absorbed by the particles. The provided figure shows how this is. In light of this, it may be claimed that particles, imperfections, or interference between the two mediums might cause light to be diverted off its incident path. As a result, dispersion is increased by light with shorter wavelengths and higher frequencies.

Similar to how light scatters when it interacts with raindrops, light's physical origin is light colliding with moisture. But when droplet size shrinks, scattering changes in both kind and quantity. Greater scatter is produced by smaller droplets, particularly more backscatter from headlights, which is also bigger and causes more loss of contrast. The use of high beam when driving in fog is discouraged for this reason.

Based on a dimensionless size parameter, light scattering models may be separated into three domains, α which is defined as equation 3

$$\alpha = \Pi d/\lambda \ldots\ldots\ldots\ldots\ldots\ldots\ldots\ldots. \text{(xii)}$$

where ΠDp is the circumference of a particle and λ is the wavelength of incident radiation. Based on the value of α, scattering can be classified as

$\alpha << 1$: Rayleigh scattering (small particle compared to wavelength of light);

$\alpha \approx 1$: Mie scattering (particle about the same size as wavelength of light, valid only for spheres);

$\alpha >> 1$: Geometric scattering (particle much larger than wavelength of light).

As the object is scattering in fog. So, the discussion will be about Rayleigh scattering and Mie scattering [28].

3.4.1. Rayleigh Scattering

Electric and magnetic field vectors serve as the defining features of light as an electromagnetic wave. For the sake of simplicity, it is assumed that the incident wave is a plane wave that is linearly polarised and hits a tiny spherical particle. About 0.5 m is the wavelength of light in the visible spectrum. The local electric field created by the wave is roughly homogeneous at any given time for particles much smaller than the wavelength. A dipole is created in the particle by the applied electric field. The induced dipole also oscillates in response to the electric field, and in accordance with classical theory, the dipole radiates in all directions. The term "Rayleigh scattering" refers to this kind of scattering.

The dipole moment “P” induced in the particle is proportional to the instantaneous electric field vector as equation 4.

$$P = \alpha E \ldots\ldots\ldots\ldots\ldots\ldots\ldots \text{(xii)}$$

Polarization is described in this statement. , which is a scalar for every isotropic spherical particle and has the dimension of volume. It is possible to get an expression for the intensity of scattered radiation as equation 5 from the energy of electric field generated by the oscillating dipole.

$$I=(1+\cos2\theta)k4\alpha_2 2R2/I_0 \ldots\ldots\ldots\ldots\ldots\ldots.. \text{(xiv)}$$

R= Distance to the particle;

θ= Scattering angle;

α= scalar (value depends on refractive index);

k= wave number = 2π/λ;

I_0= Initial intensity of the light.

With equal peaks and minima in the forward and backward directions, as well as a minimum at a right angle, the scattering is symmetrical with regard to the direction of the incident beam.

The intensity of the scattered light varies inversely with the fourth power of the wavelength, with blue light (short wavelength) scattering more frequently than red [29].

3.4.2. Mie Scattering

The generalised solution, known as the Mie scattering theory, illustrates how an electromagnetic wave might be scattered by a homogeneous, spherical material with a different RI than the medium the wave is travelling through. The fact that Mie scattering is not a stand-alone physical event should be emphasised once more. Due to the electric polarisation of the molecules in the scattering particles, the Maxwell's equations for multipole radiation can only be solved definitively when an electromagnetic wave strikes the system. It provides scattering solutions where the phase of the input signal may even fluctuate noticeably within the scattering particle's diameter. As a result, it differs from Rayleigh scattering in that it does not need that the $2\pi d/\lambda \ll 1$ requirement be satisfied. Following the Mie solution, frequent scattering factors for waves that are propagating include dust, smoke, and raindrop particles.

The Mie solution is a multipole polarisation expansion that occurs infinitely many times as a result of an incoming wave in a spherical media. Infinite series, with each member denoting the contribution of a certain order of multipole expansion, is another way to depict the electric and magnetic field of such polarisation. Now, keep in mind that you may estimate the power spread in any direction from the vector pointing in that direction. The pointing vector may also be determined, just like we did for Rayleigh scattering, if the formula for the fields E and H is well understood. As a result, the cross section may likewise be determined by using these formulae for any specific direction once the expressions for E and H are known. For finding the Mie solution, there are several effective methods available today (Hergert and Wriedt, 2012). The book isn't intended to address how to find the Mie solutions, though. We won't examine the aspects of the solution here; instead, we'll just state the formulas for the scattering cross sections that were derived.

For big particles, the square of the particle diameter determines the Mie scattering intensity. The light beam turned toward the direction the incident light ray was coming from after being scattered by a particle. Dust particles exhibit the majority of this form of scattering. Even still, this form of scattering is less common in fog because of the abundance of tiny water droplets in the sky. Rayleigh and Mie scattering are shown in Fig.3.3.

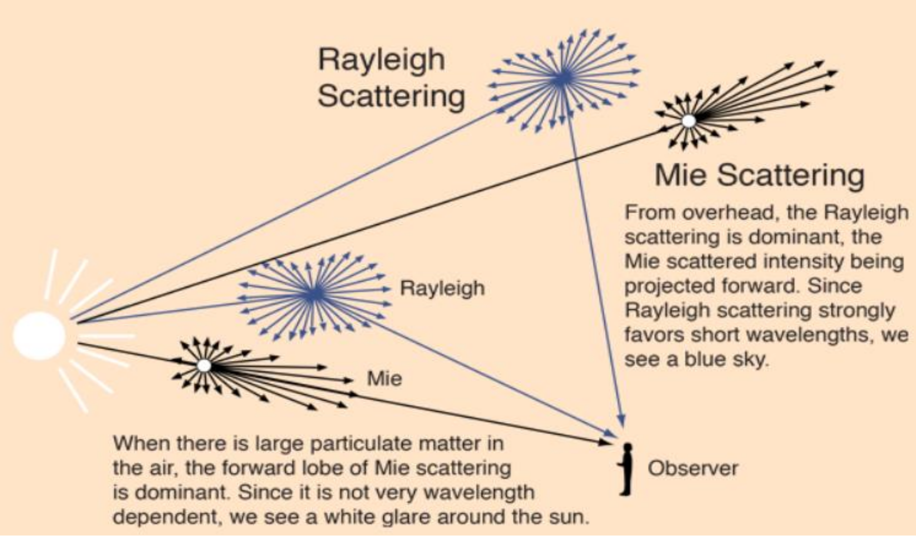

Fig. 3.5. Rayleigh and Mie scattering

The Mie scattering intensity for large particles is determined by the square of the particle diameter. After being scattered by a particle, the light beam shifted to face the incident light ray's direction. The bulk of this scattering is shown by dust particles. Due to the amount of microscopic water droplets in the sky, this type of dispersion is still less frequent in fog.

When air particle become very small, the situation is more complicated because not all wavelength is affected equally. Air molecules, for example, scatter short wavelength (blue) more [28].

3.4.3. Geometric Scattering

This is a phenomenon that occurs when photons collide with the structure of a particle in free space, but because airborne particles behave differently than those that are scattered above, this sort of scattering will be unique as well.

Geometric scattering is the term for the sort of scattering that occurs when a suspended particle has a size greater than the visible light spectrum, which has a wavelength of around 400–780 nm. Because the scattering becomes directed and unpredictable as a result of the particle size exceeding the light's wavelength, the pattern of the scattering is substantially altered. A lob-like shape with a predominance of scattering in the forward direction characterises the new kind of scattering. As in Rayleigh's scattering, the pattern is very directional, which aids in understanding that in the case of rain, which falls under this type of scattering. However, unlike Rayleigh's scattering, where the scattering is uniform in all directions due to the particles' extreme smallness in relation to the wavelength of light. Although photons are scattered via raindrops in many directions and the size of the droplets makes an assumption about the scattering, most of the scattering is facade. Fig.3.4. shows the scattering pattern of geometrical scattering.

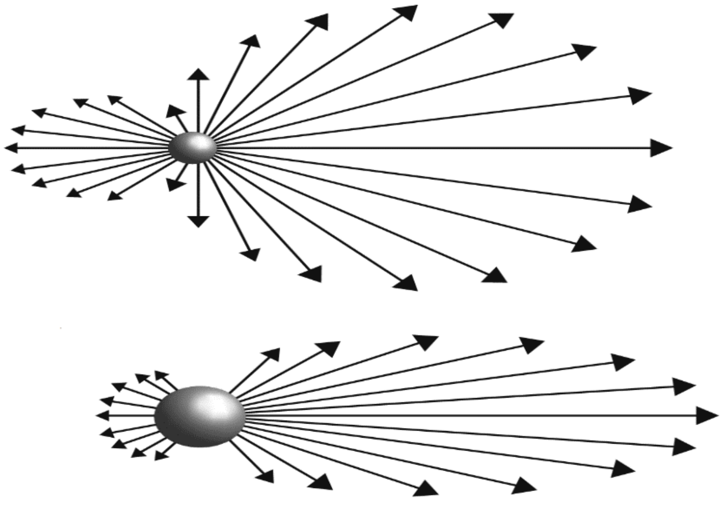

Fig.3.6. Geometrical scattering

Chapter 4 – Design of Communication Channel in FSO

4.1. Introduction

In modem networks, optical communications have given rise to previously unheard-of capacity. Wide-band fiber-optic networks now cover the whole world as a result of investments made in response to the Internet's explosive expansion. The optical communications revolution has also sparked the creation of cutting-edge technologies that have uses outside of traditional telecom. One application that might profit from these most recent developments is free-space laser communications, or lasercom. With the ability to bridge billion-kilometer links at Megabit/sec (Mbps) data speeds, free-space optical networks have the potential to encircle the planet with adaptable and agile wide-band lasercom that could extend to the moon, Mars, and beyond [70-71]. The major focus of this work is on photon-efficient transmitters and receivers that may extend unrepeated links beyond ultra-long-haul lengths greater than the net fibre already installed on Earth.

The effectiveness and sensitivity of optical transmitters and receivers directly affect the performance of free-space laser communication. But up until recently, these aspects did not play a major role in the development of fiber-optic networks. However, more sensitive receivers have emerged as a method of enhancing network performance in terms of power and bandwidth efficiency as the apparent need for bandwidth has reached the limits of installed fiber-optic lines. As a result, needs for fiber- and free-space-based technologies are beginning to converge. High-sensitivity photon-efficient transmitter and receiver designs can lessen the need for mid-span amplifiers, lessen nonlinear impairments, and increase link distances in fibre networks, but they are especially helpful for free space optical (FSO) communication because improvements in receiver sensitivity directly reduce transmitted power requirements, which in turn can result in significant size, weight, power (SWAP), and cost reductions.

Compared to radio-frequency (RF) and fiber-optic linkages, free-space optical links provide a number of noteworthy benefits, including more design and optimization options for transmitters and receivers. Particularly in space-based applications where there is no atmospheric absorption, these include the lack of channel dispersion and nonlinearities, as well as almost infinite channel bandwidth. These features enable FSO transmitter (TX) and receiver (RX) designs to take advantage of the average-power-limited characteristics of optical transmitters to generate optimised signalling waveforms [72–77], which, when used in conjunction with photon-efficient modulation formats, can significantly increase link efficiency, η_{link}. Energy consumption per received bit, or [J/bit], is a useful indicator of η_{link} performance.

4.2. Data Communication Channel

The Laser driver switches the DPSS Laser in accordance with the incoming TTL signal using the modulated TTL output from the Arbitrary waveform generator. The Laser driver comprises of MOSFET driver and a MOSFET unit which is used the switching the Laser module. Fig.4.1. shows block diagram of FSO Data Communication Channel.

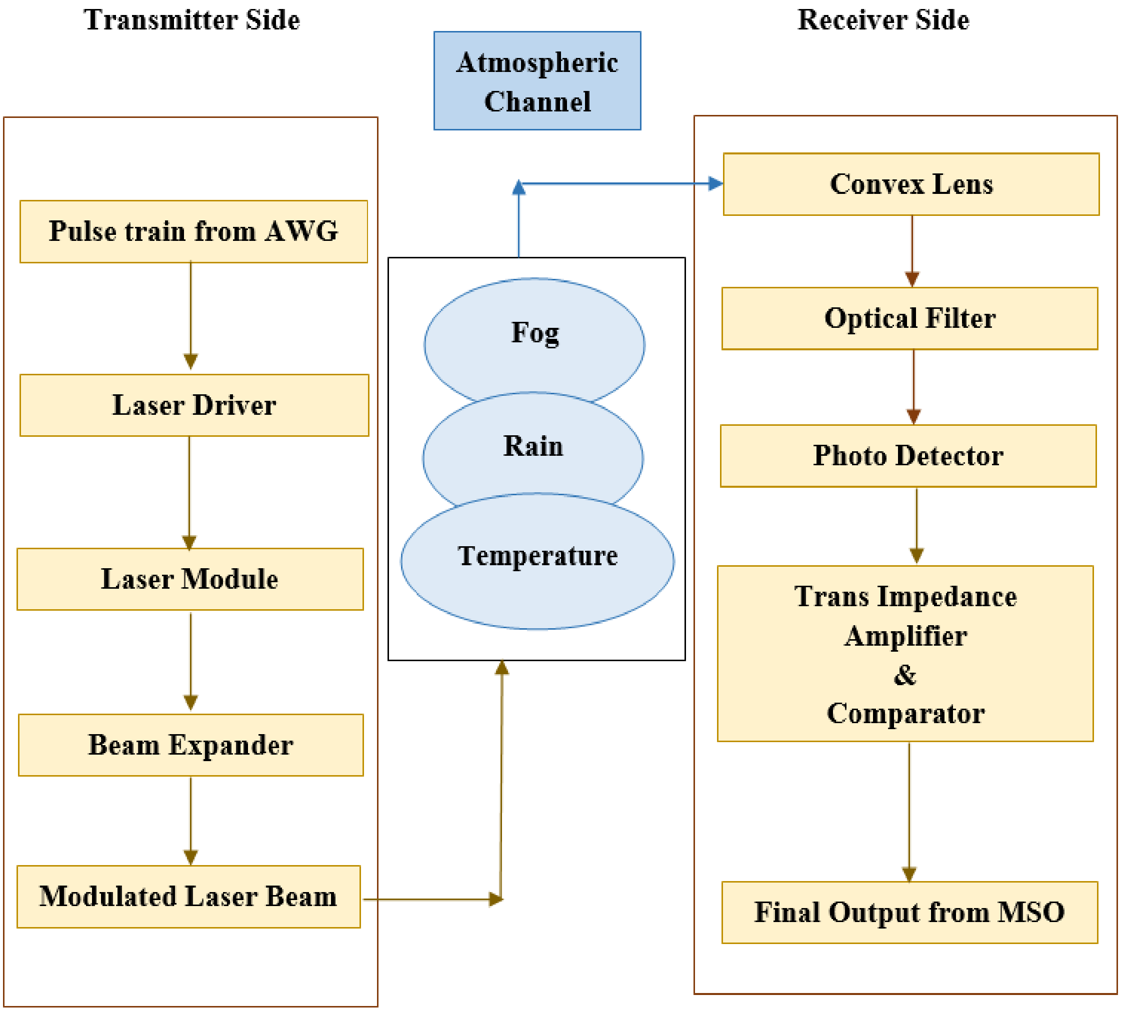

Fig.4.1. Block Diagram of FSO Data Communication Channel

As the AWG is provided the TTL signal to the MOSFET Driver and the MOSFET is connected according to the MOSFET driver, as a result the MOSFET is on off, according to the TTL input signal. Mainly, Intensity Modulation has been done by this process. The modulated Laser beam is transmitted through a beam expander. The main functioning of the beam expander is reduced the optical beam expansion at the receiver side according to its magnification factor. A wireless connection with a range of 25 m is used for the free space channel and a line of sight is an essential condition for this.

Through this conduit, the optical beam can reach the appropriately positioned photo detection equipment. The Trans-impedance amplifier stage comes after the photo detector system and amplifies as well as transforms the input current level from the photo detector to the appropriate voltage level, whose operating frequency and slew rate are selected in accordance with the frequency of the signal. A convex lens should be used for the longer range operation to reduce the beam expansion loss and collimate the laser beam accordingly. The collimated Laser beam is fall into the photodetector unit and signal is processed as per block diagram and finally, the output signal has been captured from the comparator and transimpedance side through a Mixed Signal Oscilloscope (MSO), model no. MSOS054A, Keysight. The optical signal power has been measured by an Optical power meter, Ophir, Vega.

4.2.1. Transmitter Unit of Data Transmission

The +5 V supply is provided to the MOSFET driver circuit and a TTL signal is provided as a input to the MOSFET driver (through a BNC connector BN1) with respect to ground, the output of the driver (TTL Pulses) is provided to the gate of the MOSFET through a resistor. The source of the MOSFET is grounded and the output from the drain is connected to the one pin of the two pin connector (CN2) unit. Another pin (CN2) is connected to the 5V supply.

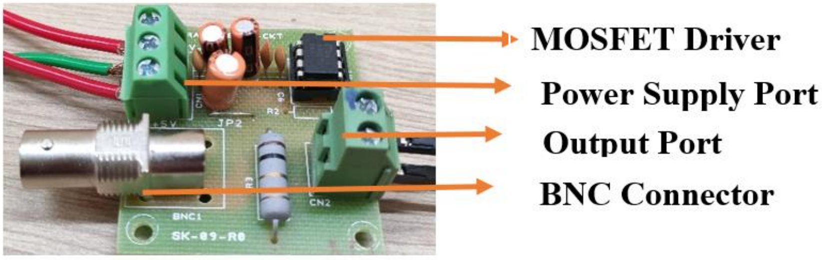

Fig.4.2. MOSFET driver circuit

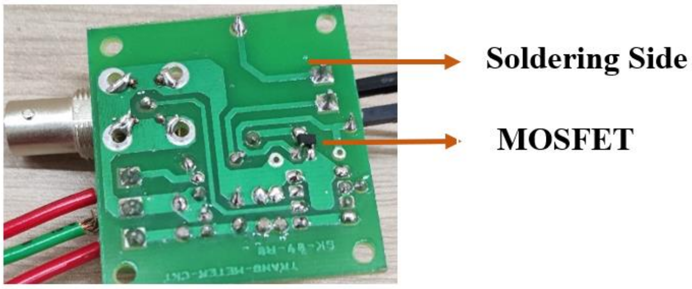

Fig.4.3. MOSFET circuit

According to the TTL pulses is coming from the MOSFET driver, the MOSFET works accordingly. The output has been tapped from two port connector (CN2) which is fed to the LASER module. According to the output, the LASER is switched on off accordingly. Fig.4.2. and fig.4.3. show the transmitter side MOSFET driver and MOSFET circuit. Fig.4.4. shows the schematic layout of Laser Driver and fig.4.5. shows the transmission side of data communication.

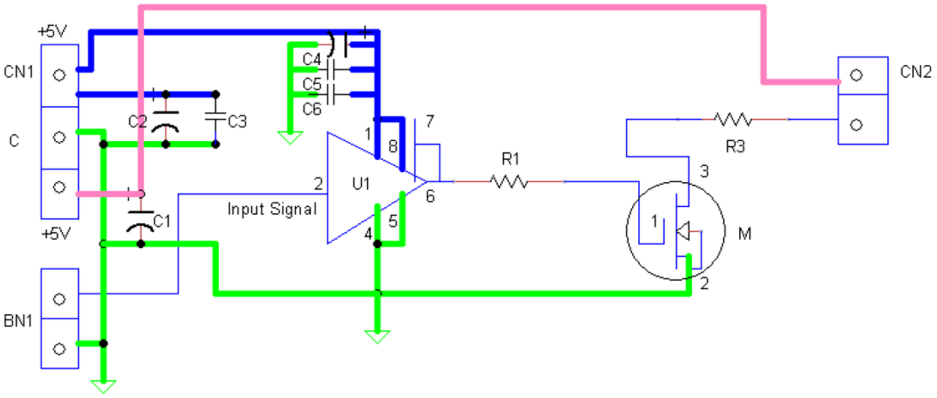

Fig.4.4. Schematic layout of Laser Driver

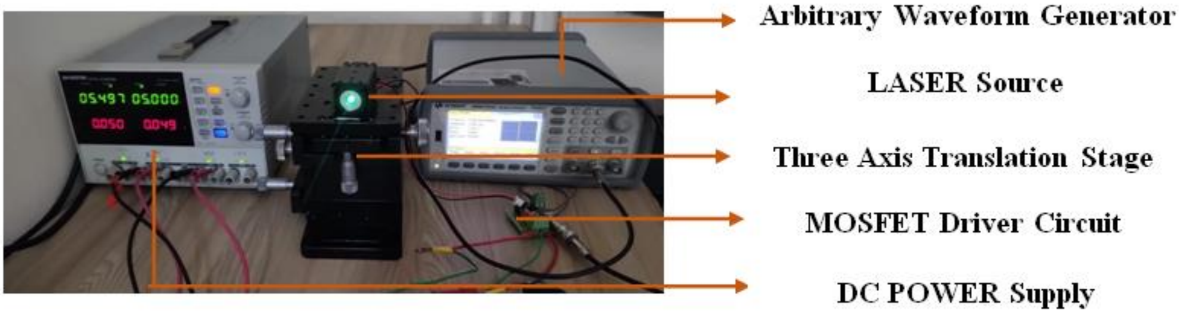

Fig.4.5. Transmission Side of Data Communication

4.2.2. Receiver Unit of Data Transmission

The trans-impedance amplifier is used for amplify the captured photodetector signal and convert the photodetector current signal into voltage signal. The photodetector signal (PD IN) is fed to the inverter terminal of the U1A which is a high speed op-amp. The value of R3 and C10 has been chosen according to the bandwidth requirement of the system. As the photodetector signal is fed to the inverting terminal of U1A, the signal is inverted. This inverted signal is not comparable with comparator unit, so, this signal is inverted in another stage (U1B), as a result this amplified signal is similar of photodetector signal (PD IN) which was not the amplified signal. The second stage has been configured as a unity gain. This signal is fed to the high speed comparator (U2) non inverting side, and a minimum threshold value is set for the accurate operation of the comparator. Two voltage regulator has been used U3 and U4 for positive supply regulator and negative supply regulator respectively for proper functioning of the U1A, U1B, U2 respectively. Fig.4.6. shows Schematic layout of the trans-impedance amplifier and fig.4.7. shows Trans-impedance and comparator unit and fig.4.8. shows the 4.8. receiver side of data communication.

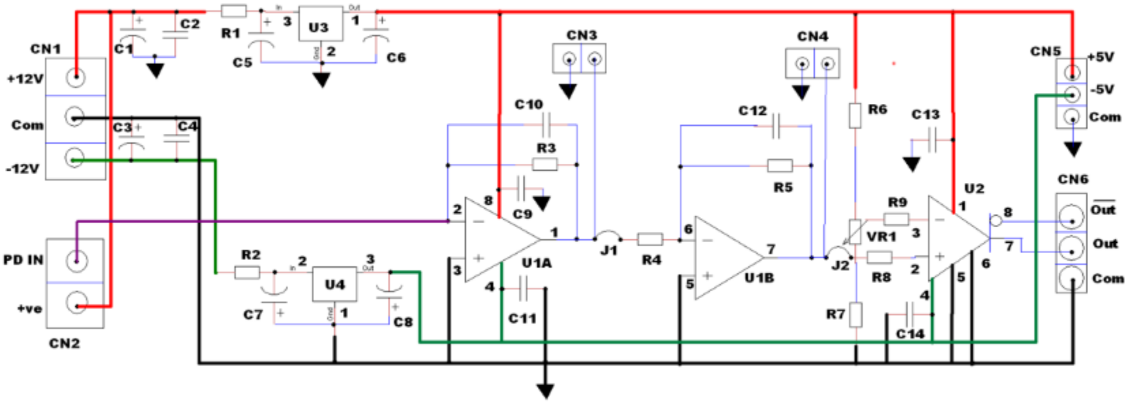

Fig.4.6. Schematic layout of the trans-impedance amplifier

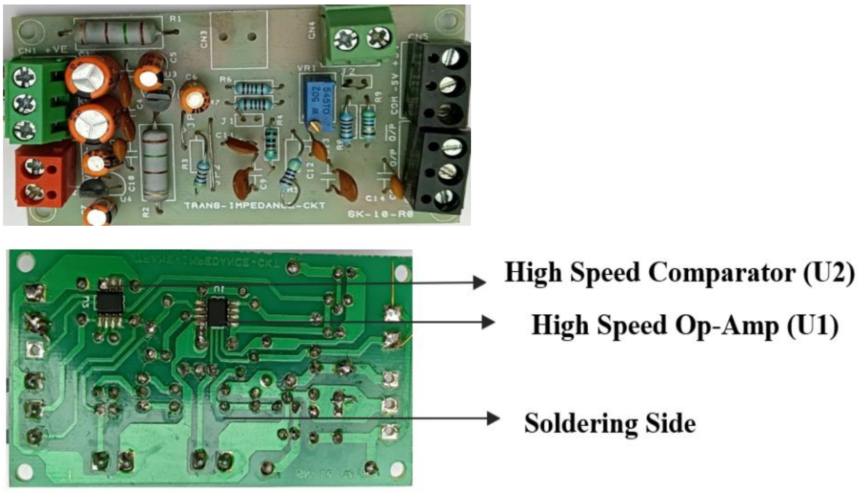

Fig.4.7. Trans-impedance and comparator unit

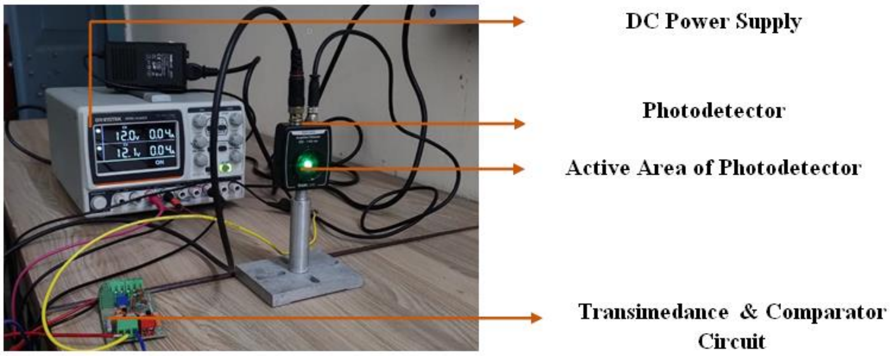

Fig.4.8. Receiver Side of Data Communication

4.3. Voice Communication Channel

An automated gain controller device receives audio signal input from the microphone and feeds it to the pre-amplifier. After that, the amplifier unit receives the pre-amplified audio stream. To create a PWM signal, the triangle wave signal and the amplified audio signal are compared. The generated PWM signal is fed to the Laser Driver and finally the modulated Laser beam is passed through the beam expander and propagated through a free space and finally it is fallen to the convex lens and followed by an optical filter, and then the optical signal is captured through the photodetector and then the signal is passed through a high speed opto-coupler which is a highly noise immune. Then this signal is fed to the comparator unit. The comparator unit is providing the proper wave shaping, minimum threshold value. Then it is passed through the buffer unit. Its purpose is to offer enough driving capability to transfer signals to a subsequent step. Then the signal is passes through low pass filter which is filter out the noise. The signal power is reduced as an audio signal without changed the actual waveform which is fed to the speaker. This attenuated signal is less harmful for speaker as well. Fig.4.9. shows the block diagram of FSO voice communication channel.

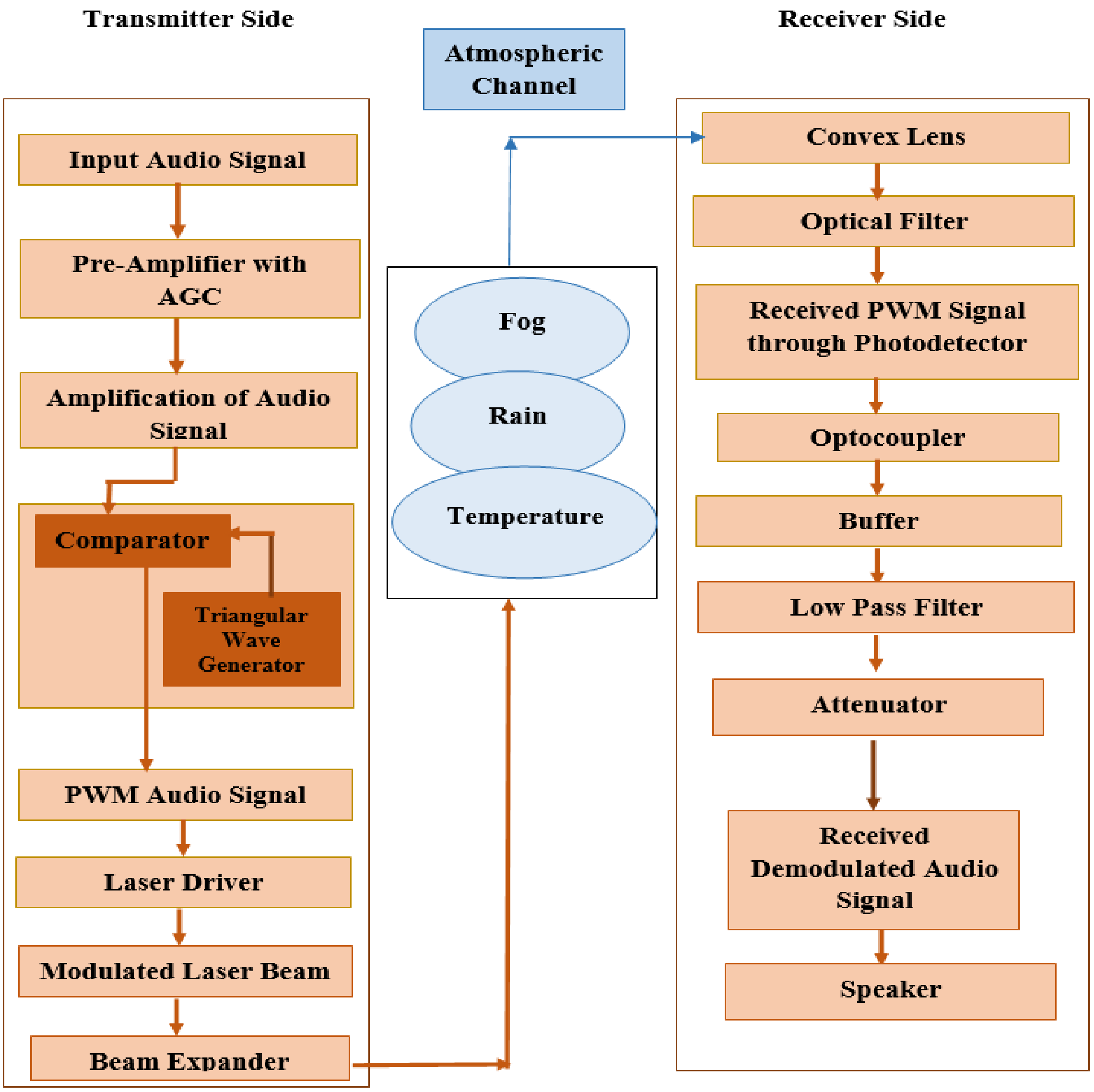

Fig.4.9. Block Diagram of FSO Voice Communication Channel

4.3.1. Modulator Unit of Voice Transmission

Before being supplied to the pre-amplifier with AGC unit, the input audio signal (as a message signal) has first been routed via a 10 µF electrolytic capacitor (C5) to reduce DC bias. The N-channel JFET Q1 controls the gain of the operational amplifier U1A (TL082). Op-amp U1B (TL082) amplified a portion of the output voltage of U1A, and after passing it through a half-wave rectifier to produce negative voltage, it was sent to the gate of JFET Q1 to create a signal.

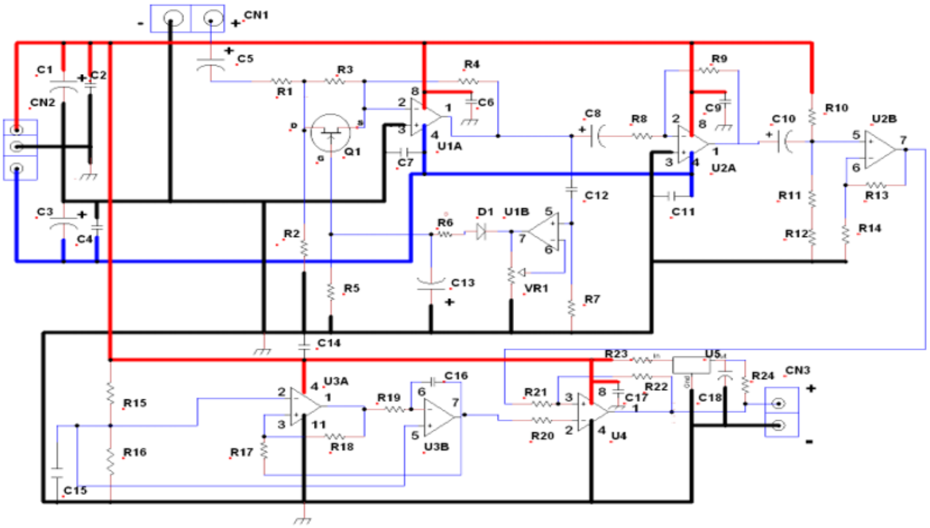

Fig.4.10. Schematic layout of the voice transmitter circuit

The drain-source resistance of the JFET grows, the gain of the op-amp U1A falls, and the output voltage lowers when the output voltage of the op-amp U1A rises and the negative gate voltage rises as well. Therefore, the gain is automatically regulated. fig.4.10. shows schematic layout of the voice transmitter circuit and fig.4.11. shows audio modulator circuit.

Fig.4.11. Audio Modulator Circuit

The pre-amplified audio signal is fed through an inverting amplifier U2A (LM358) before being routed to a non-inverting amplifier U2B (LM358) with additional DC bias. Fig.4.12. shows the audio signal with pre-amplification signal.

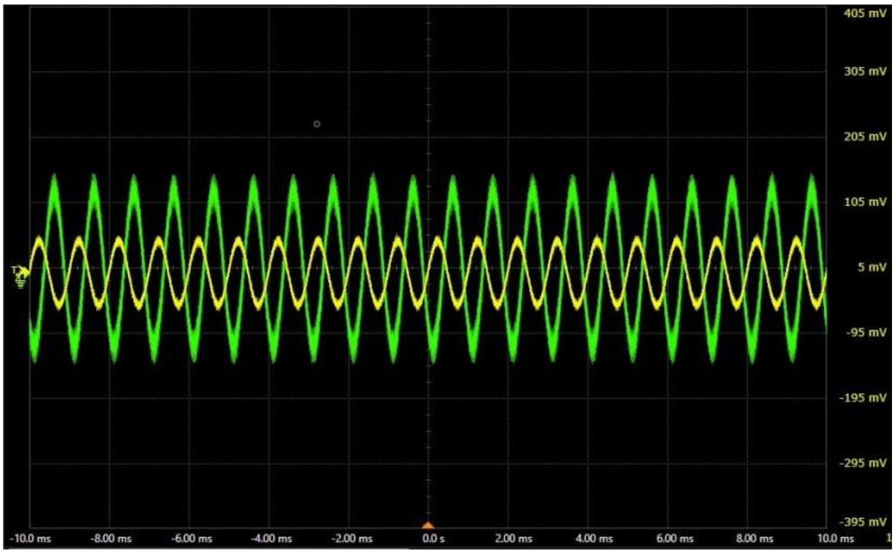

Fig.4.12. Audio signal with pre-amplification

The audio signal has a DC bias added to it prior to amplification. The amplified audio signal is then supplied to a comparator U4 (LM393), where it is compared to a 63 kHz triangle wave signal (carrier signal) to produce a 63 kHz PWM signal. Fig.4.13. shows the triangular wave form and output PWM signal with 63 kHz

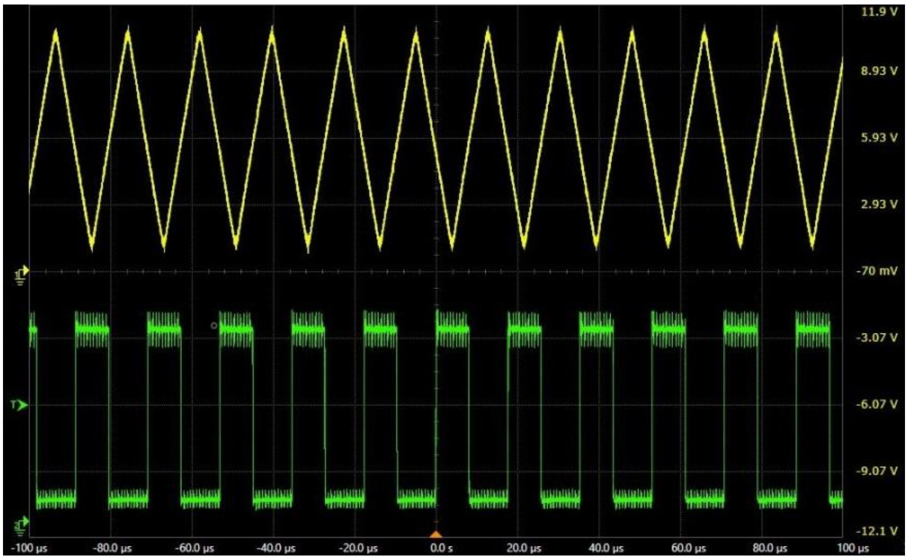

Fig.4.13. Triangular wave form and output PWM signal with 61 kHz

Using op-amp U3, a triangle waves of 63 kHz was produced (OP462). The duty cycle of the PWM signal will vary immediately along with the loudness of the audio signal. The modulator circuit produces a 63 kHz square wave signal in the absence of audio input.

Fig.4.14. shows generated PWM signal with audio and amplified audio signal. Fig.4.15. shows the transmission side of voice communication.

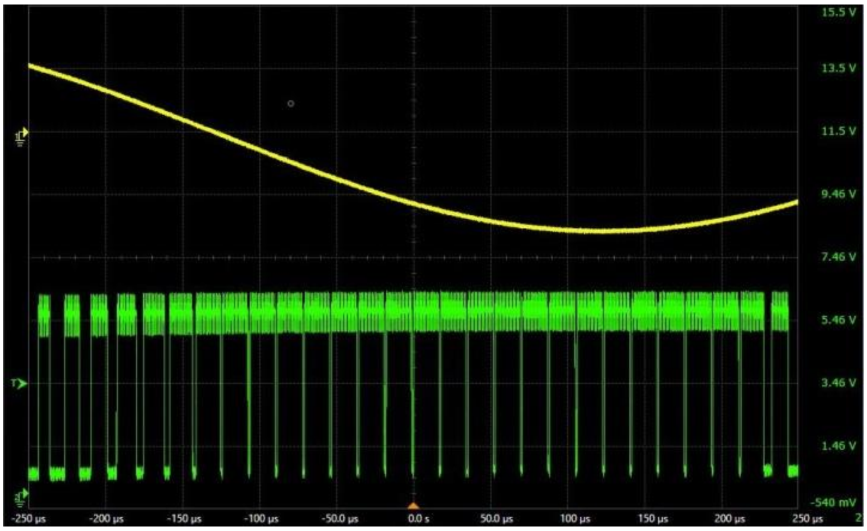

Fig.4.14. Generated PWM signal with Audio and amplified Audio signal

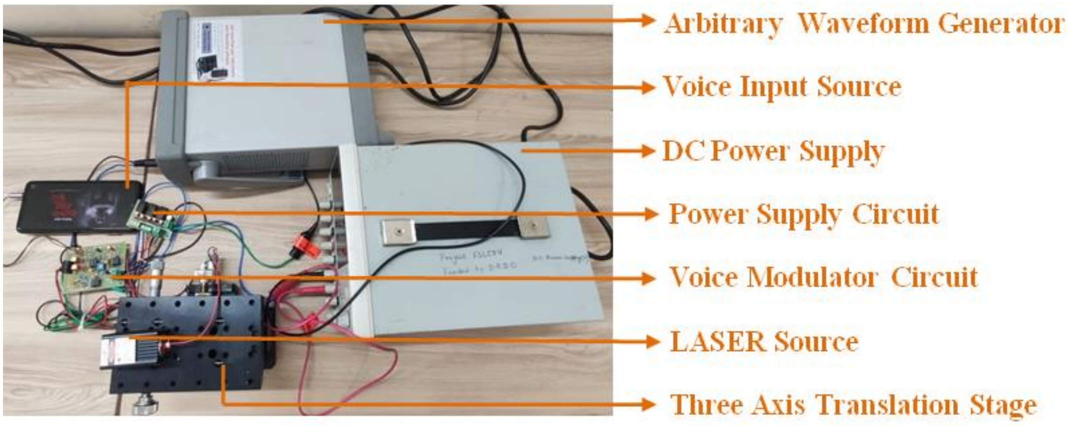

Fig.4.15. Transmission Side of Voice Communication

4.3.2. Demodulator unit of Voice transmission

The received signal is fed to the CN3 and supply has been given to the opto-coupler (U6).

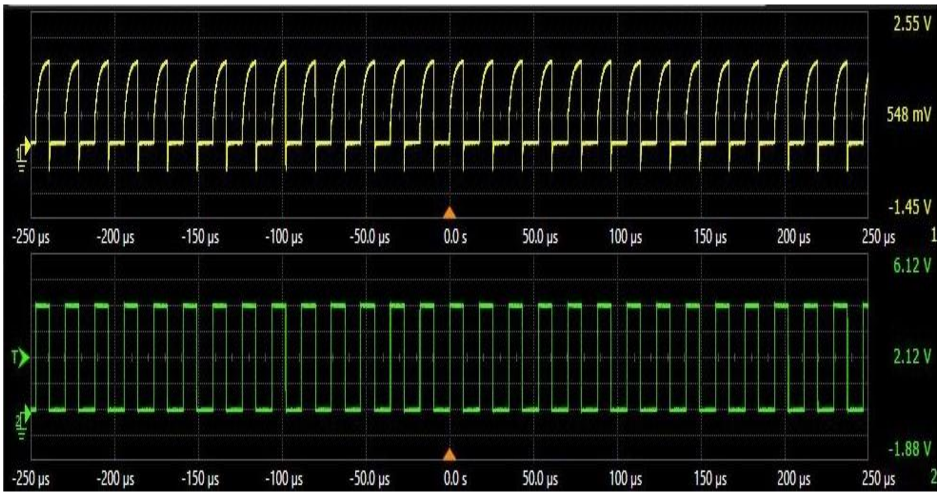

Fig.4.16. Received PWM signal from the photo detector and comparator side (without audio signal)

Fig.4.16. shows the received PWM signal from the photo detector and comparator side (without audio signal), fig.4.17. shows the received PWM signal from the opto-coupler and comparator side (with audio signal).

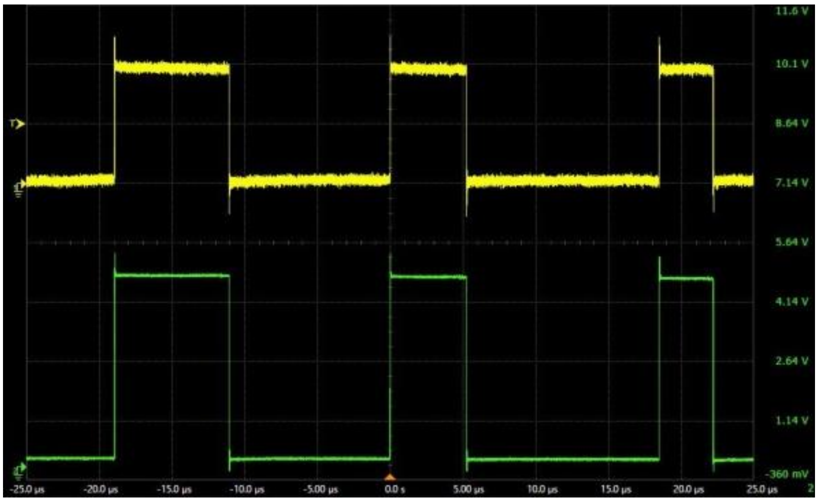

fig.4.17. Received PWM signal from the opto-coupler and comparator side (with audio signal)

The output of the opto-coupler (from the pin 6) is fed to the inverting terminal of the op-amp of pin 2. This is amplifying the signal, after amplification, this is fed to the comparator unit (U2) which is provided the perfect square wave. After that, this signal is fed to the buffer (U3) to offer enough driving capability to transfer signals to a subsequent step.

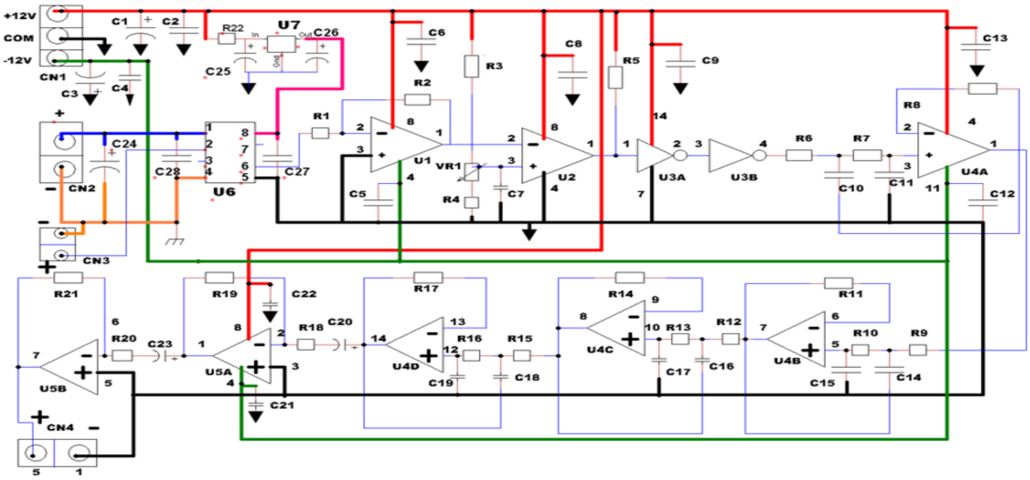

Fig.4.18. Schematic layout of the audio demodulator circuit

To make it noise free signal, this buffer signal is fed to the low pass higher order filter (U4) and finally this noise free signal is attenuated by the attenuator (U5). This attenuated signal is received in CN4, which is the actually demodulated audio signal and This audio signal goes to the speaker. Fig.4.18. shows schematic layout of the audio demodulator circuit and fig.4.19. audio demodulator circuit.

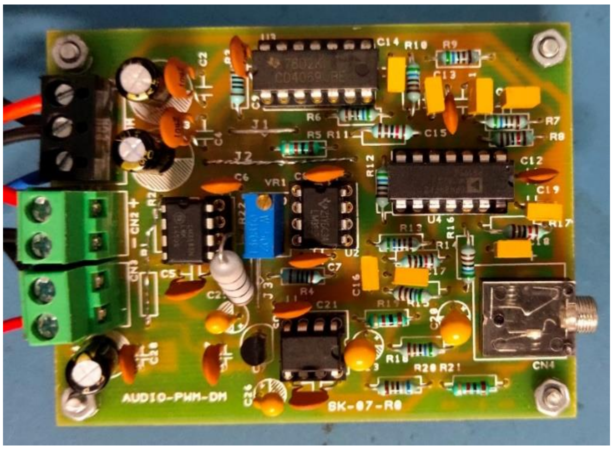

Fig.4.19. Audio Demodulator Circuit

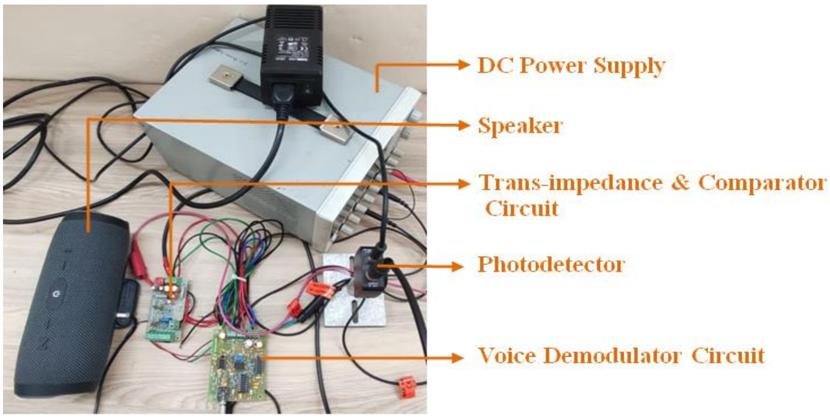

Fig.4.20. Receiver Side of Voice Communication

Chapter 5 – Artificial Simulation Setup

5.1. Introduction

The goal of the communication system is to send data or information reliably and at a low acceptance error rate from a transmitter to a receiver via an air channel between two points. In this specific experiment, DPSS (Diode Pumped Solid State) lasers of the same sort are employed. In this series of studies, the transmitter is made up of various lasers, each of which has its own laser module and laser driver. The laser driver draws 12V, while the modules for the 638 nm, 808 nm, and 980 nm lasers require roughly 2.5V and 532 nm laser 5V, respectively. In this particular experiment setup, 5MHz is formed, but the transmitting signal may vary in each sub-part of the experimental condition due to the formation of the laser driver which modulates the signal and another reason is the oscillator used in this experiment is AWG where the transmitting frequency is changeable. The modulator converts bits of information into electrical signals and modulates the laser to generate an optical signal. A receiver collects the optical signal after it has travelled through the air channel and recovered the data. On the receiver side, a detector and a decoder are used to extract the signal. In this experiment, the photodetector serves as the decoder, converting the optical signal back into an electrical signal. Consequently, using the modulator and laser module to beam light at certain wavelengths of 532 nm, 638 nm, 808 nm, and 980 nm sequentially, the extended experiment will be carried out. The photodetector is positioned to demodulate the frequency carried laser beam as the modulated beam is received at the other side, which is the receiver end. The modulated beam will travel through intentionally generated rain, fog, and temperature. The signal is then created and examined in detail in order to have a full understanding of how the laser beam attenuates and loses the data that is being conveyed.

5.2. Temperature

For this experiment six hollow wooden boxes were made. Each of the six boxes is 3 feet in length, 1 feet in width and 1 feet in height. Out of six boxes this design has been made for the four boxes in the middle which are completely open two sides and other three sides out of four sides have one glass window on each side. Remaining one side of the wooden box is completely closed because that side is placed on the wooden bench. Each glass window are 1 feet in length, 0.5 feet in width and 0.25 feet distance from edge to edge of three sides. The other two boxes on the extreme side have the same design, one side of the box is completely open and the exact opposite side has a square shape glass window of which each side has 0.25 feet. When all the boxes are merged, then this window of the two side works as inward and outward way of this wooden box. Each small box is numbered for the convenience of the experiment. Outside of every small box is coated with sunmica and inside of the box is painted with heat-resistant black color to prevent any unexpected incidents during the experiment as well as glass to these windows are also resist the heat. Each small box is completely attached as well as aligned to the other box and in order to prevent the movement of the air through the sticking parts, the boxes are fully air sealed by using gas blocking strip. As a result, the outside weather cannot affect during the experiment. For this system setup we will get the results of our experiment with more accuracy. If the small boxes are arranged in a row regarding their serial number, the length of the newly formed box is 18 feet. These 18 feet is the main core focused region of our experiment. Each small box is placed on the wooden bench and each wooden bench is 3 feet long, 1 feet width and 2 feet height from the ground. In order to keep the glass windows, we can compare the weather inside the wooden box with the atmospheric weather for the purpose of experiment. Fig.5.1. shows the arrangement for artificial temperature experiment.

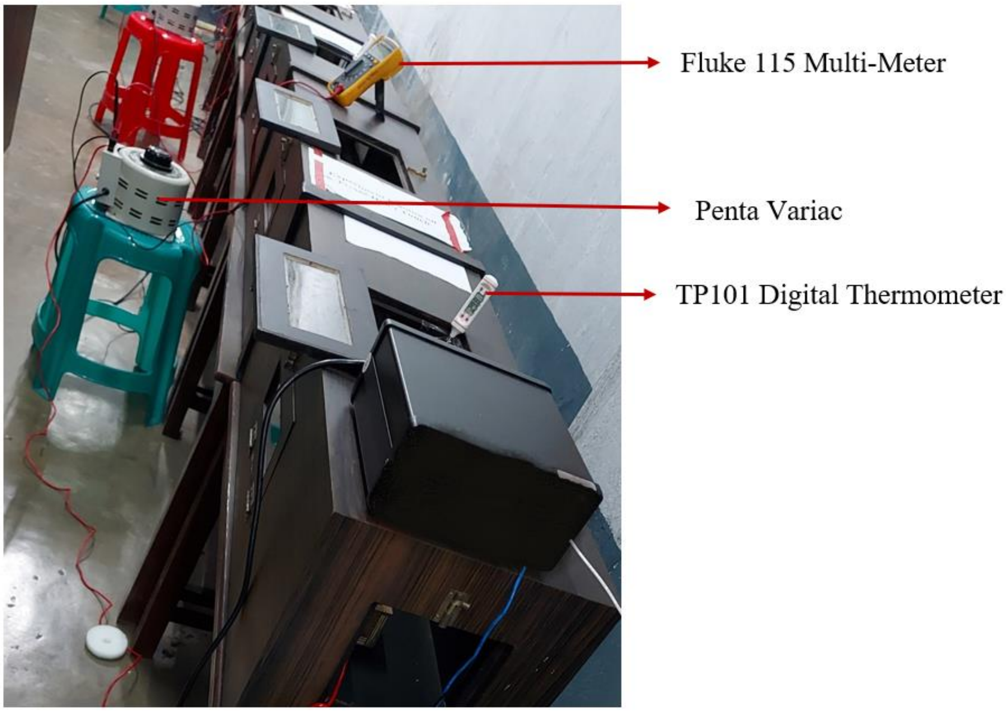

Fig.5.1. Arrangement for artificial temperature experiment

After that, three top side open boxes are made with plywood and coated with sunmica and inside of the box is painted with heat-resistant black color to prevent any unexpected incident which may occurs during the experiment. With help of the screw, 1500-watt coper coil tied up the longest side of these opened box and 4mm wire is joined permanently with the part of the screw that sticks out. During this experiment, the temperature of the copper coil will be very high, and if the heated coil touches the floor of the wooden box, it may catch fire. For these reason, ceramic mounting pole is used to keep the heated coil untouched with wooden box. Here all the three top side open boxes are arranged in the same way and 4mm wire is permanently added to each box, one side of these copper coil is positive side, another side of the copper coil is negative side. Here we used two different color wire for two different side, red color wire is attached with the positive side of the coil and black color wire is attached with the negative side of the coil. For the sake of the experiment we connect two of the three top side open boxes in series connection and the other box is kept as before connection. The positive side of the series connection box is connected to the positive side of variac and the negative side is connected to the negative side of the variac. The connection of the other box is done in the same way as the previous two boxes. This arrangement has been made so that the temperature of the main core focused region are varies. With the help of the variac we increase or decrease the voltage for getting the accurate temperature of core focused region. With the help of the multi-meter we fixed the voltage. A digital thermometer is installed in the top side glass window of each three feet long small boxes. The temperature of the main core focused region is optimized for the experiment by increasing or decreasing the voltage with the help of the variac by observing the temperature of the digital temperature. After that we are passing different wavelength laser over this region. Fig.5.2. shows hot chamber.

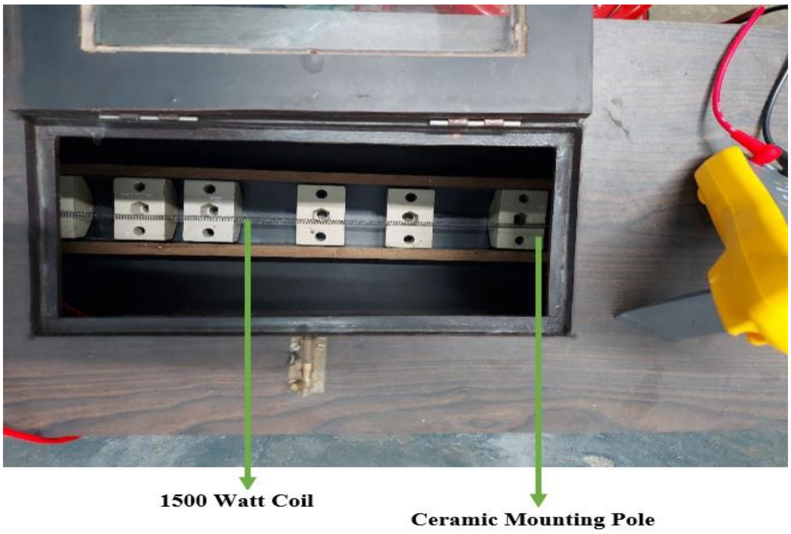

Fig.5.2. Artificial hot chamber arrangement

5.3. Fog

For this experiment six hollow wooden boxes were made. Each of the six boxes is 3 feet in length, 1 feet in width and 1 feet in height. Out of six boxes this design has been made for the four boxes in the middle which are completely open two sides and other three sides out of four sides have one glass window on each side. Remaining one side of the wooden box is completely closed because that side is placed on the wooden bench. Each glass window is 1 feet in length, 0.5 feet in width and 0.25 feet distance from edge to edge of three sides. The other two boxes on the extreme side have the same design, one side of the box is completely open and the exact opposite side has a square shape glass window of which each side has 0.25 feet. When all the boxes are merged, then this window of the two side works as inward and outward way of this wooden box. Each small box is numbered for the convenience of the experiment. Outside of every small box is coated with sunmica and inside of the box is painted with heat-resistant black color to prevent any unexpected incidents during the experiment. Each small box is completely attached as well as aligned to the other box and in order to prevent the movement of the air through the sticking parts, the boxes are fully air sealed by using gas blocking strip. As a result, the outside weather cannot affect during the experiment. For this system setup we will get the results of our experiment with more accuracy. If the small boxes are arranged in a row regarding their serial number, the length of the newly formed box is 18 feet. These 18 feet is the main core focused region of our experiment. Each small box is placed on the wooden bench and each wooden bench is 3 feet long, 1 feet width and 2 feet height from the ground. In order to keep the glass windows, we can compare the weather inside the wooden box with the atmospheric weather for the purpose of experiment.

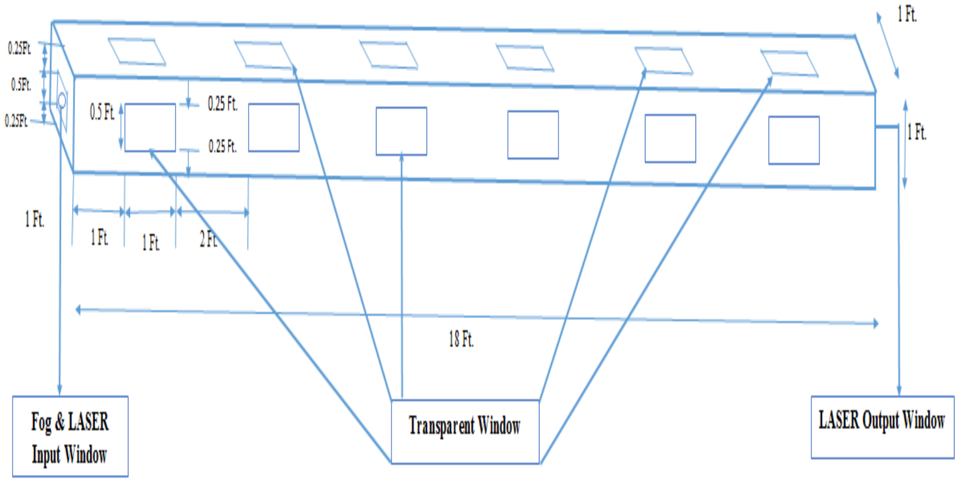

Fig.5.3 Schematic diagram of the fog simulation box/chamber

Fig.5.4. Artificial fog simulation setup with ultrasonic nebulizers

After that three nebulizers are installed on top side of the wooden box. Natural fog is given inside the wooden box through the nebulizers. With the help of the speed controlling button of the nebulizer we determine the amount of fog for the experiment. Different types of fog like thin fog, light fog, moderate fog, light haze, haze, thick fog and dense fog are produced with the help of the speed controlling button of the nebulizer. A nebulizer uses drinking water to produce the fog, so produced fog through water with the help of nebulizer we can say the produced fog is natural fog because particle of the fog made with water. Out of six windows three glass windows at the top of the wooden box are kept open when fogging the box through the nebulizers. We cut a thick paper board to the size of the glass windows from a large paper board so that the fog doesn’t come out from the box. Then the size of the diameter of the nebulizer outing pipe is cut on that thick paper board. We cut three thick paper boards of the same size for three opened windows. As a result of this arrangement, fog cannot come out. Three nebulizers were intended to be used for equal amounts of fog at each location at each region in core focused experimental region. After this we pass different wavelength lasers for experiment through this region. Fig.5.3. shows schematic diagram of artificial fog chamber and fig.5.4. shows artificial arrangement for fog simulation.

Fig.5.5. Natural fog (Type I) inside the wooden box

Fig.5.5., fig.5.6., fig.5.7., fig.5.8., fig.5.9. and fig.5.10. show the different types of natural fog like thin fog, light fog, moderate fog, light haze, haze, thick fog and dense fog which used in our experiment.

Fig.5.6. Natural fog (Type II) inside the wooden box

Fig.5.7. Natural fog (Type III) inside the wooden box

Fig.5.8. Natural fog (Type IV) inside the wooden box

Fig.5.9. Natural fog (Type V) inside the wooden box

Fig.5.10. Natural fog (Type VI) inside the wooden box

5.4. Rain

We put this equipment on the roof of the Electrical Engineering department, thus the entire experiment is conducted outside, exposed to the sky. This was done primarily in order to obtain more realistic data and to advance in the collection of data under real atmospheric conditions, as the entire experiment is dependent on the collection of attenuation. The likelihood of attenuation is substantially higher when it is done outside, demonstrating that the data obtained from this procedure is more accurate. The construction is composed of 6mm diameter pure iron rods and is shaped like a rectangular hollow box with a length of 18 feet, a width of 3 feet, and a height of 10 feet. Three 18 feet long PVC pipes are installed to the rod at the top of the iron structure. For the experimental purpose each pipe is drilled with the help of the drill machine. Each pipe has a different diameter of the holes made by the drill machine. As a result, different types of rain rates can be obtained through this arrangement. Iron rods are fixed at the height of 3 feet and 6 feet from the ground of the structure. There are gardening nozzles installed at a distance of 1 feet and each nozzle provides water from two directions. The PVC pipelines and nozzle pipelines are well fixed with iron structure with the help of cable tie. Each pipe is connected to the UPVC pipe and UPVC pipe is connected to the pipe coming from the tank through 8 ball valve. Since the water tank at the pipe's end has the dimensions 2.4x2.4x1.2 feet and can hold around 250 liters of water, it is submerged in the water as it is. Additionally, a further pipe section that has been placed in the secondary pipe line's outflow portion and is politely referred to as "extra pipe" is connected into the water tank. Aside from preventing water wasting, the extra pipe's installation has the dual aim of monitoring pipe pressure and preventing leaks. The water tank is filled with the aid of a 5 foot long water pipe, and the outlet of the water tank is linked to a 0.5 HP (horsepower) pump with the aid of a 1 inch flexible pipe, with the pump then being connected to the entrance of the secondary water pipe line of the iron structure system. The distance between the transmitter and the receiver is 40 feet approximately, the link is established through the iron structure. The transmitter and receiver are placed 11 feet from the artificial rain setup, so as to primary protect the laser and its module and other instruments which are used in this experiment.

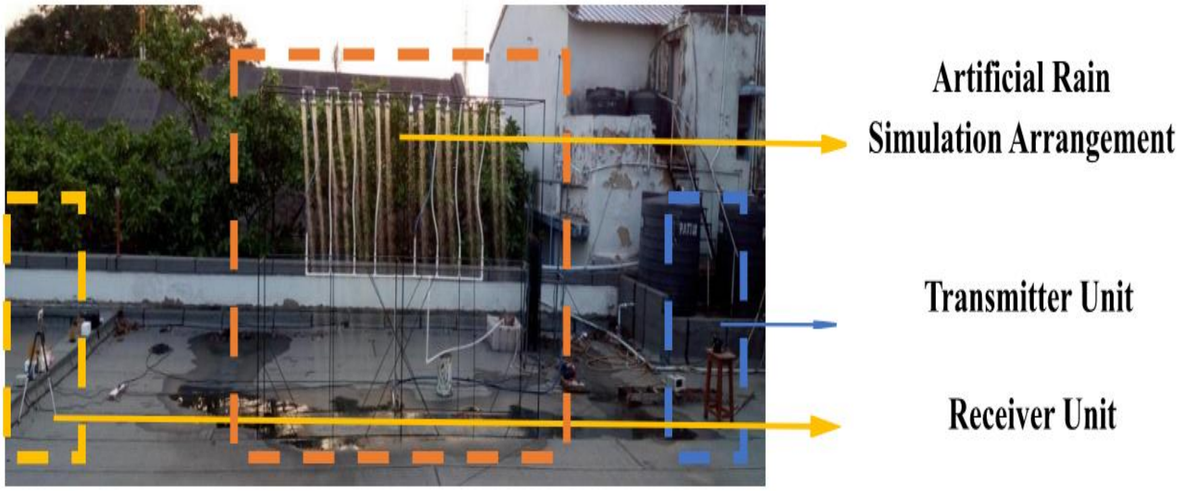

Fig.5.11. Artificial rain simulation arrangement

Fig.5.11. shows the artificial rain simulation arrangement. Fig.5.12. depicts an experiment that is being conducted at night while using a rain simulation setup, and Fig.5.13. depicts an experiment that is being conducted at night while using the same arrangement, but the rain rate in the two photographs is different.

Fig.5.12. Experimentation is going on at night time(Type I)

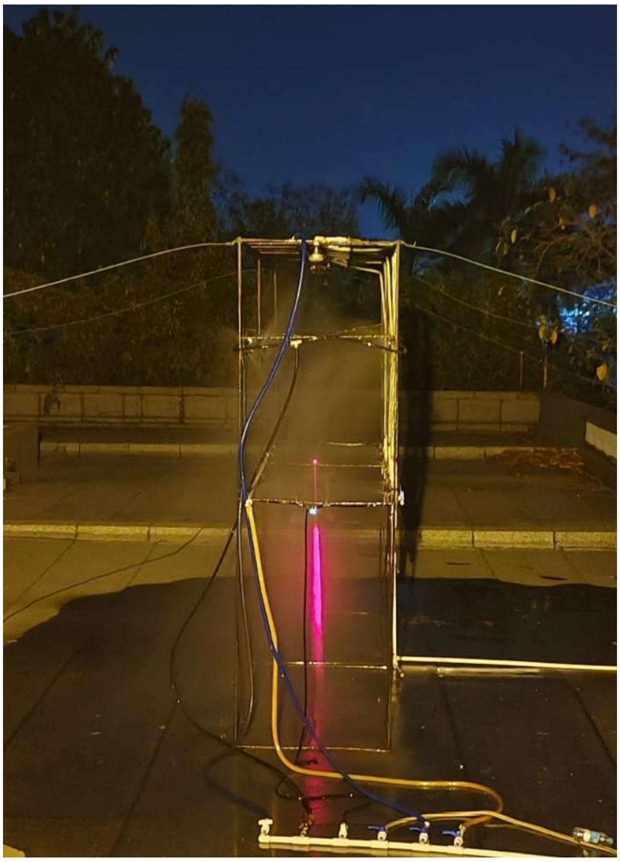

Fig.5.13. Experimentation is going on at night time (Type II)

The appropriate rain gauge, which is shown in Fig.5.14., has been used to measure the rate of precipitation.

Fig.5.14. Rain rate measured by the suitable rain gauge

Chapter 6 – Experimental Results

Experimental result has divided into two parts. Number one is optical power attenuation and another one is channel attenuation.

6.1. Optical Power Attenuation

6.1.1. Fog Experiment

The optical has been measured using suitable optical power meter whose range is 380nm to 10600nm (Model No. 7Z01560). From the Fig.6.1. Optical Power Attenuation of 532nm LASER Source it has been shown that the received optical power has been changed with respect to different visibility and this visibility has been created by the nebulizer which similar to the natural fog. As the visibility has been changed with respect to different time, as a result, the received optical power has been changed with respect to time. When the visibility is more, the optical power attenuation is more and vise-versa. The visibility has been determine from the Kim model and these values are collected from the fig.6.1. Optical Power Attenuation of 532nm LASER Source, due to lack of visibility meter and finally the time versus visibility curve has been determine by these curve and Kim model. Similar process done for the 650nm laser also.

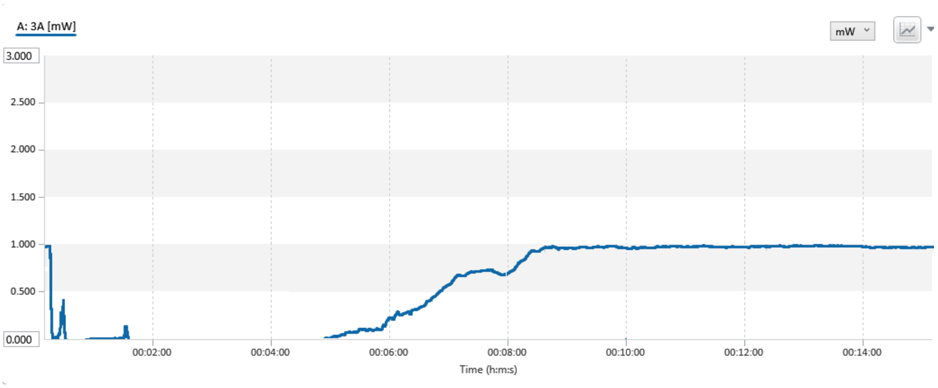

Fig.6.1. Optical Power Attenuation of 532nm LASER Source

From these two curve Fig.6.1. Optical Power Attenuation of 532nm LASER Source and Fig.6.2. Optical Power Attenuation of 650nm LASER Source, it has been shown that the 532nm laser is more attenuated than 650nm laser. Finally the optical power attenuation due to fog for the both wavelength (532nm and 650nm) has been given fig.6.3. Received optical power at different Visibility conditions (532 nm, 650 nm).

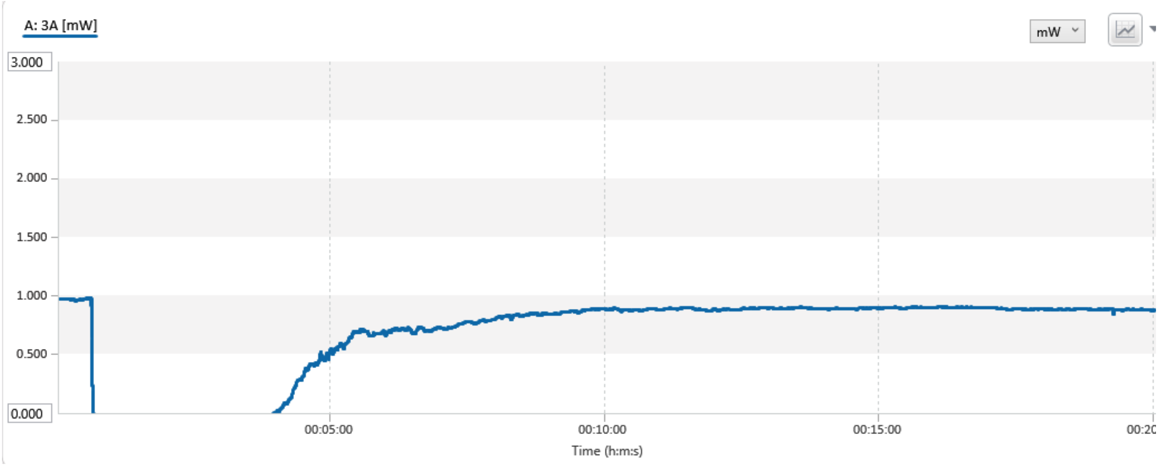

Fig.6.2. Optical Power Attenuation of 650nm LASER Source

The received optical power has been demonstrated in fig.6.3. Received optical power at different Visibility conditions (532 nm, 650 nm) to have been altered in relation to various levels of visibility, which were produced by a nebulizer that resembled a natural fog. The received optical power has varied with regard to time as a result of the changing visibility with respect to different times. Visibility affects optical power attenuation in the opposite direction of visibility. The Kim model was used to calculate the visibility, and these values were taken from the fig.6.3. Received optical power at different Visibility conditions (532 nm, 650 nm), owing to the absence of a visibility meter, and lastly, these curves plus the Kim model have determined the time vs visibility curve. The 650nm laser has likewise undergone a similar procedure.

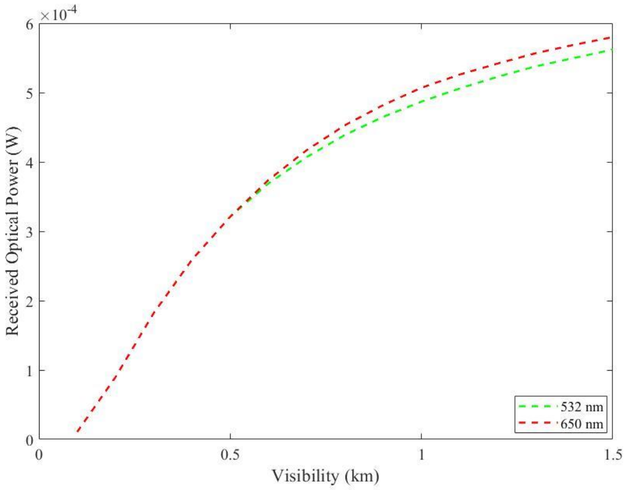

Fig.6.3. Received optical power at different Visibility conditions (532 nm, 650 nm)

From the fig.6.4. Optical Power Attenuation of 808nm LASER Source it has been shown that the received optical power has been changed with respect to different visibility and this visibility has been created by the nebulizer which similar to the natural fog. As the visibility has been changed with respect to different time, as a result, the received optical power has been changed with respect to time. When the visibility is more, the optical power attenuation is more and vise-versa. The visibility has been determine from the Kim model and these values are collected from the fig.6.4. Optical Power Attenuation of 808nm LASER Source, due to lack of visibility meter and finally the time versus visibility curve has been determine by these curve and Kim model. Similar process done for the 980nm laser also.

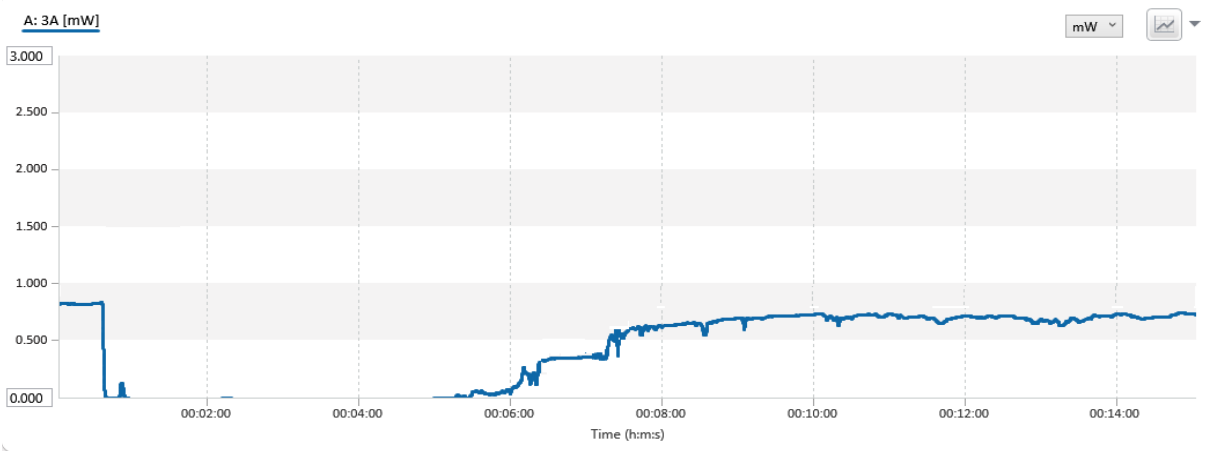

Fig.6.4. Optical Power Attenuation of 808nm LASER Source

From these two curve Fig.6.4. Optical Power Attenuation of 808nm LASER Source and Fig.6.5. Optical Power Attenuation of 980nm LASER Source, it has been shown that the 808nm laser is more attenuated than 980nm laser. Finally the optical power attenuation due to fog for the both wavelength (808nm and 980nm) has been given fig.6.6.

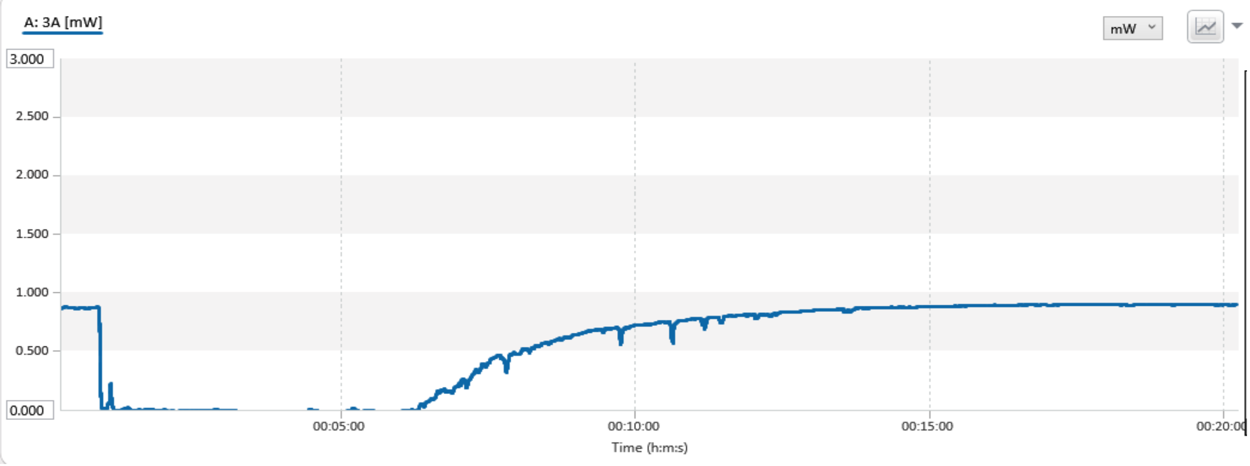

Fig.6.5. Optical Power Attenuation of 980nm LASER Source

It can be seen that the 808nm laser is more attenuated than the 980nm laser from these two curves fig.6.4., fig.6.5. Finally, a fig.6.6. illustrating the optical power attenuation owing to fog for both wavelengths (808 nm and 980 nm) has been provided.

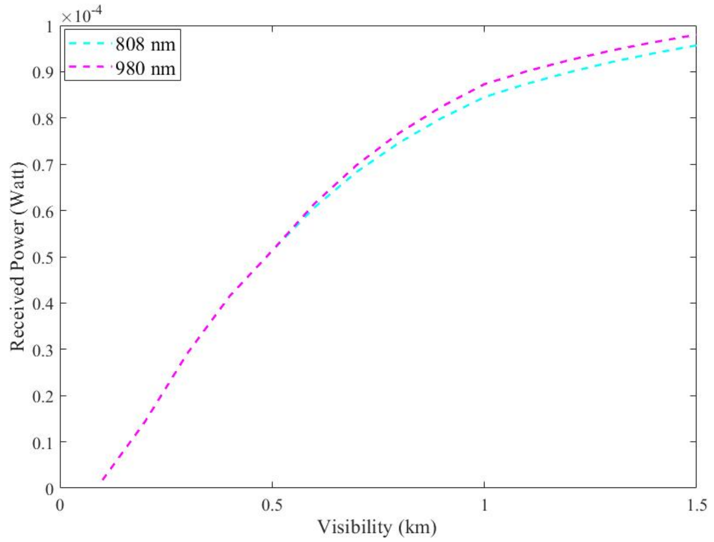

Fig.6.6. Received Optical Power Vs Visibility

6.1.2. Temperature Experiment

The optical power attenuation due to lower scintillation has been given in fig.6.7. Almost 0.16 dB loss has been occurred during this range of scintillation.

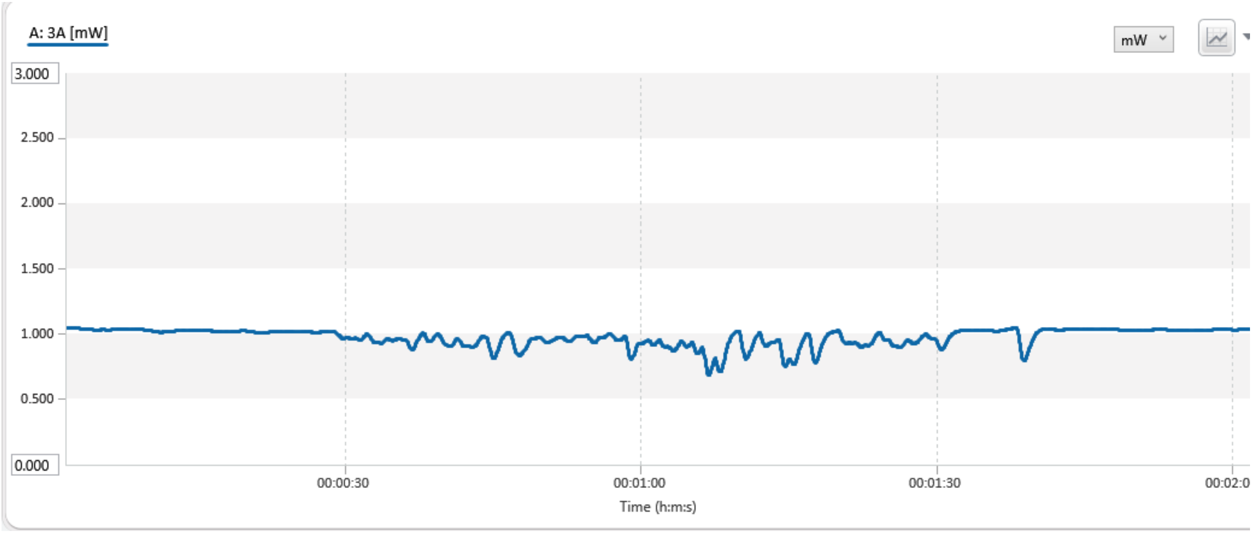

Fig.6.7. Optical Power Attenuation of 532nm laser during the scintillation of 10^{-15}

Similarly, for 10^{-14} scintillation range, the optical power attenuation almost 0.5 dB has been noticed that has been shown in fig.6.8.

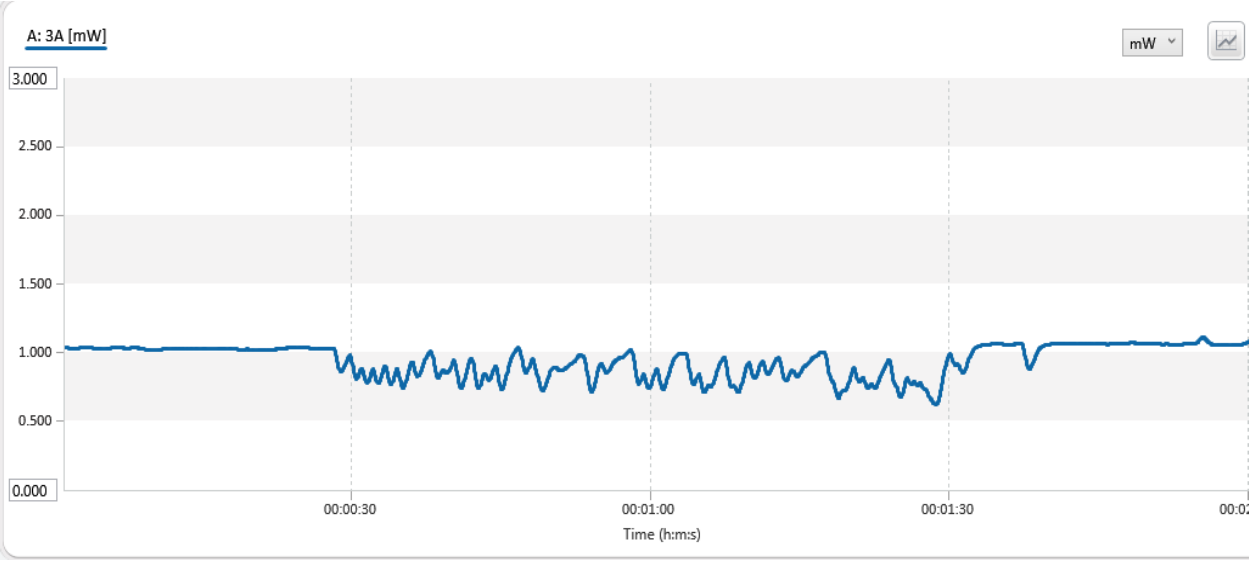

Fig.6.8. Optical Power Attenuation of 532nm laser during the scintillation of 10^{-14}

The optical power attenuation for the scintillation range of 10^{-13} has been shown in fig.6.9. From this figure it has been shown that almost 1.53 dB loss has been occurred.

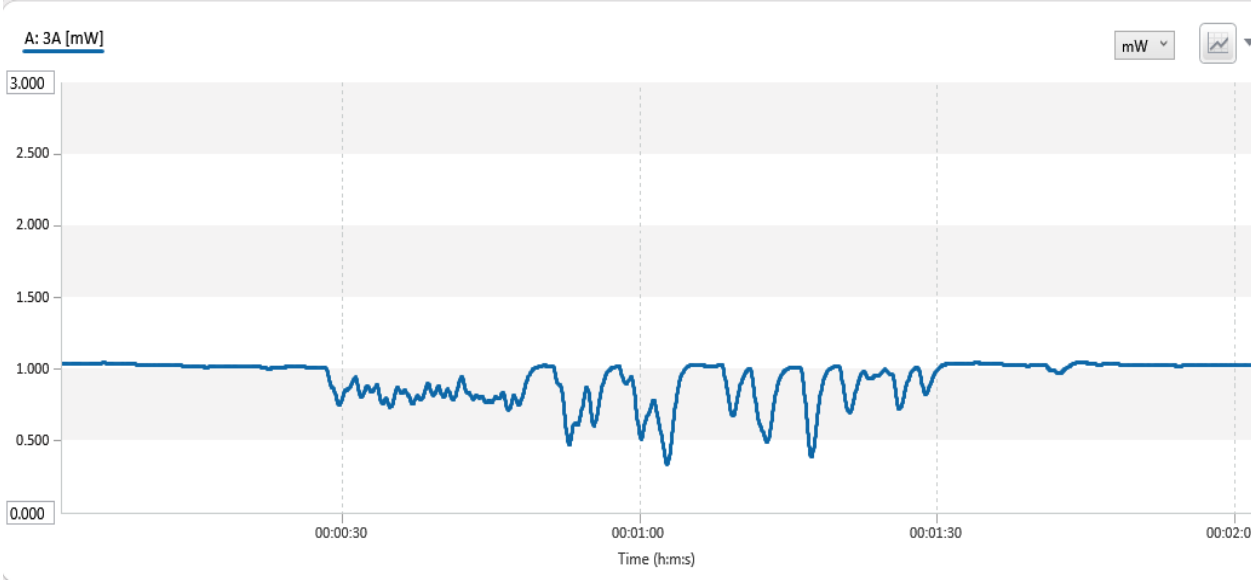

Fig.6.9. Optical Power Attenuation of 532nm laser during the scintillation of 10^{-13}

Finally, the attenuation for the higher turbulence regime like $5x10^{-12}$ range, the optical power has been noticed almost 10.84 dB.

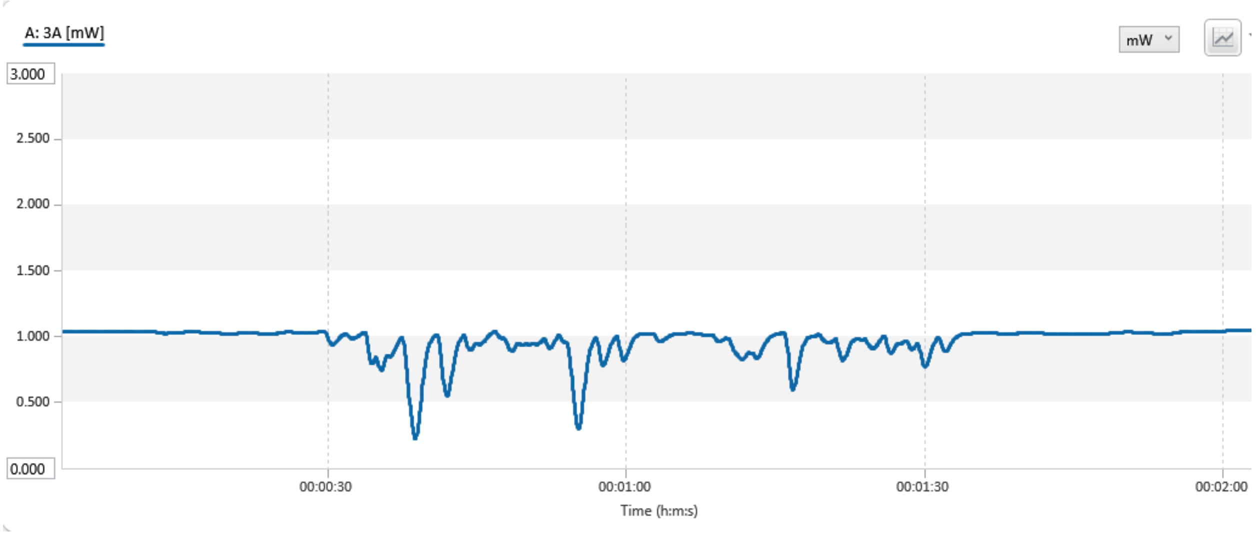

Fig.6.10. Optical Power Attenuation of 532nm laser during the scintillation of 10^{-12}

For the 650nm wavelength laser, the optical power attenuation due to lower scintillation has been given in fig6.11. Almost 0.14 dB loss has been occurred during this range of scintillation.

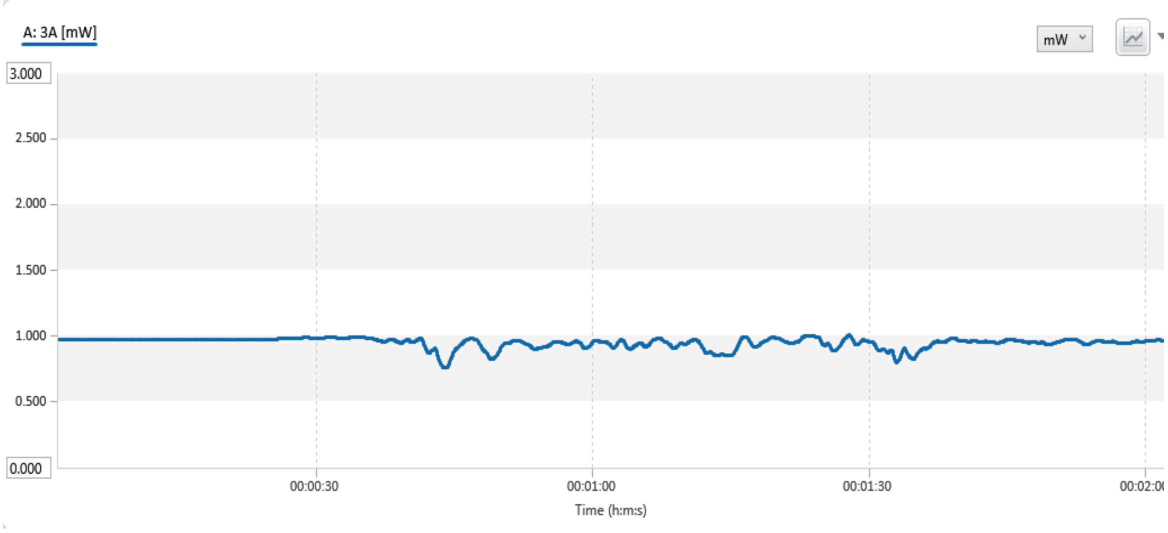

Fig.6.11. Optical Power Attenuation of 650nm laser during the scintillation of 10^{-15}

Similarly, for 10^{-14} scintillation range, the optical power attenuation almost 0.44 dB has been noticed that has been shown in fig.6.12.

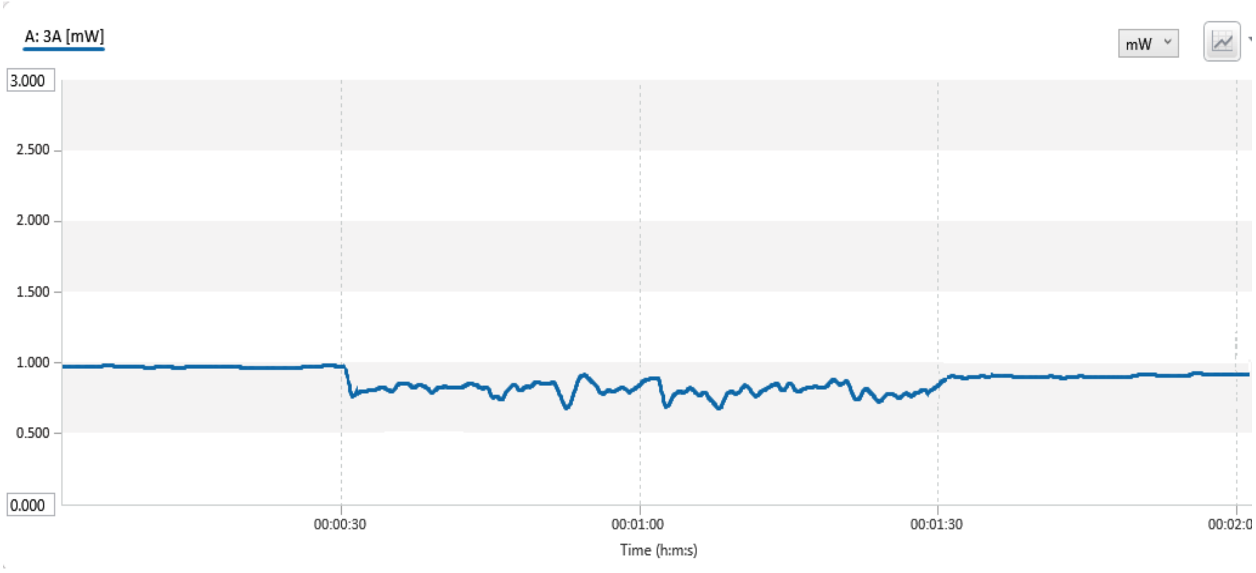

Fig.6.12. Optical Power Attenuation of 650nm laser during the scintillation of 10^{-14}

The optical power attenuation for the scintillation range of 10^{-13} has been shown in fig.6.13. From this figure it has been shown that almost 1.4 dB loss has been occurred.

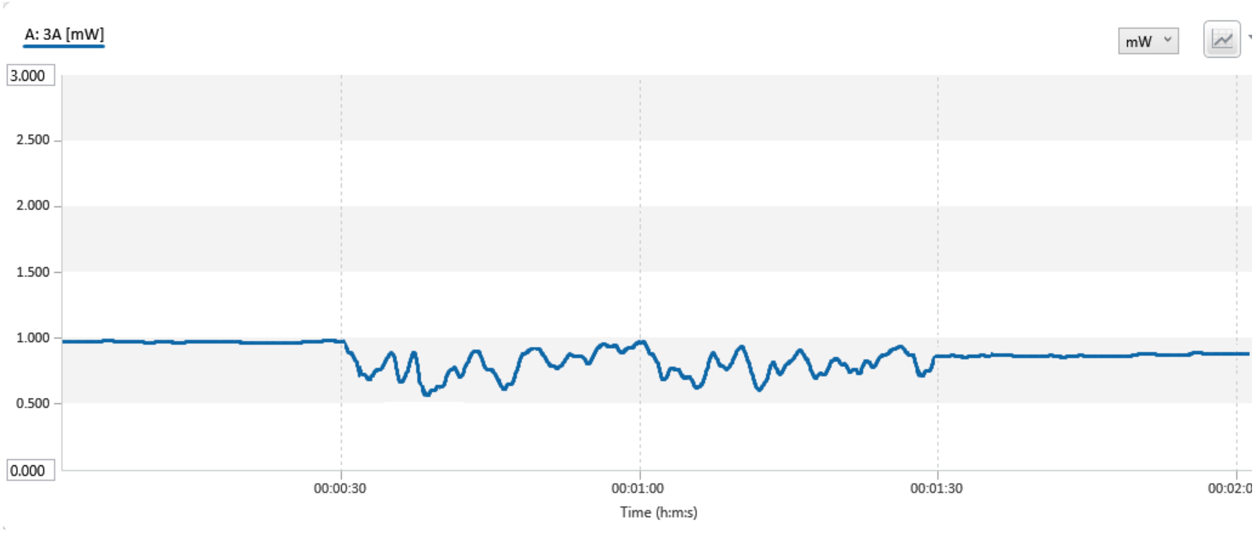

Fig.6.13. Optical Power Attenuation of 650nm laser during the scintillation of 10^{-13}

Finally, the attenuation for the higher turbulence regime like $5x10^{-12}$ range, the optical power has been noticed almost 9.81 dB.

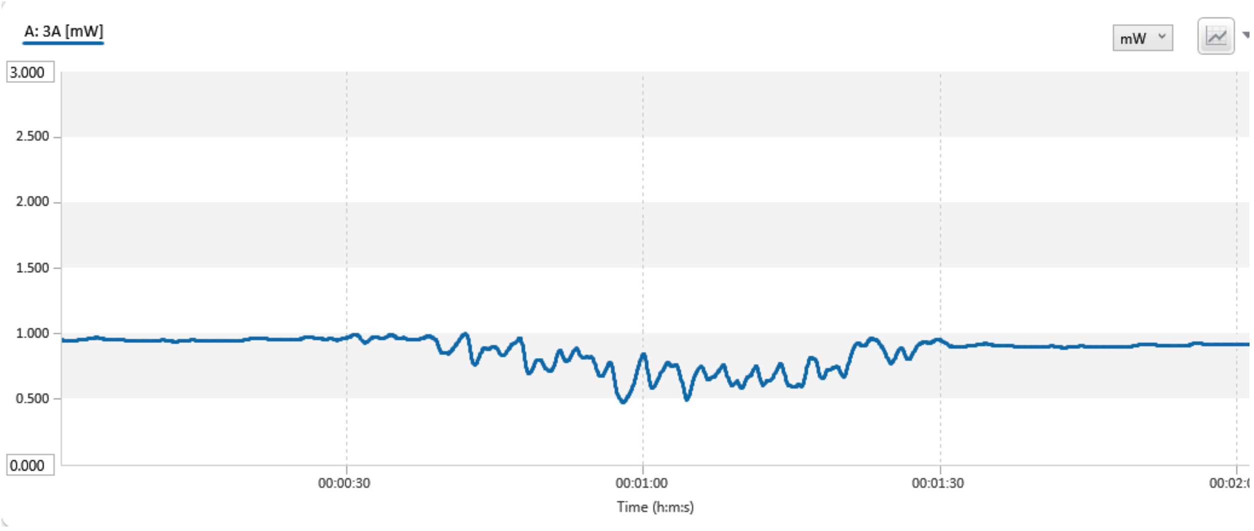

Fig.6.14. Optical Power Attenuation of 650nm laser during the scintillation of $5x10^{-12}$

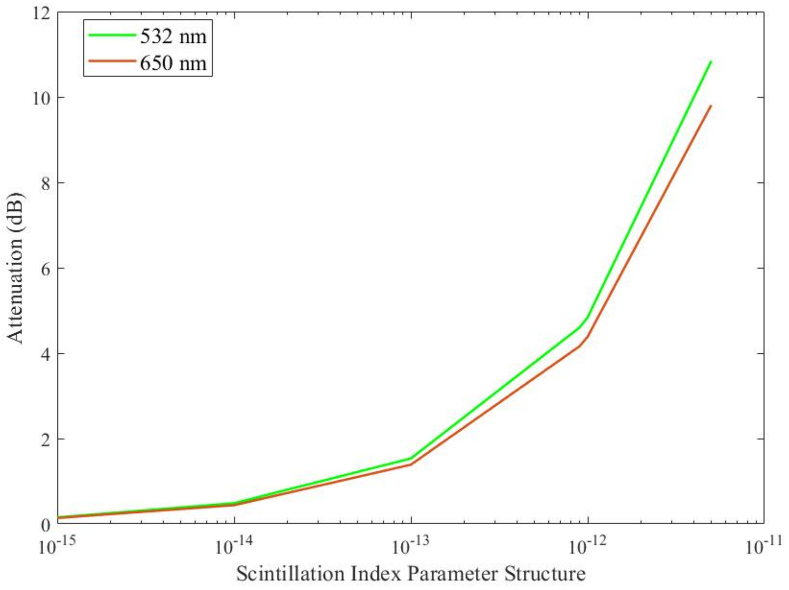

Fig.6.15. Optical power attenuation for different scintillation index parameter structure (532 nm, 650 nm)

From the above fig.6.15., it has been shown that the same scintillation regime, the 532 nm Laser is more attenuated than 650 nm Laser.

For the 808nm wavelength laser, the optical power attenuation due to lower scintillation (range of 10^{-15}) has been given in fig.6.16. Almost 0.13 dB loss has been occurred during this range of scintillation.

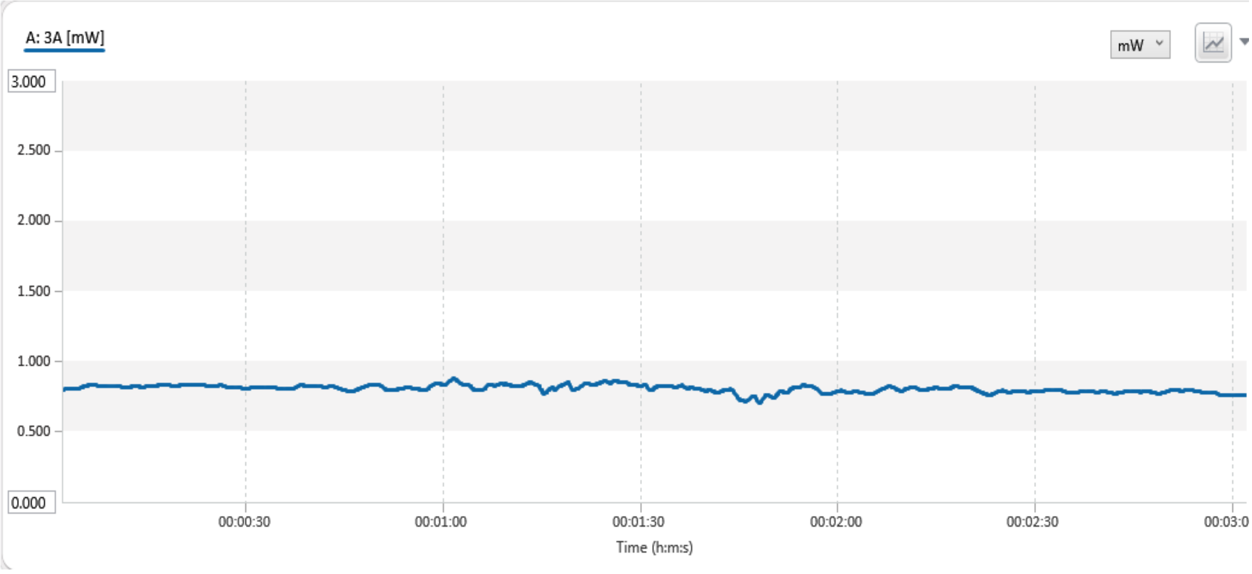

Fig.6.16. Optical Power Attenuation of 808nm laser during the scintillation of 10^{-15}

The optical power attenuation for the scintillation range of 10^{-14} has been shown in fig.6.17. From this figure it has been clearly observed that almost 0.41 dB loss has been occurred.

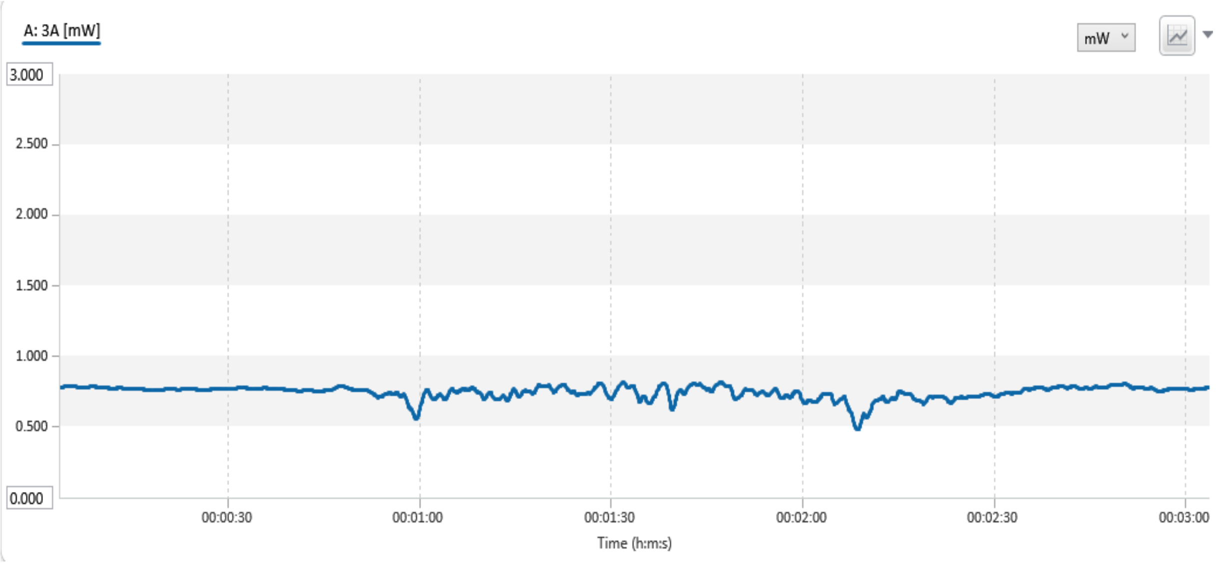

Fig.6.17. Optical Power Attenuation of 808nm laser during the scintillation of 10^{-14}

The optical power attenuation for the scintillation range of 10^{-13} has been shown in fig.6.18. From this figure it has been clearly observed that almost 1.244 dB loss has been occurred.

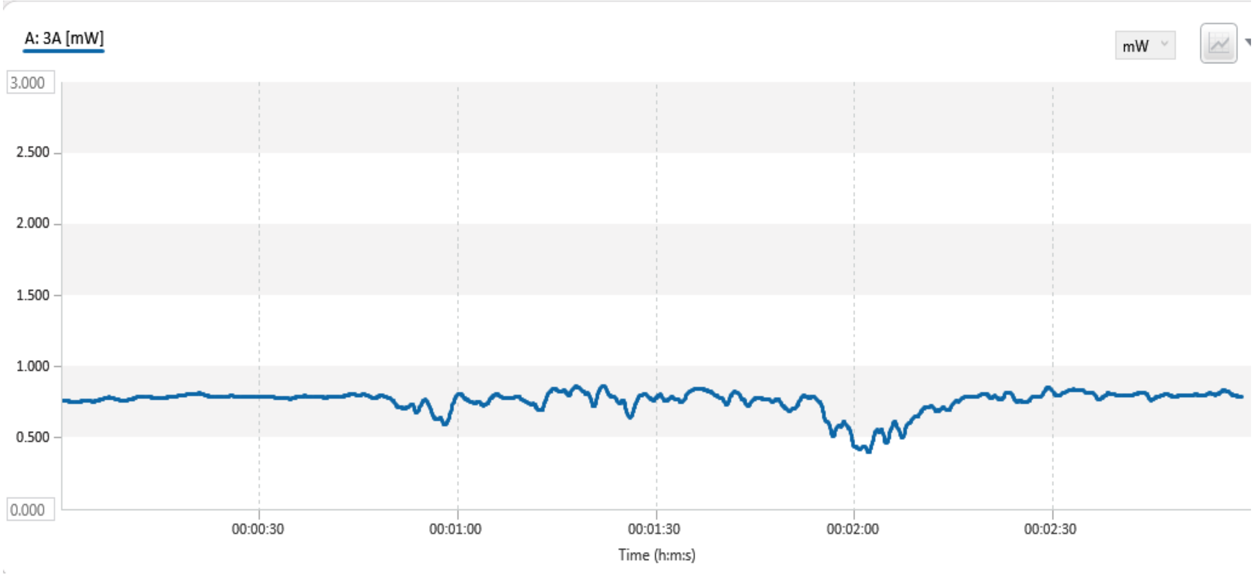

Fig.6.18. Optical Power Attenuation of 808nm laser during the scintillation of 10^{-13}

Finally, the attenuation for the higher turbulence regime like $5x10^{-12}$ range, the optical power has been noticed almost 8.8 dB. It has been shown in fig.6.19.

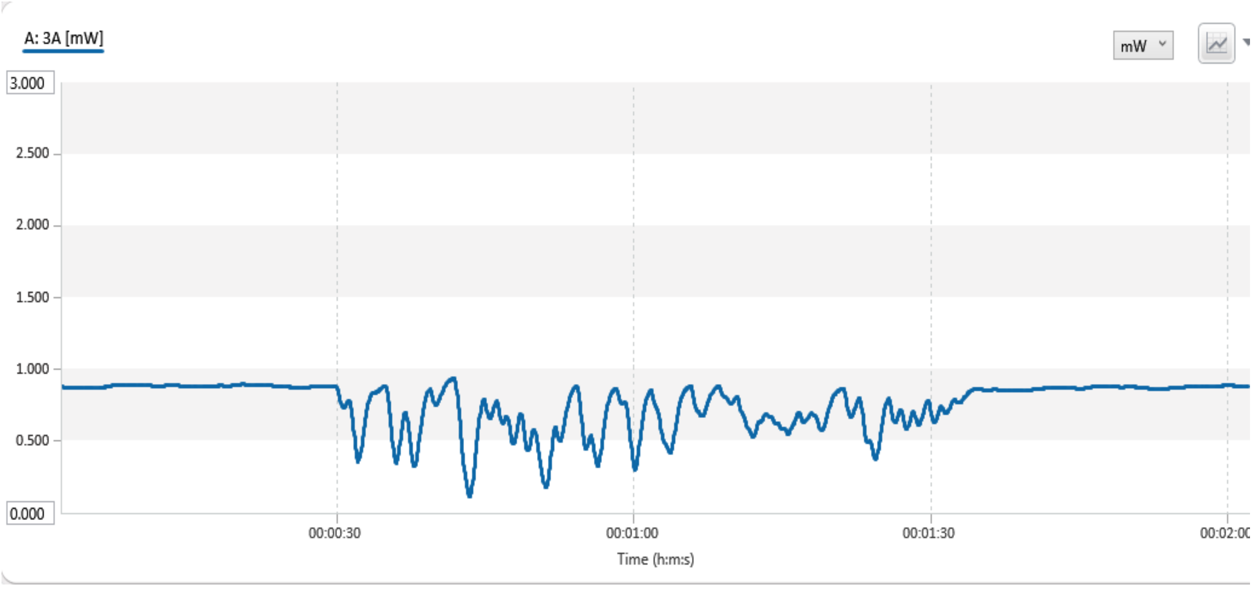

Fig.6.19. Optical Power Attenuation of 808nm laser during the scintillation of 10^{-12}

For the 980nm wavelength laser, the optical power attenuation due to lower scintillation (range of 10^{-15}) has been given in fig.6.20. Almost 0.112 dB loss has been occurred during this range of scintillation.

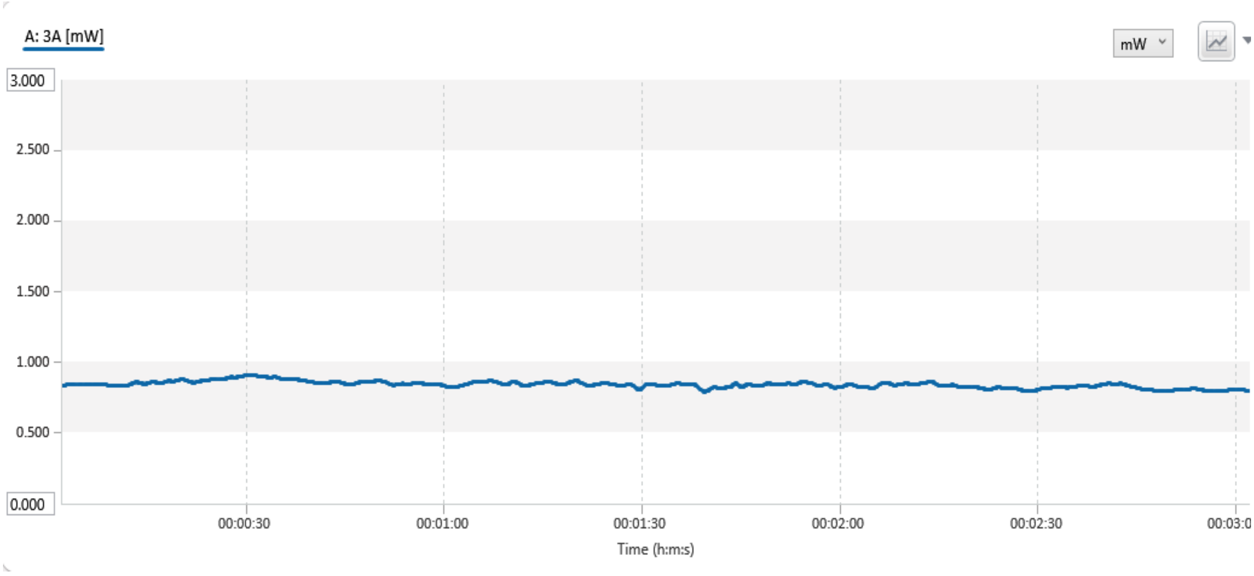

Fig.6.20. Optical Power Attenuation of 980nm laser during the scintillation of 10^{-15}

The optical power attenuation for the scintillation range of 10^{-14} has been shown in fig.6.21. From this figure it has been clearly observed that almost 0.36 dB loss has been occurred.

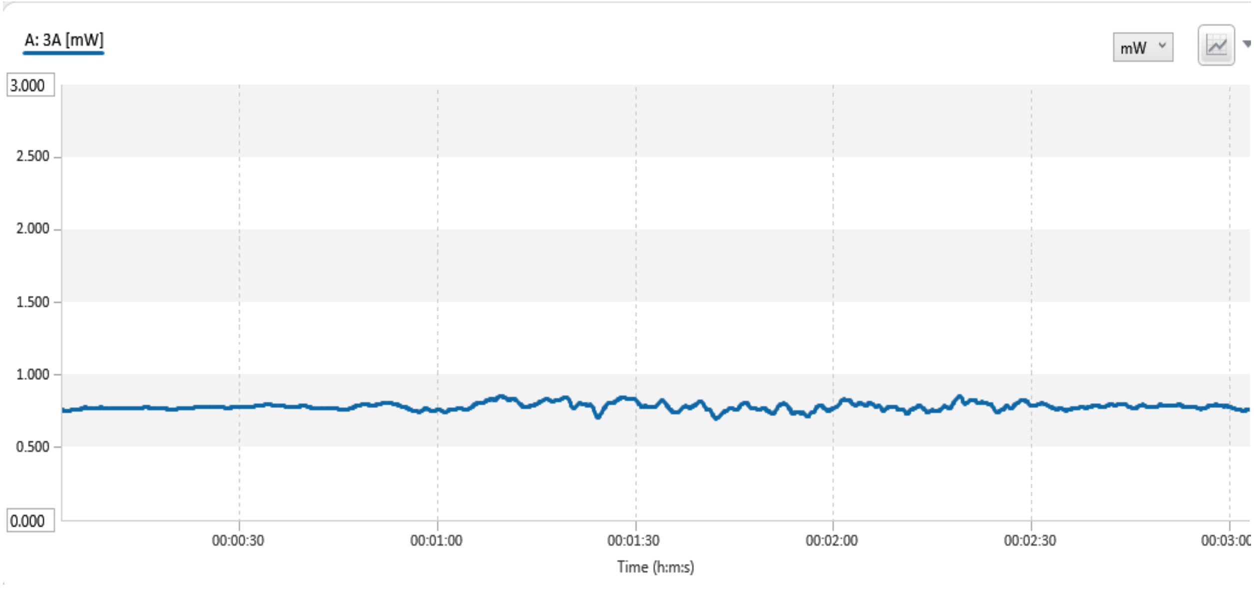

Fig.6.21. Optical Power Attenuation of 980nm laser during the scintillation of 10^{-14}

The optical power attenuation for the scintillation range of 10^{-13} has been shown in fig.6.22. From this figure it has been clearly observed that almost 1.118 dB loss has been occurred.

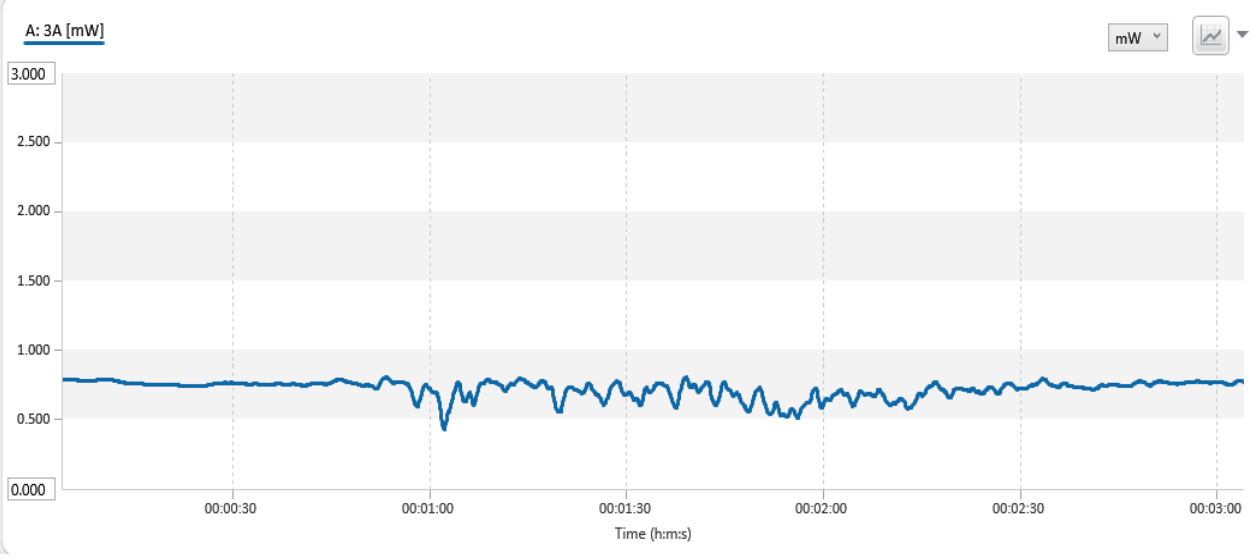

Fig.6.22. Optical Power Attenuation of 980nm laser during the scintillation of 10^{-13}

Finally, the attenuation for the higher turbulence regime like 5×10^{-12} range, the optical power has been noticed almost 8.05 dB. It has been shown in fig.6.23.

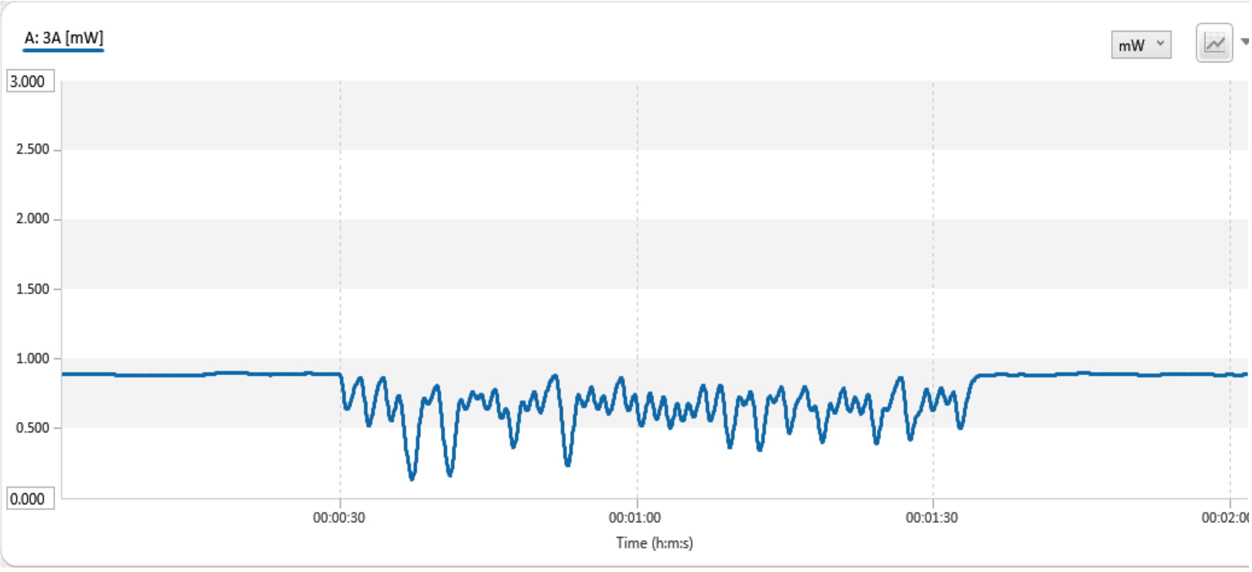

Fig.6.23. Optical Power Attenuation of 980nm laser during the scintillation of 10^{-12}

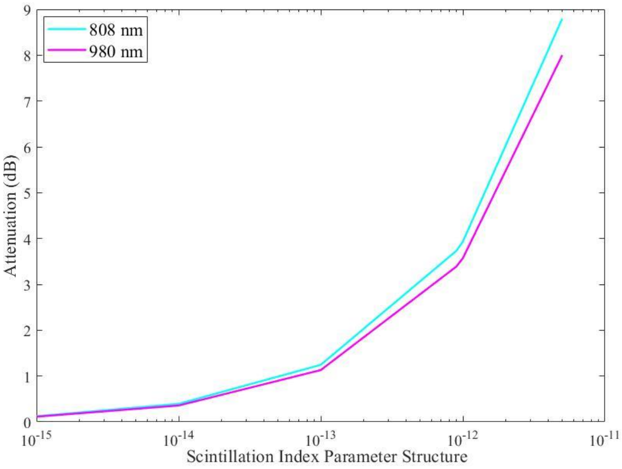

Fig.6.24. Optical power attenuation for different scintillation index parameter structure (808 nm, 980 nm)

From the above-mentioned fig.6.24., it has been shown that 808 nm is more attenuated than 980 nm Laser source for the same scintillation index parameter regime.

6.1.3. Rain Experiment

Different optical power attenuation has been noticed for different rain rates. As the rain rates is increased, the optical power attenuation is increased gradually. It has been observed that the attenuation due to rain is for the both wavelength (532 nm & 650 nm) is almost same as the rain droplet size is greater than the optical wavelengths. The optical power attenuation for the 5 mm/hr rain rate has been shown in fig.6.25. From this figure it has been clearly observed that almost 0.128 dB loss has been occurred.

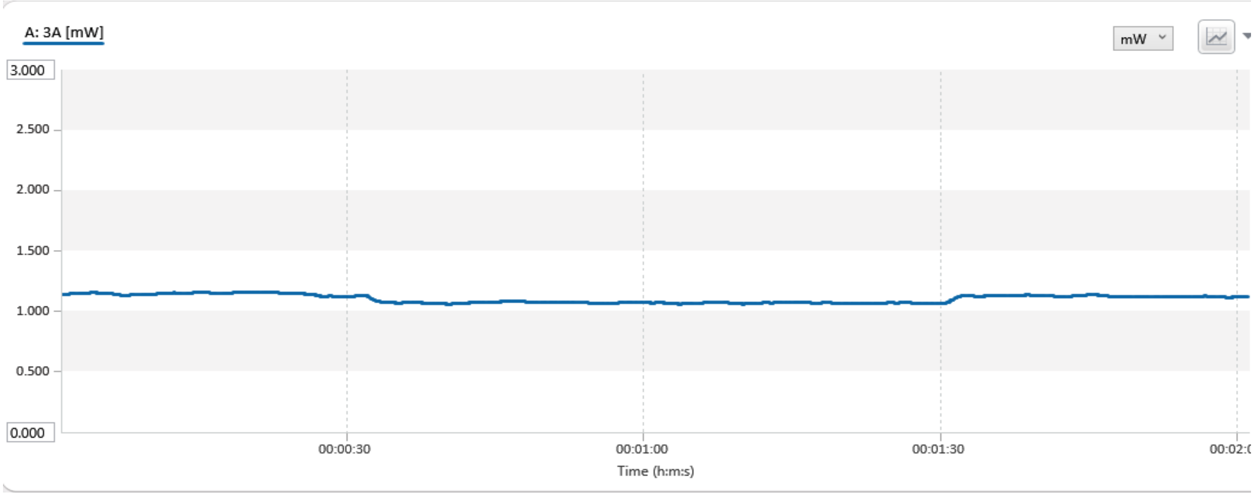

Fig6.25. Optical Power Attenuation of 532nm & 650nm laser at a rain rate of 5 mm/hr

The optical power attenuation for the 34 mm/hr rain rate has been shown in fig.6.26. From this figure it has been clearly observed that almost 0.405 dB loss has been occurred.

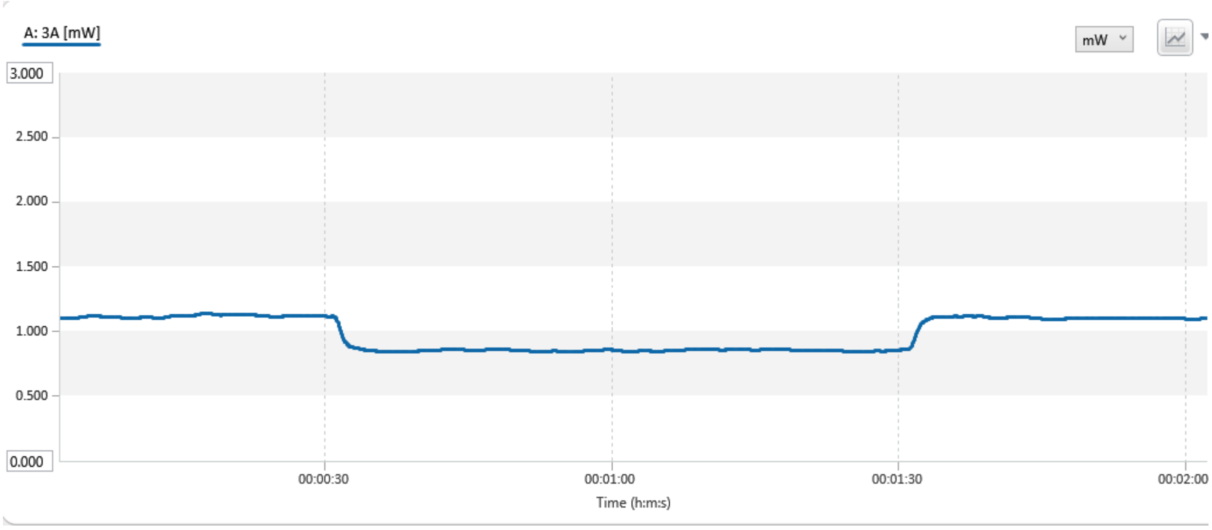

Fig.6.26. Optical Power Attenuation of 532nm & 650nm laser at a rain rate of 34 mm/hr

The optical power attenuation for the 68 mm/hr rain rate has been shown in fig.6.27. From this figure it has been clearly observed that almost 0.553 dB loss has been occurred.

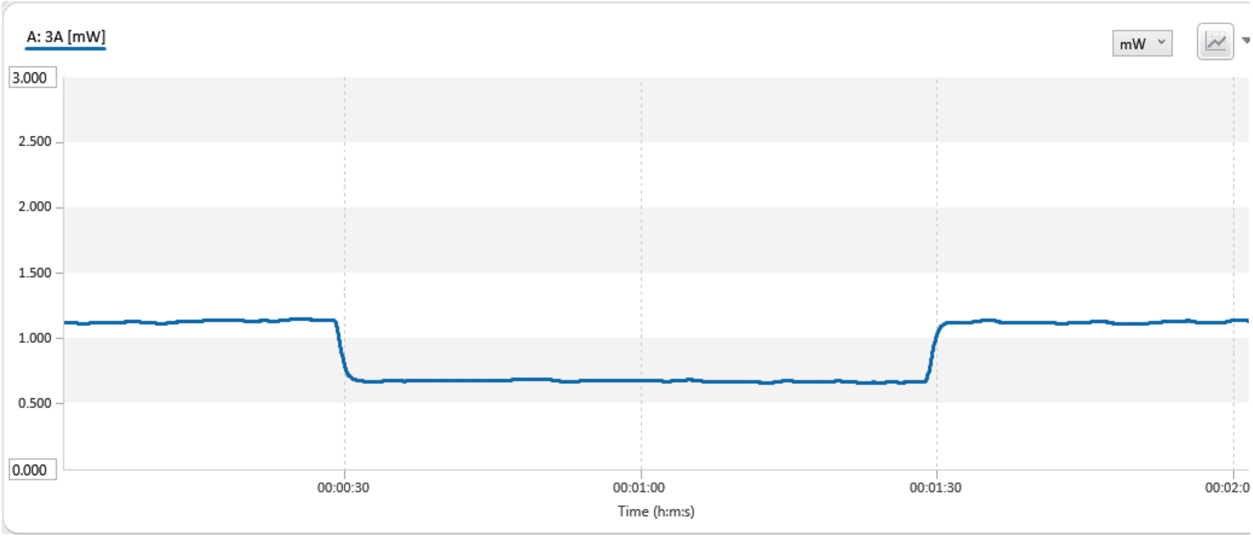

Fig.6.27. Optical Power Attenuation of 532nm & 650nm laser at a rain rate of 68 mm/hr

The optical power attenuation for the 92 mm/hr rain rate has been shown in fig.6.28. From this figure it has been clearly observed that almost 0.79 dB loss has been occurred.

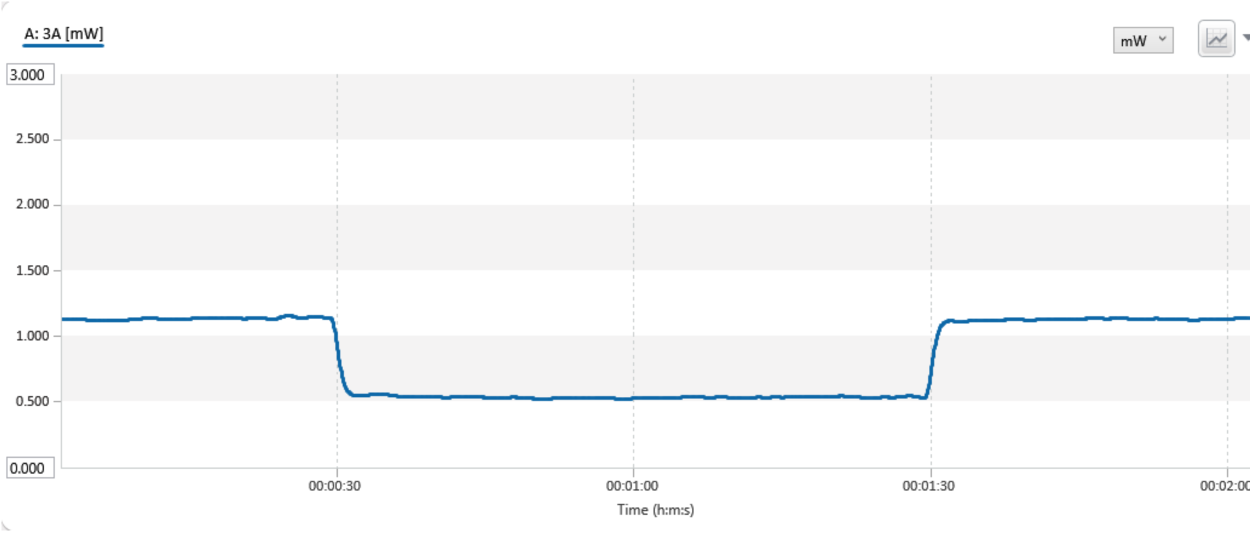

Fig.6.28. Optical Power Attenuation of 532nm & 650nm laser at a rain rate of 92 mm/hr

The optical power attenuation for the 125 mm/hr rain rate has been shown in fig.6.29. From this figure it has been clearly observed that almost 0.959 dB loss has been occurred.

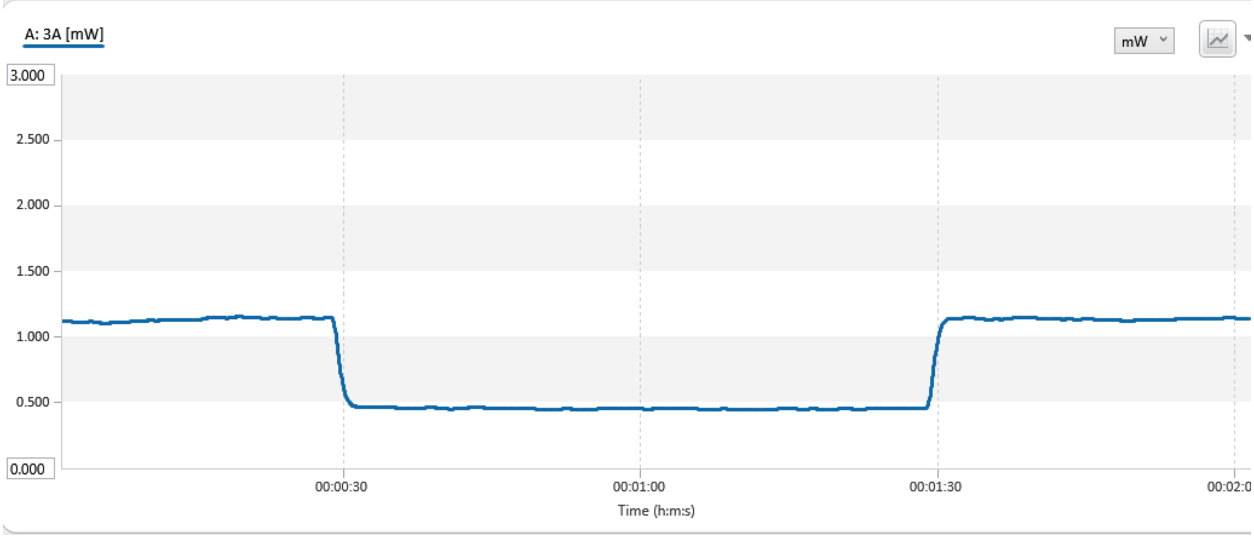

Fig.6.29. Optical Power Attenuation of 532nm & 650nm laser at a rain rate of 125 mm/hr

The optical power attenuation for different rain rates (mm/hr) are shown in fig.6.30. From the figure, it has been shown that both the wavelengths (532 nm, 650 nm) are attenuated in the different rain rates are almost same.

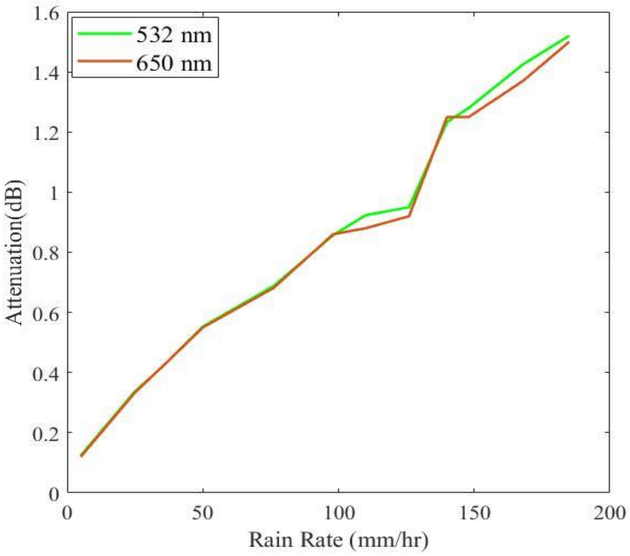

Fig.6.30. Optical Power attenuation at different rain rates (mm/hr) for 532 nm & 650 nm

From the above-mentioned fig.6.30., it has been shown that the optical power attenuation is almost same for the both wavelengths at different rain rates.

Different optical power attenuation has been noticed for different rain rates. As the rain rates is increased, the optical power attenuation is increased gradually. It has been observed that the attenuation due to rain is for the both wavelength (808 nm & 980 nm) is almost same as the rain droplet size is greater than the optical wavelengths.

The optical power attenuation for the 5 mm/hr rain rate has been shown in fig.6.31. From this figure it has been clearly observed that almost 0.122 dB loss has been occurred.

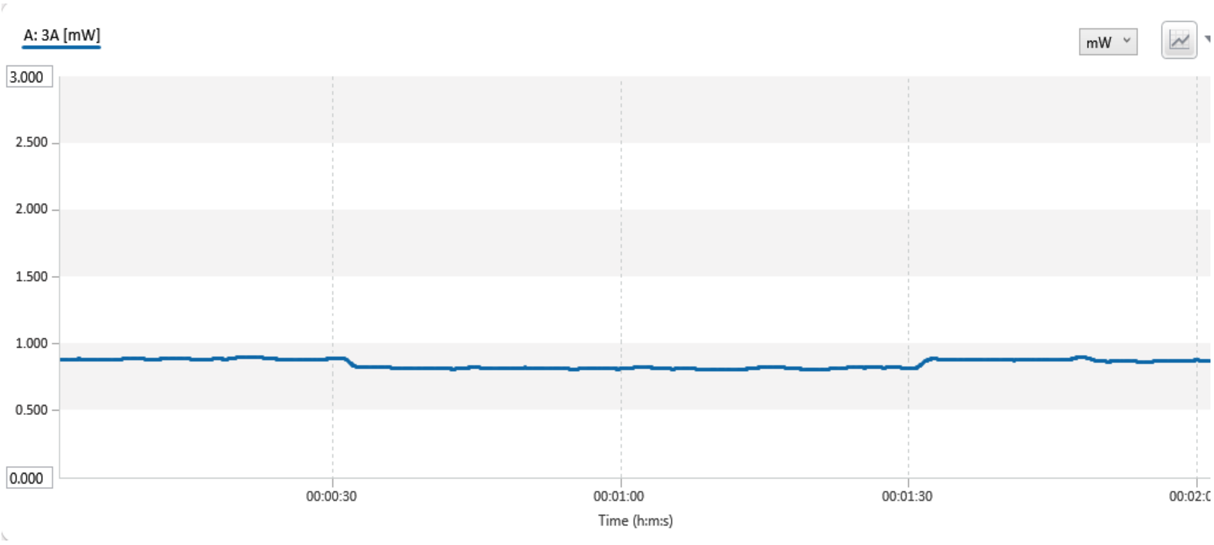

Fig.6.31. Optical Power Attenuation of 808nm & 980nm laser at a rain rate of 5 mm/hr

The optical power attenuation for the 34 mm/hr rain rate has been shown in fig.6.32. From this figure it has been clearly observed that almost 0.397 dB loss has been occurred.

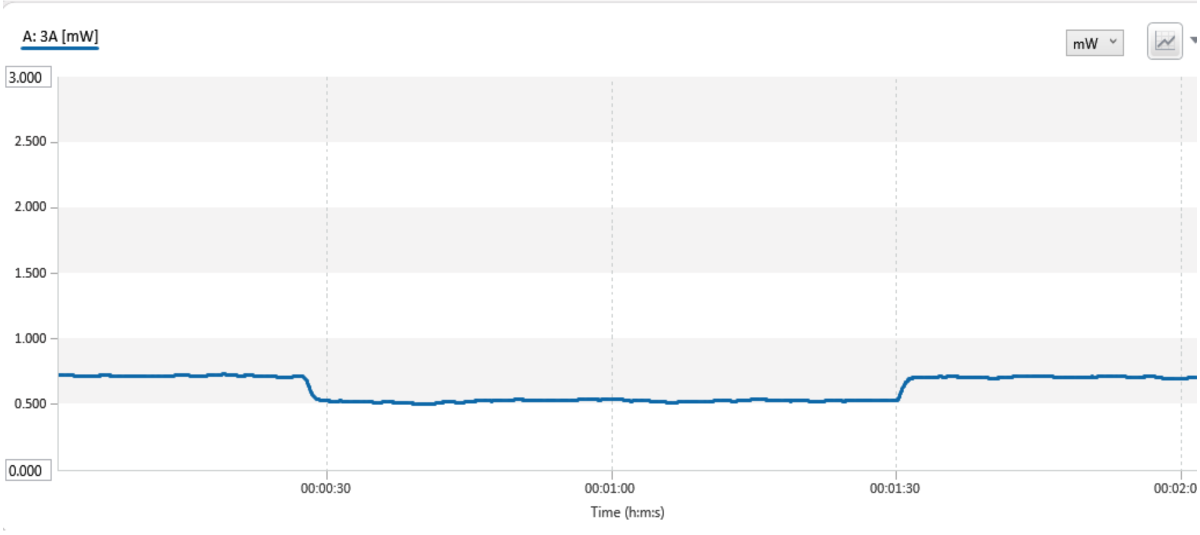

Fig.6.32. Optical Power Attenuation of 808nm & 980nm laser at a rain rate of 34 mm/hr

The optical power attenuation for the 68 mm/hr rain rate has been shown in fig.6.33. From this figure it has been clearly observed that almost 0.548 dB loss has been occurred.

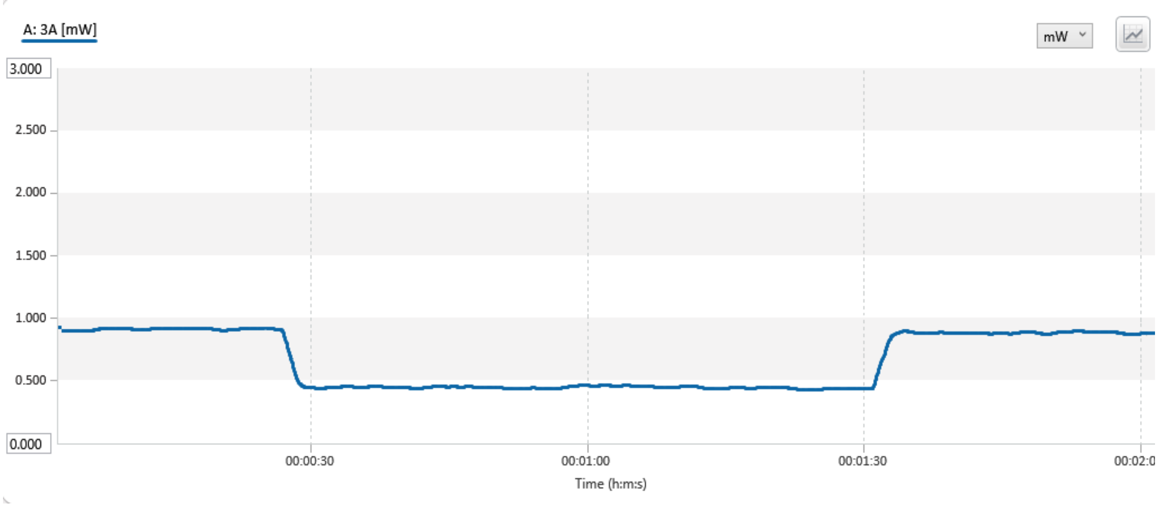

Fig.6.33. Optical Power Attenuation of 808nm & 980nm laser at a rain rate of 68 mm/hr

The optical power attenuation for the 92 mm/hr rain rate has been shown in fig.6.34. From this figure it has been clearly observed that almost 0.77 dB loss has been occurred.

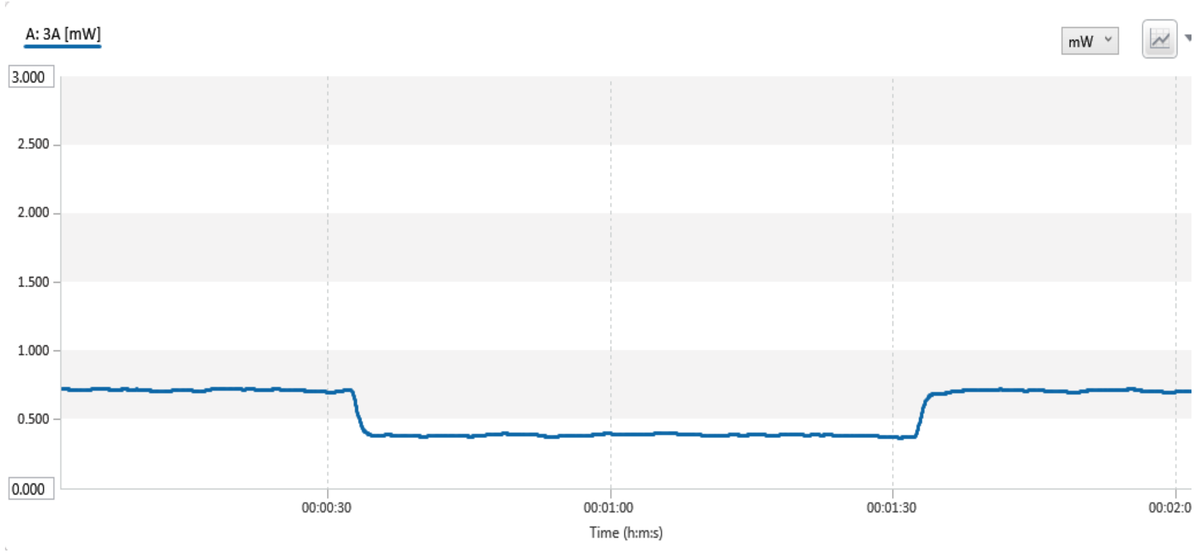

Fig.6.34. Optical Power Attenuation of 808nm & 980nm laser at a rain rate of 92 mm/hr

The optical power attenuation for the 125 mm/hr rain rate has been shown in fig.6.35. From this figure it has been clearly observed that almost 0.956 dB loss has been occurred.

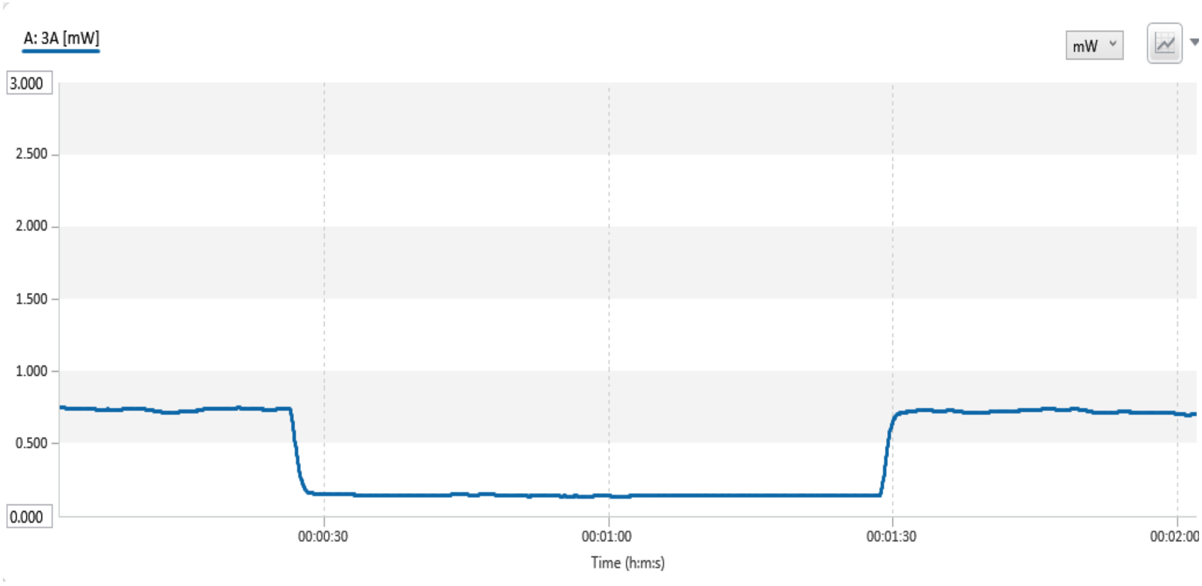

Fig.6.35. Optical Power Attenuation of 808nm & 980nm laser at a rain rate of 125 mm/hr

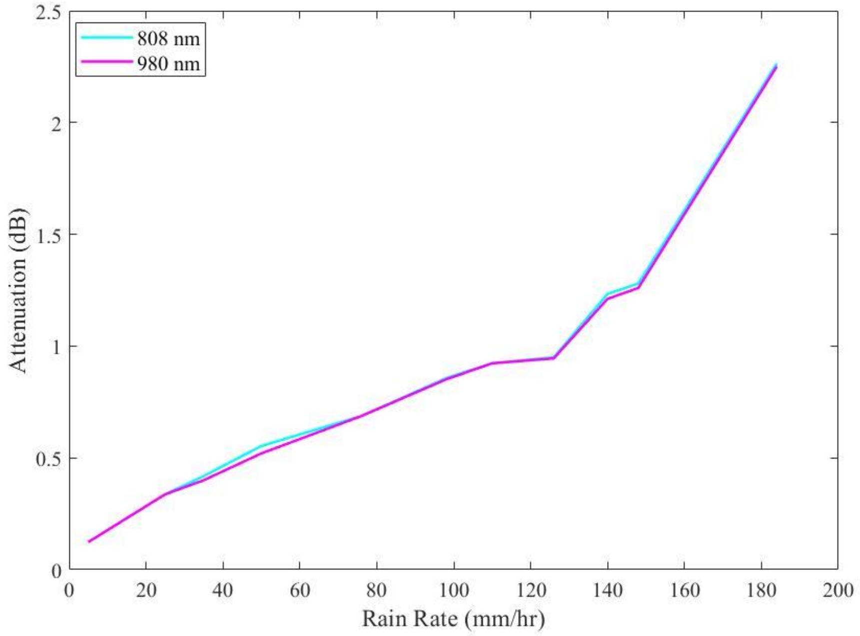

Fig.6.36. Optical power attenuation for different rain rates (mm/hr) (808 nm & 980 nm)

The optical power attenuation for different rain rates (mm/hr) are shown in fig.6.36. From the figure, it has been shown that both the wavelengths (808 nm, 980 nm) are attenuated in the different rain rates are almost same.

6.2. Channel Attenuation

6.2.1. Fog Experiment

For different visibility, the eye diagrams are also different for different wavelengths. For thin fog condition (1500m), photodetector signal is around 790 mV for 532 nm Laser, which is greater than the comparator threshold value, so the comparator works properly. Whereas the photodetector signal for the 650 nm is around 810 mV. The Eye Diagram of Photodetector Signal & Comparator Signal of 532 nm & 650 nm laser during the Very light Fog are shown in fig.6.37., fig.6.38.

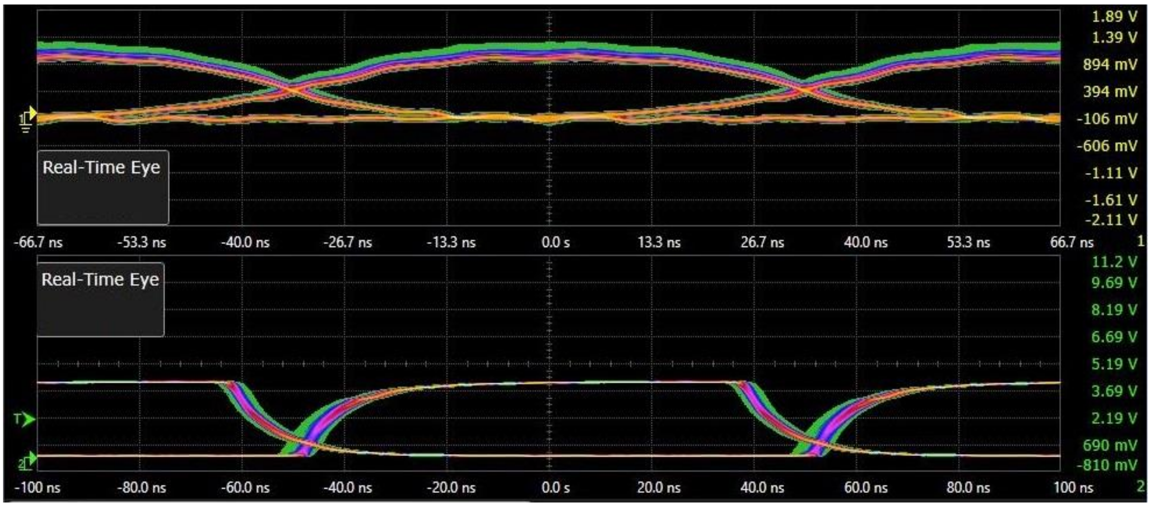

Fig.6.37. Eye Diagram of Photodetector Signal & Comparator Signal of 532nm laser during the light Fog

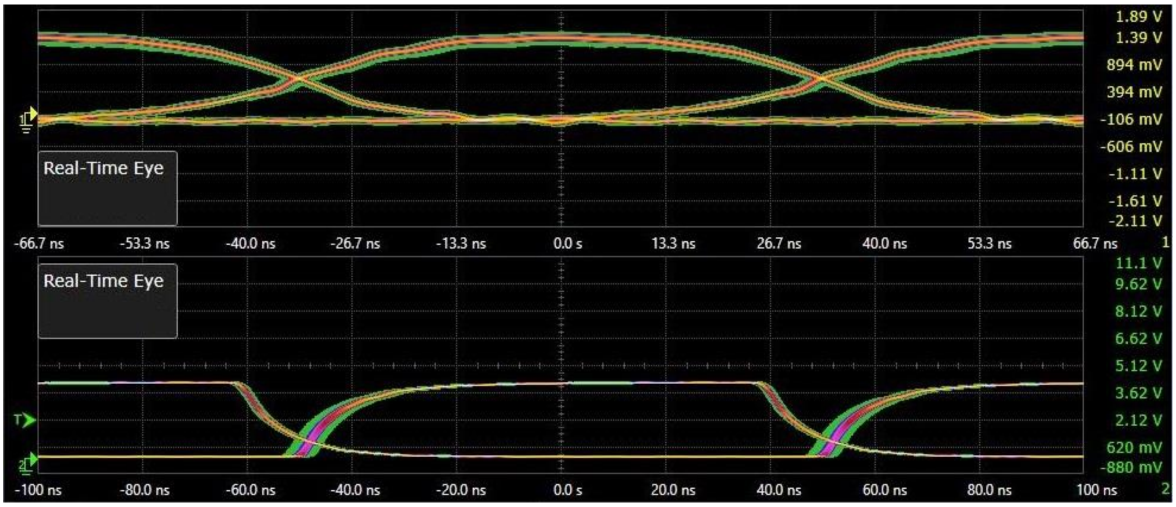

Fig.6.38. Eye Diagram of Photodetector Signal & Comparator Signal of 650 nm laser during light fog

For the medium visibility (700m) range, photodetector signal is around 488 mV for 532 nm Laser, which is greater than the comparator threshold value, so the comparator works properly. Whereas the photodetector signal for the 650 nm is around 515 mV. The Eye Diagram of Photodetector Signal & Comparator Signal of 532 nm & 650 nm laser during the medium Fog are shown in fig.6.39., fig.6.40.

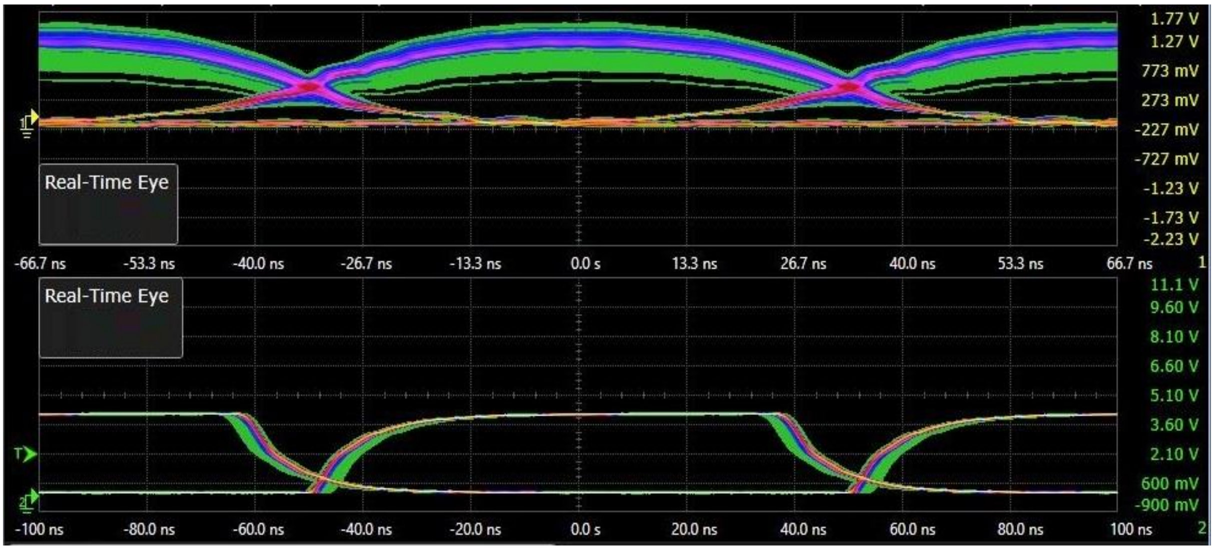

Fig.6.39. Eye Diagram of Photodetector Signal & Comparator Signal of 532 nm laser during medium fog

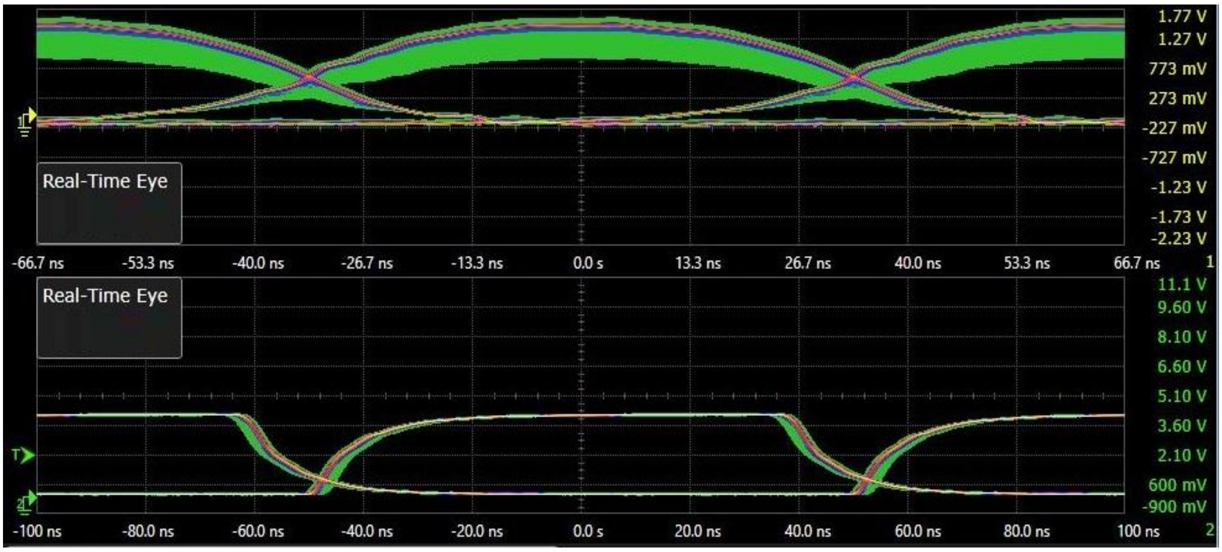

Fig.6.40. Eye Diagram of Photodetector Signal & Comparator Signal of 650 nm laser during medium fog

For the dense visibility (300 m) range, photodetector signal is around 48 mV for 532 nm Laser, which is lesser than the comparator threshold value, so the comparator is not working properly. Whereas the photodetector signal for the 650 nm is around 74 mV. The Eye Diagram of Photodetector Signal & Comparator Signal of 532 nm & 650 nm laser during the dense fog are shown in fig.6.41., fig.6.42.

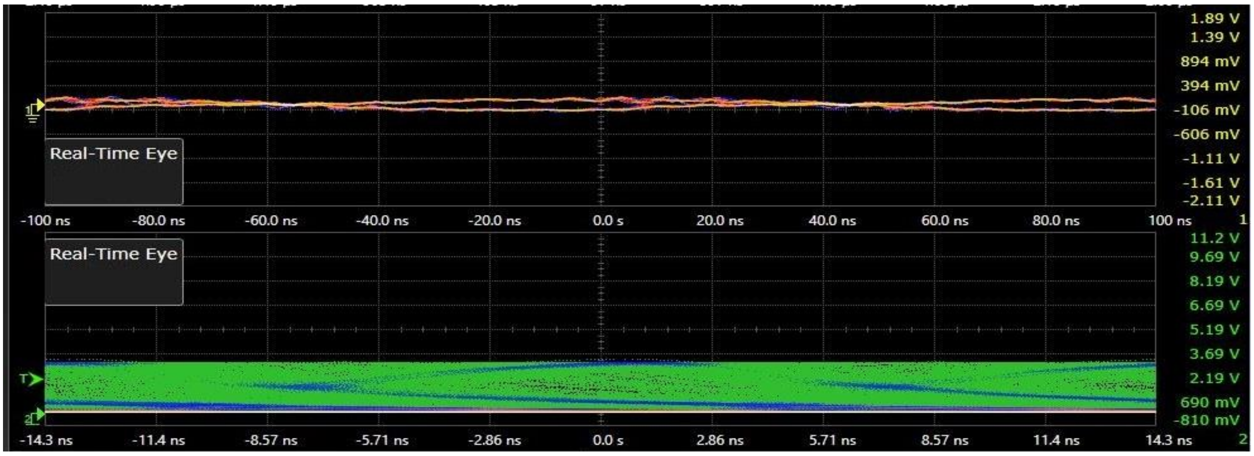

Fig.6.41. Eye Diagram of Photodetector Signal & Comparator Signal of 532 nm laser during dense fog

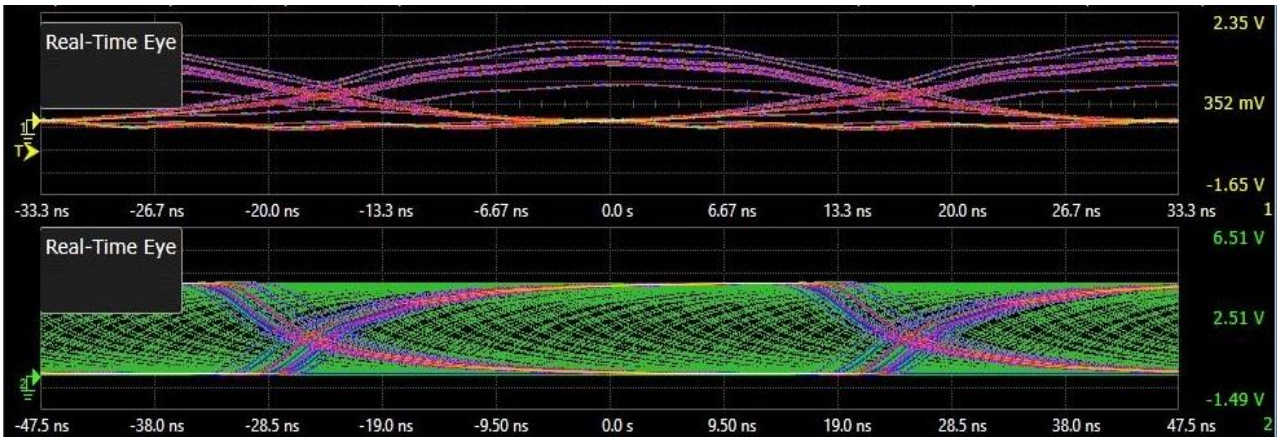

Fig.6.42. Eye Diagram of Photodetector Signal & Comparator Signal of 650 nm laser during dense fog

The SNR value and BER value for different visibility have been depicted in the fig.6.43 and fig.6.44. For light fog condition (1500 m), the SNR is around 112 for 532 nm and corresponding BER value is around 5.71x10^{-08}. Whereas 650 nm Laser source the SNR value is around 120 and corresponding BER value is around 2.66x10-^{8}. Similarly, for medium fog condition (700 m), the SNR is around 83.07 for 532 nm and corresponding BER value is around 2.59x10^{-6}. Whereas 650 nm Laser source the SNR value is around 85.1 and corresponding BER value is around 2x10^{-6}. Consequently, for dense fog condition (300 m), the SNR is around 36.1 for 532 nm and corresponding BER value is around 0.00125. Whereas 650 nm Laser source the SNR value is around 37.1 and corresponding BER value is around 0.00116.

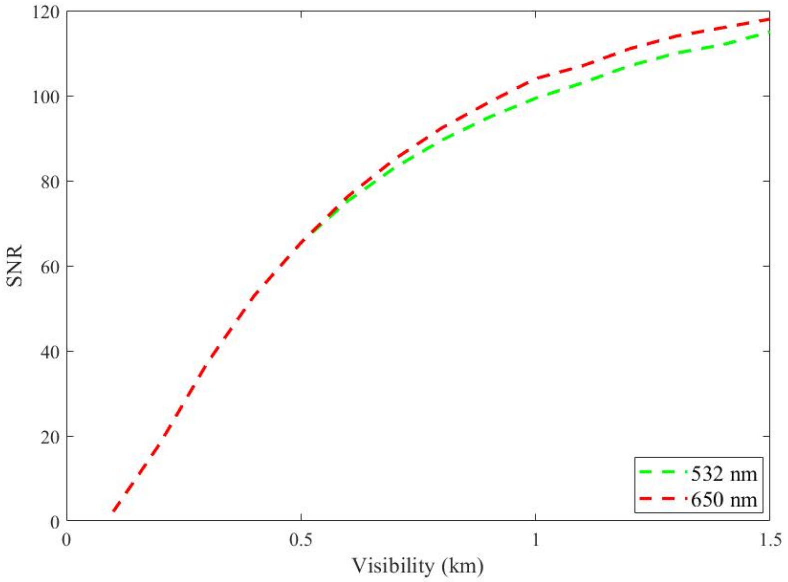

Fig.6.43. Different SNR value for different Visibility range (km) for 532 nm & 650 nm Laser

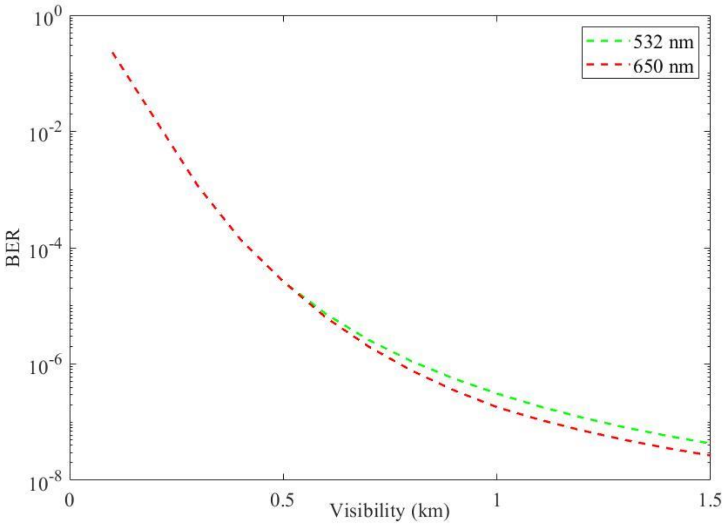

Fig.6.44. Different BER value for different Visibility range (km) for 532 nm & 650 nm Laser

Similarly, for thin fog condition (1500m), photodetector signal is around 818 mV for 808 nm Laser, which is greater than the comparator threshold value, so the comparator works properly. Whereas the photodetector signal for the 650 nm is around 838 mV. The Eye Diagram of Photodetector Signal & Comparator Signal of 808 nm & 980 nm laser during the light Fog are shown in fig.6.45., fig.6.46.

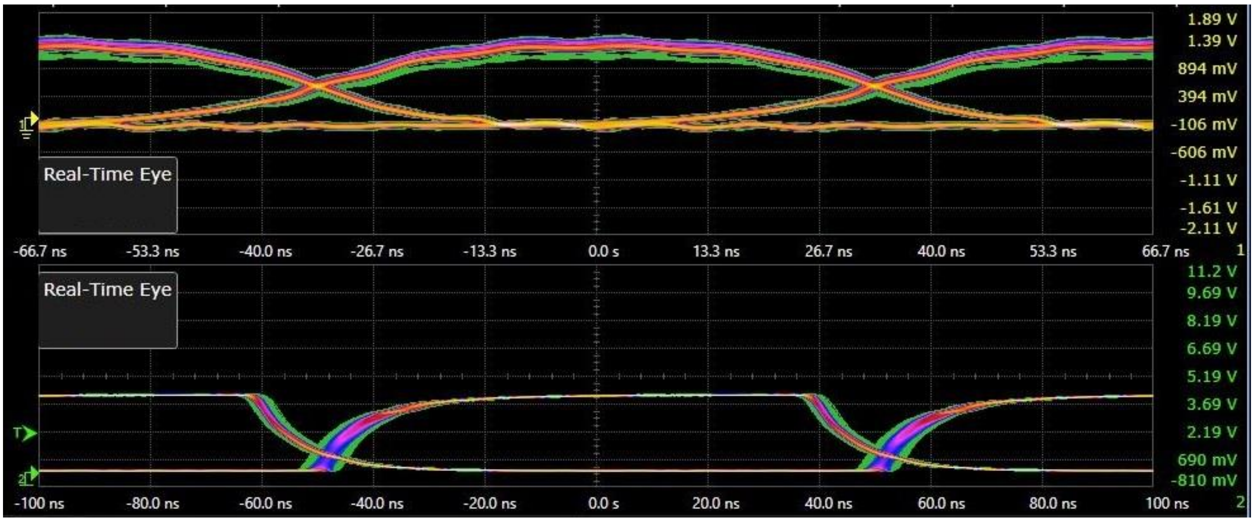

Fig.6.45. Eye Diagram of Photodetector Signal & Comparator Signal of 808 nm laser during light fog

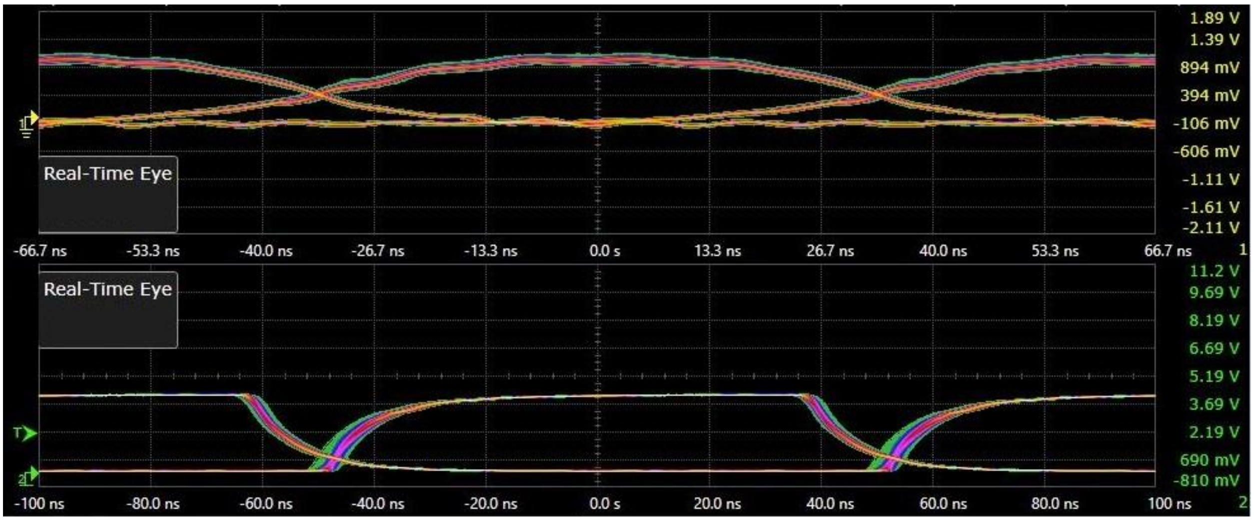

Fig.6.46. Eye Diagram of Photodetector Signal & Comparator Signal of 980 nm laser during light fog

For the medium visibility (700m) range, photodetector signal is around 494 mV for 808 nm Laser, which is greater than the comparator threshold value, so the comparator works properly. Whereas the photodetector signal for the 980 nm is around 518 mV. The Eye Diagram of Photodetector Signal & Comparator Signal of 808 nm & 980 nm laser during the medium Fog are shown in fig.6.47, fig.6.48.

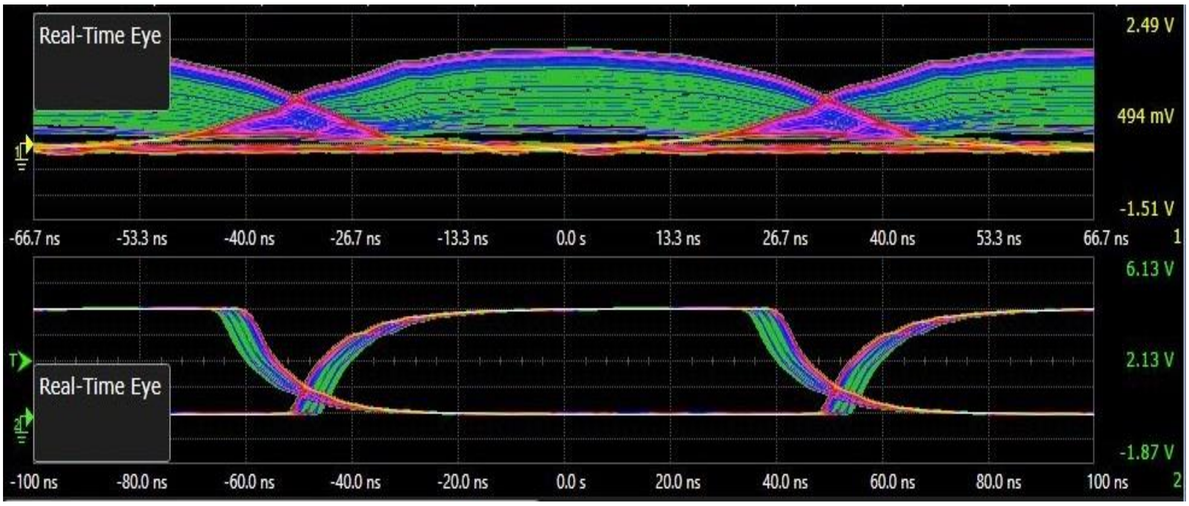

Fig.6.47. Eye Diagram of Photodetector Signal & Comparator Signal of 808 nm laser during medium fog

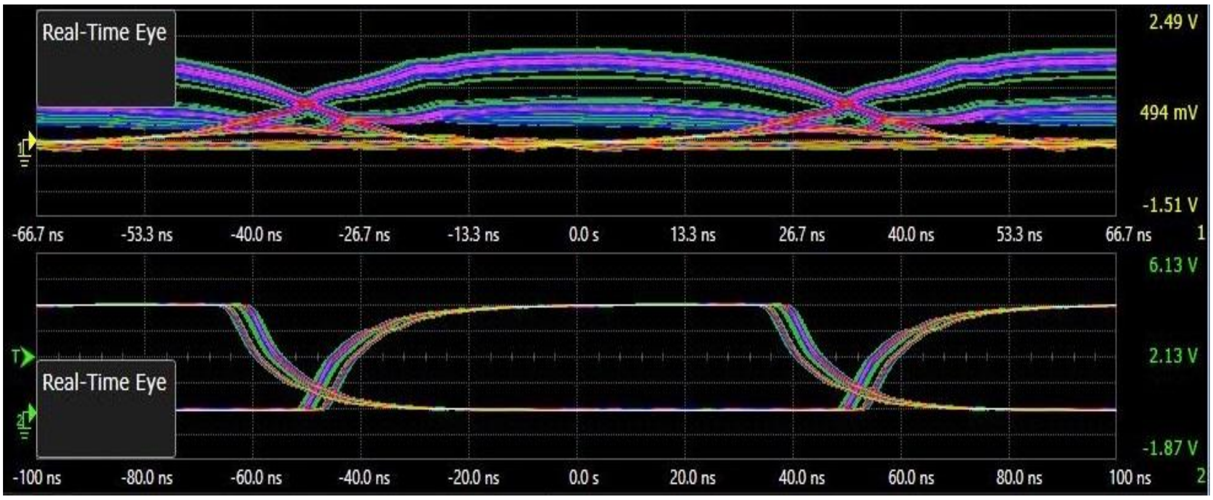

Fig.6.48. Eye Diagram of Photodetector Signal & Comparator Signal of 980 nm laser during medium fog

For the dense visibility (300 m) range, photodetector signal is around 22 mV for 808 nm Laser, which is lesser than the comparator threshold value, so the comparator is not working properly. Whereas the photodetector signal for the 980 nm is around 65 mV. The Eye Diagram of Photodetector Signal & Comparator Signal of 808 nm & 980 nm laser during the dense fog are shown in fig.6.49, fig.6.50.

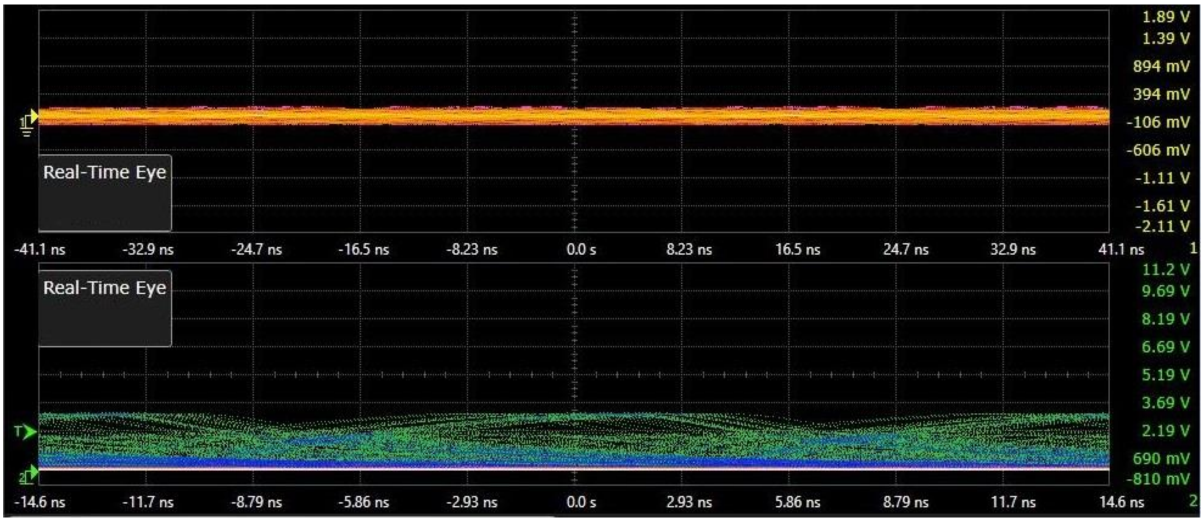

Fig.6.49. Eye Diagram of Photodetector Signal & Comparator Signal of 808 nm laser during dense fog

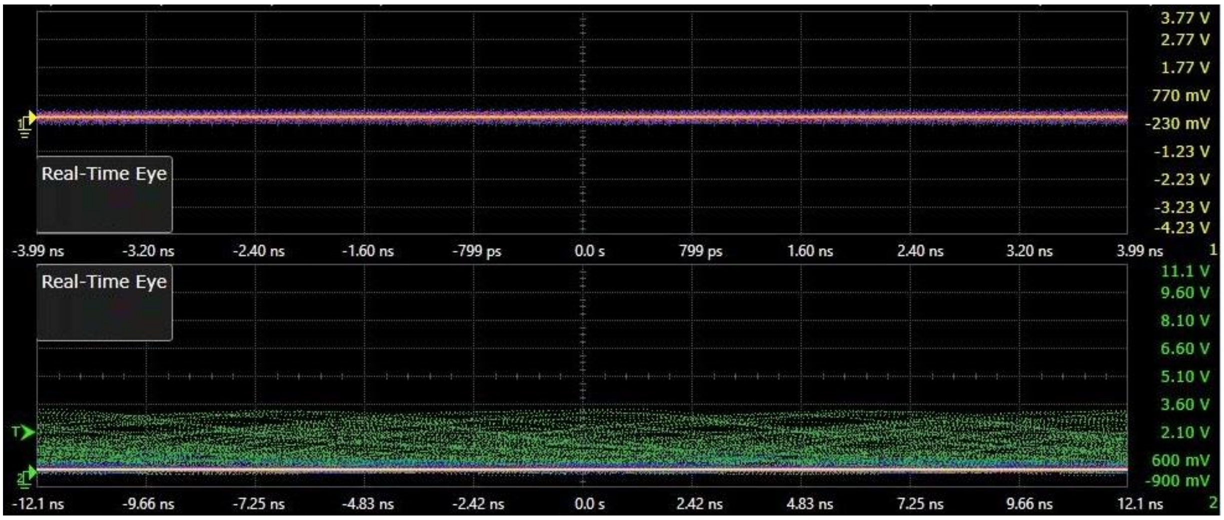

Fig.6.50. Eye Diagram of Photodetector Signal & Comparator Signal of 980 nm laser during dense fog

The SNR value and BER value for different visibility has been depicted in the fig.6.51. and fig.6.52. For light fog condition (1500 m), the SNR is around 185 for 808 nm and corresponding BER value is around 1.41x10^{-11}. Whereas 980 nm Laser source the SNR value is around 198 and corresponding BER value is around 2.66x10^{-12}. Similarly, for medium fog condition (700 m), the SNR is around 128 for 808 nm and corresponding BER value is around 5.5x10^{-8}. Whereas 980 nm Laser source the SNR value is around 132.5 and corresponding BER value is around 2x10^{-8}. Consequently, for dense fog condition (300 m), the SNR is around 39 for 808 nm and corresponding BER value is around 0.0005. Whereas 980 nm Laser source the SNR value is around 40.1 and corresponding BER value is around 0.00042.

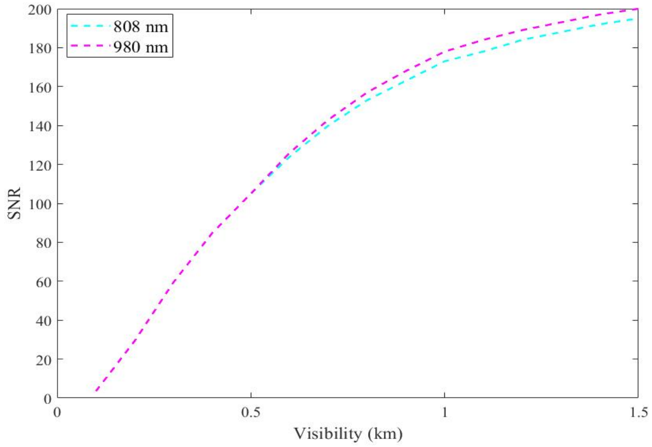

Fig.6.51. Different SNR value for different Visibility range (km) for 808 nm & 980 nm Laser

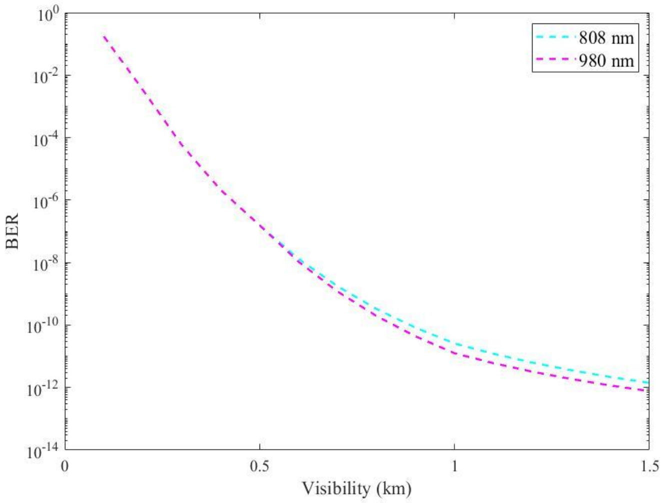

Fig.6.52. Different BERvalue for different Visibility range (km) for 808 nm & 980 nm Laser

6.2.2. Temperature Experiment

For different scintillation regime, the eye pattern are different wavelengths are given below. For lower scintillation regime (10^{-15}) range, the signal eye voltage is around 988 mV for 532 nm Laser, whereas for 650 nm Laser, 1.05 V signal strength has been obtained. As the comparator threshold (0.15 V) is well below the above-mentioned signal voltage level, so the comparator is worked properly.

Fig.6.53. and fig.6.54. are shown in the Eye Diagram of Photodetector Signal & Comparator Signal of 532nm & 650 nm Laser during the scintillation of 10^{-15}.

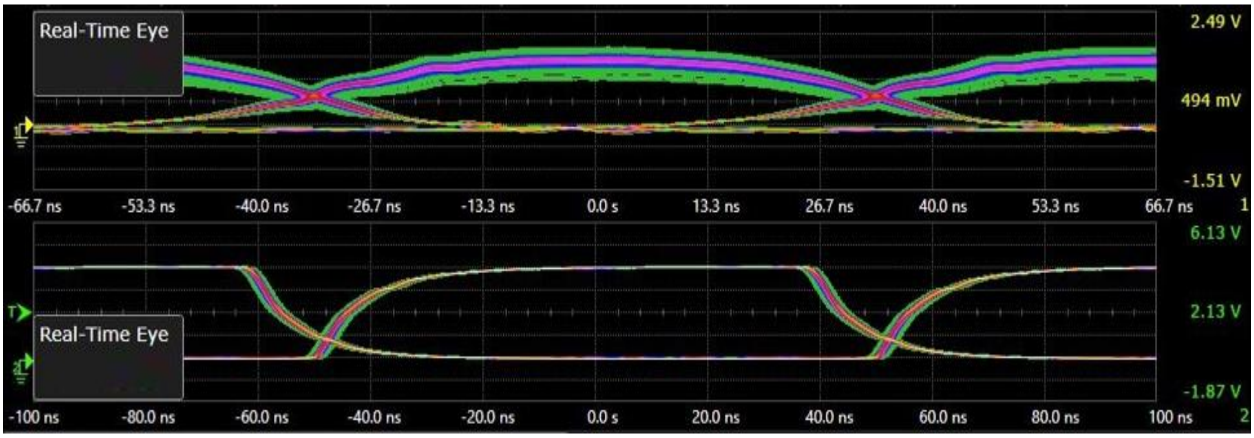

Fig.6.53. Eye Diagram of Photodetector Signal & Comparator Signal of 532nm laser during the scintillation of 10^{-15}

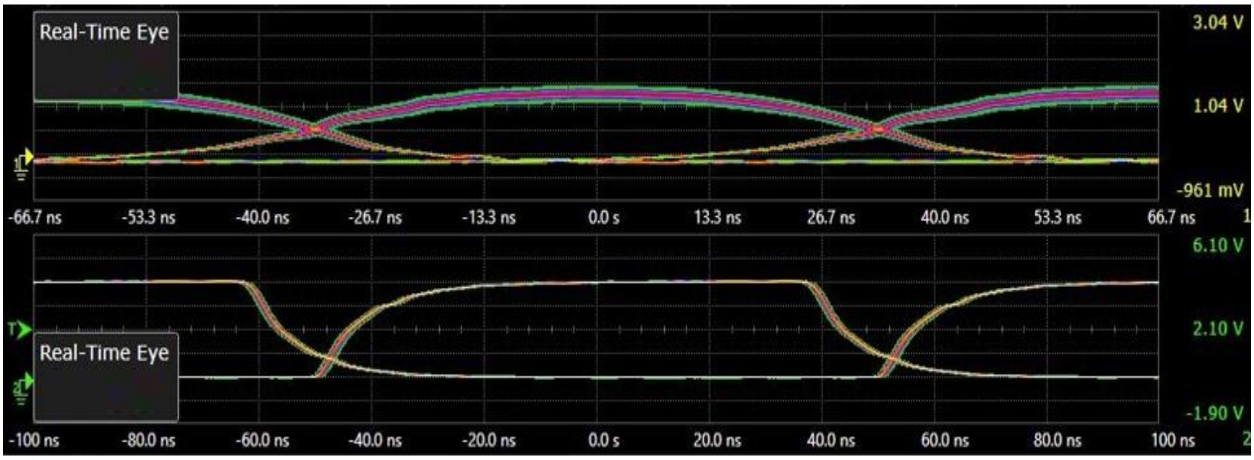

Fig.6.54. Eye Diagram of Photodetector Signal & Comparator Signal of 650nm laser during the scintillation of 10^{-15}

Similarly, for medium scintillation regime (10^{-13}) range, the signal eye voltage is around 520 mV for 532 nm Laser, whereas for 650 nm Laser, 588 mV signal strength has been obtained. As the comparator threshold (0.15 V) is well below the above mentioned signal voltage level, so the comparator is worked properly.

Fig.6.55. and fig.6.56. show the Eye Diagram of Photodetector Signal & Comparator Signal of 532nm & 650 nm Laser during the scintillation of 10^{-13}.

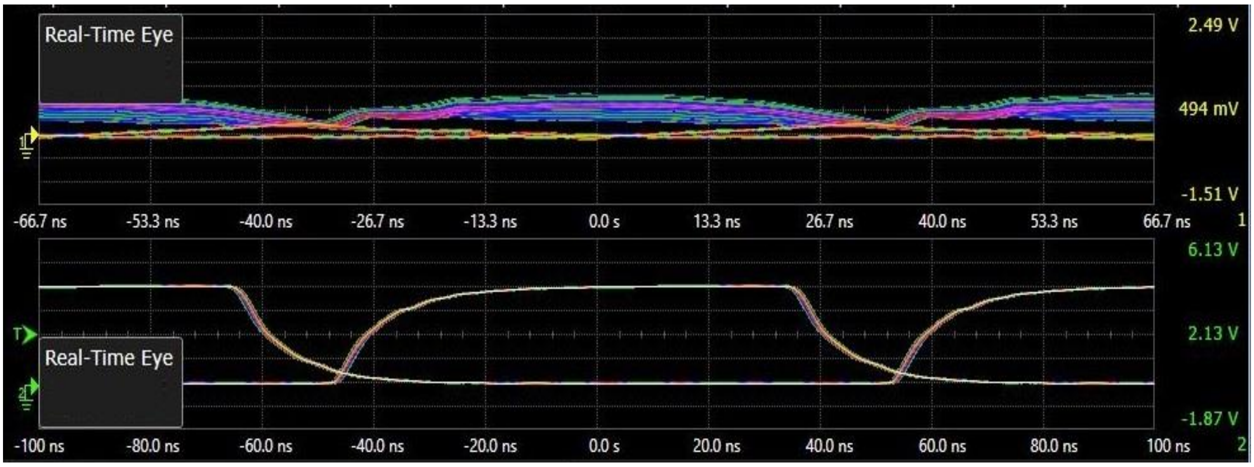

Fig.6.55. Eye Diagram of Photodetector Signal & Comparator Signal of 532nm laser during the scintillation of 10^{-13}

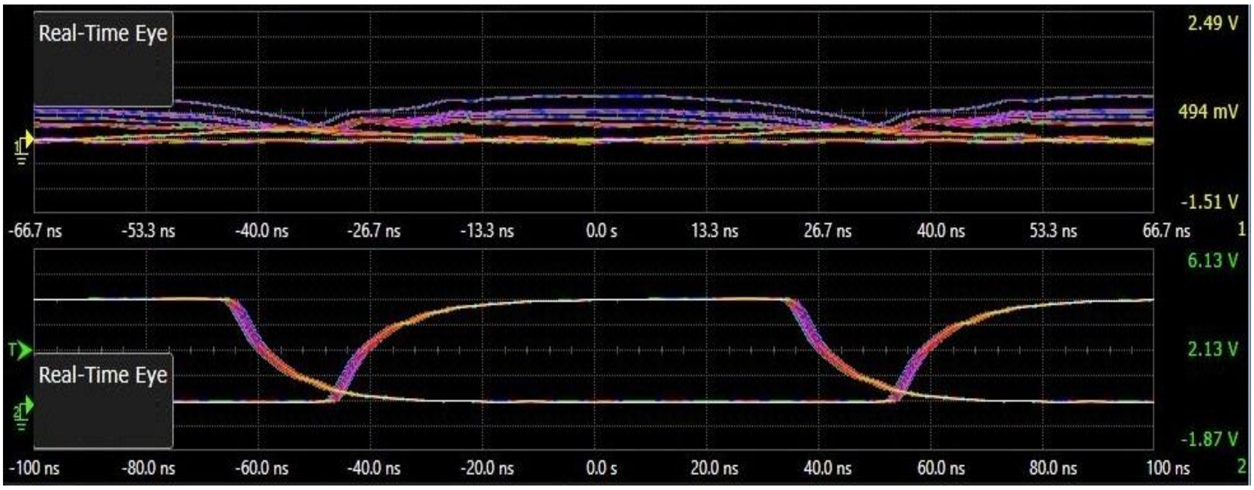

Fig.6.56. Eye Diagram of Photodetector Signal & Comparator Signal of 650nm laser during the scintillation of 10^{-13}

Consequently, for higher scintillation regime ($5x10^{-12}$) range, the signal eye voltage is around 98 mV for 532 nm Laser, whereas for 650 nm Laser, 124 mV signal strength has been obtained. As the comparator threshold (0.15 V) is well above the above-mentioned signal voltage level, so the comparator is not worked properly in this regime.

Fig.6.57. and fig.6.58. show the Eye Diagram of Photodetector Signal & Comparator Signal of 532nm & 650 nm Laser during the scintillation of 5x10^{-12}.

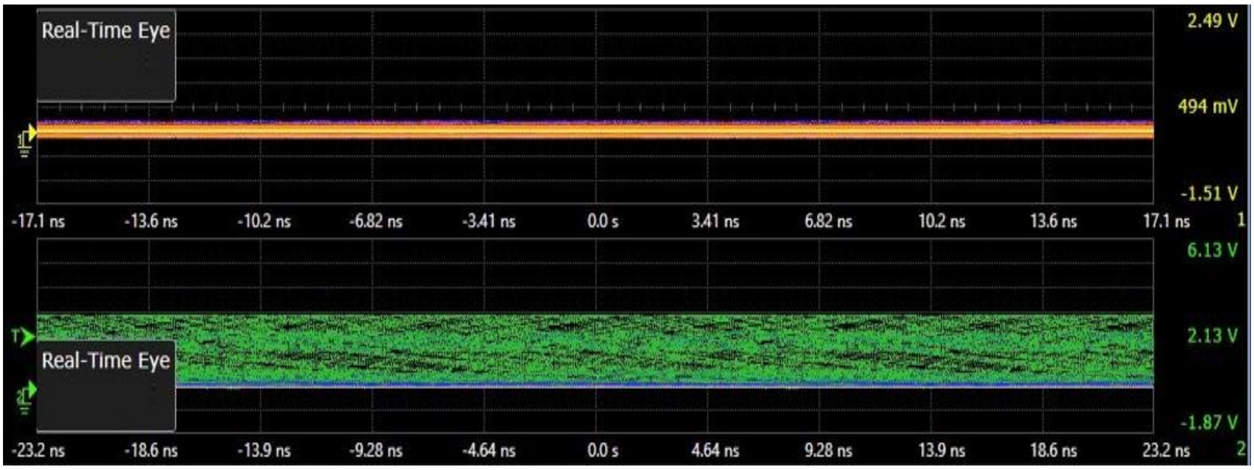

Fig.6.57. Eye Diagram of Photodetector Signal & Comparator Signal of 532nm laser during the scintillation of 5x10^{-12}

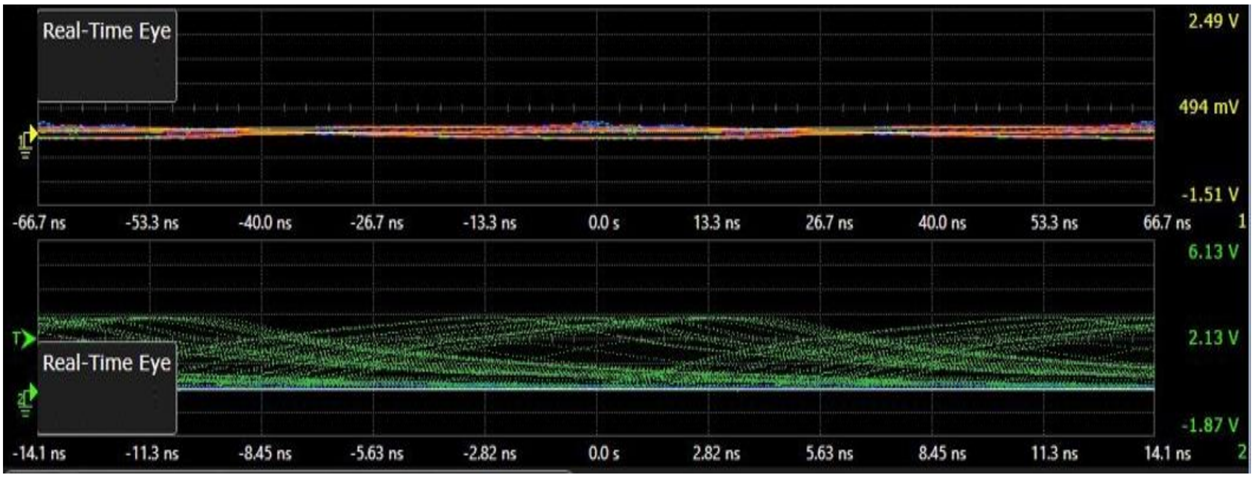

Fig.6.58. Eye Diagram of Photodetector Signal & Comparator Signal of 650nm laser during the scintillation of 5x10^{-12}

For the Scintillation of 10^{-15}, the SNR value for 532 nm is around 21.5 dB and corresponding BER value is around 5x10^{-10}, similarly, the SNR value for 650 nm is around 21.8 dB and corresponding BER value is around 4.5x10^{-10}.

Again, For the Scintillation of 10^{-13}, the SNR value for 532 nm is around 17 dB and corresponding BER value is around $8x10^{-17}$, similarly, the SNR value for 650 nm is around 17.5 dB and corresponding BER value is around $5x10^{-7}$.

Consequently, For the Scintillation of $5x10^{-12}$, the SNR value for 532 nm is around 6.7 dB and corresponding BER value is around $3.3x10^{-2}$, similarly, the SNR value for 650 nm is around 7.1 dB and corresponding BER value is around $1.5x10^{-2}$. Fig.6.59. and fig.6.60. shows the different Scintillation Index Parameter Structure vs SNR for 532 nm & 650 nm and Different Scintillation Index Parameter Structure vs BER for 532 nm & 650 nm.

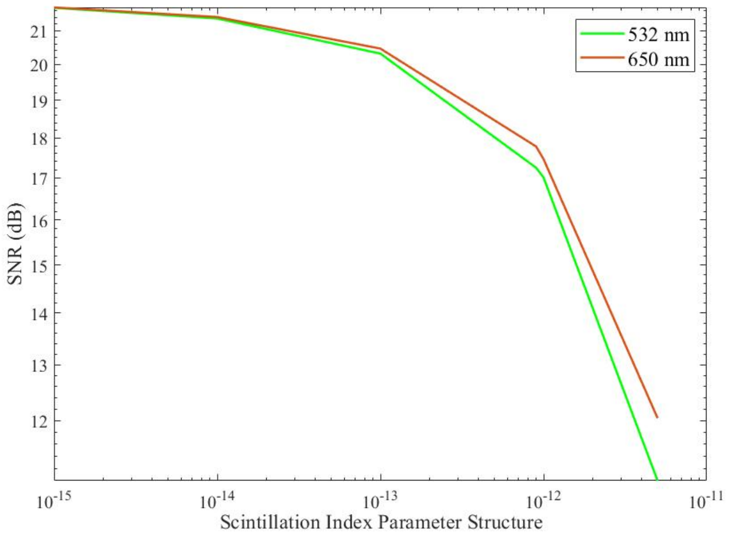

Fig.6.59. Different Scintillation Index Parameter Structure vs SNR for 532 nm & 650 nm

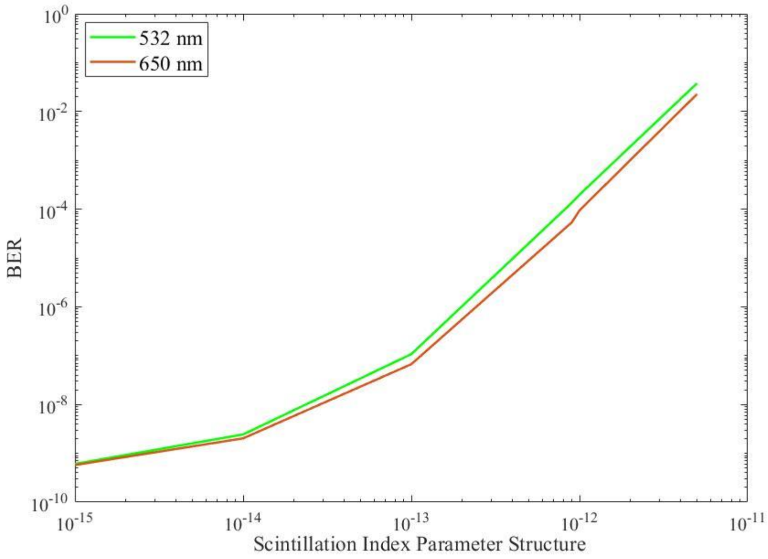

Fig.6.60. Different Scintillation Index Parameter Structure vs BER for 532 nm & 650 nm

For lower scintillation regime (10^{-15}) range, the signal eye voltage is around 1.02 V for 808 nm Laser, whereas for 980 nm Laser, 1.1 V signal strength has been obtained. As the comparator threshold (0.15 V) is well below the above -mentioned signal voltage level, so the comparator is worked properly. Fig.6.61. and fig.6.62. depict the Eye Diagram of Photodetector Signal & Comparator Signal of 808 nm & 980 nm Laser during the scintillation of 10^{-15}.

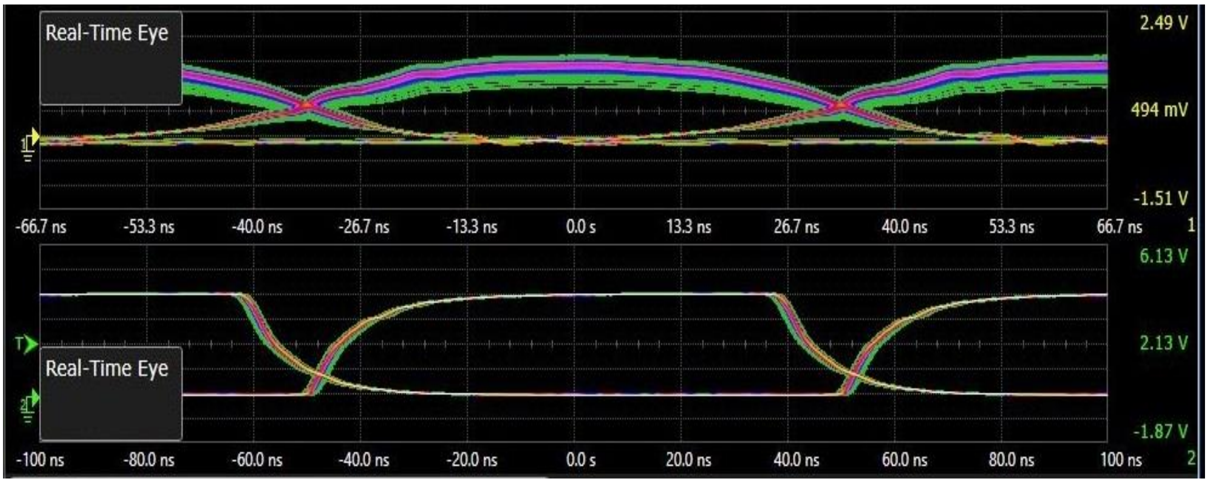

Fig.6.61. Eye Diagram of Photodetector Signal & Comparator Signal of 808nm laser during the scintillation of 10^{-15}

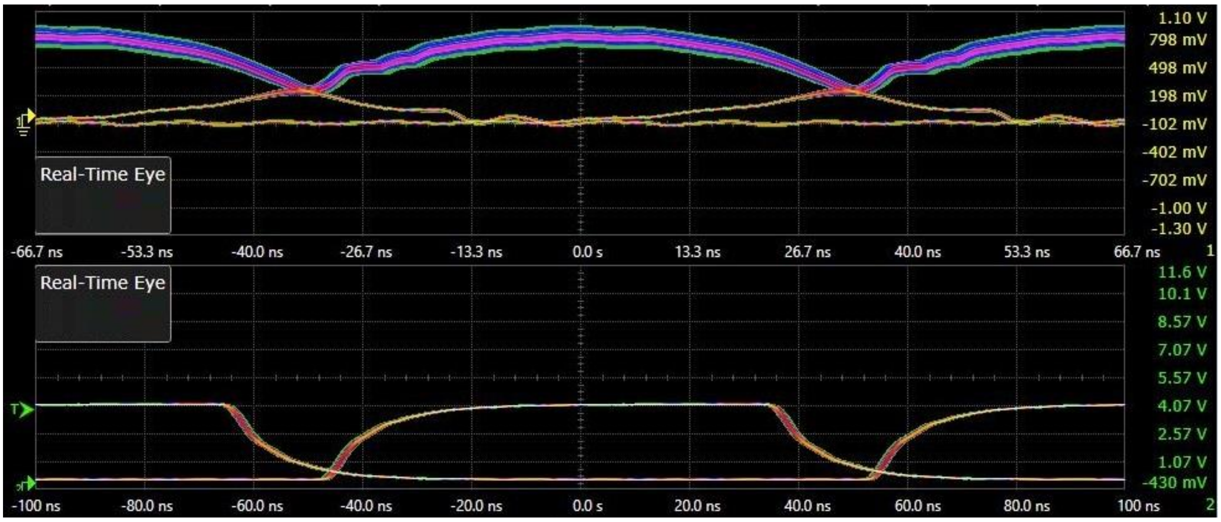

Fig.6.62. Eye Diagram of Photodetector Signal & Comparator Signal of 980nm laser during the scintillation of 10^{-15}

Similarly, for medium scintillation regime (10^{-14}) range, the signal eye voltage is around 520 mV for 808 nm Laser, whereas for 980 nm Laser, 552 mV signal strength has been obtained. As the comparator threshold (0.15 V) is well below the above mentioned signal voltage level, so the comparator is worked properly.

Fig.6.63. and fig6.64. show the Eye Diagram of Photodetector Signal & Comparator Signal of 808 nm & 980 nm Laser during the scintillation of 10^{-14}.

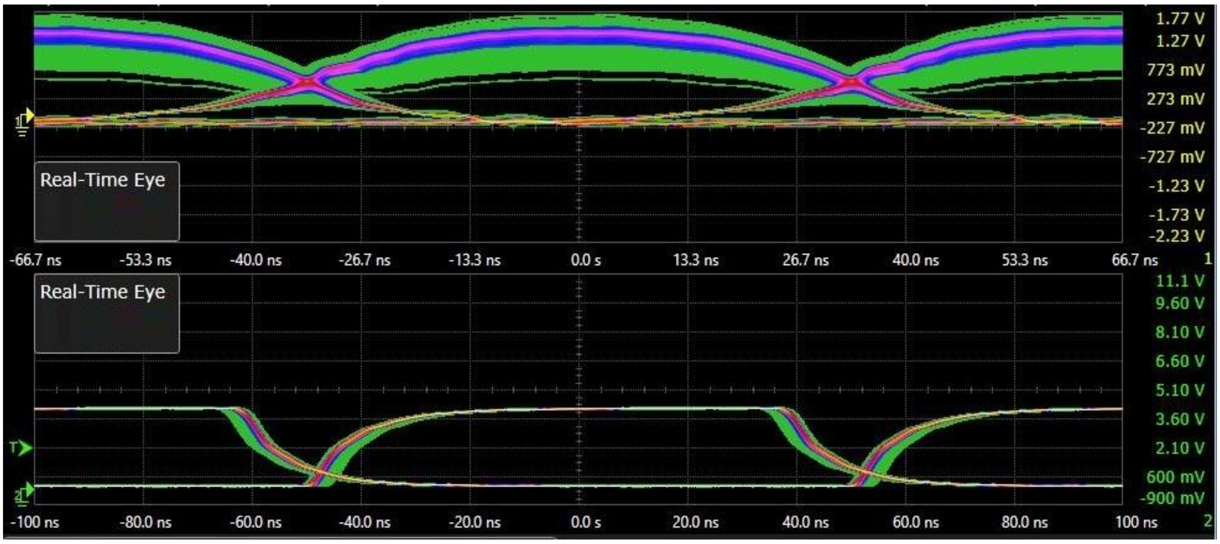

Fig.6.63. Eye Diagram of Photodetector Signal & Comparator Signal of 808nm laser during the scintillation of 10^{-14}

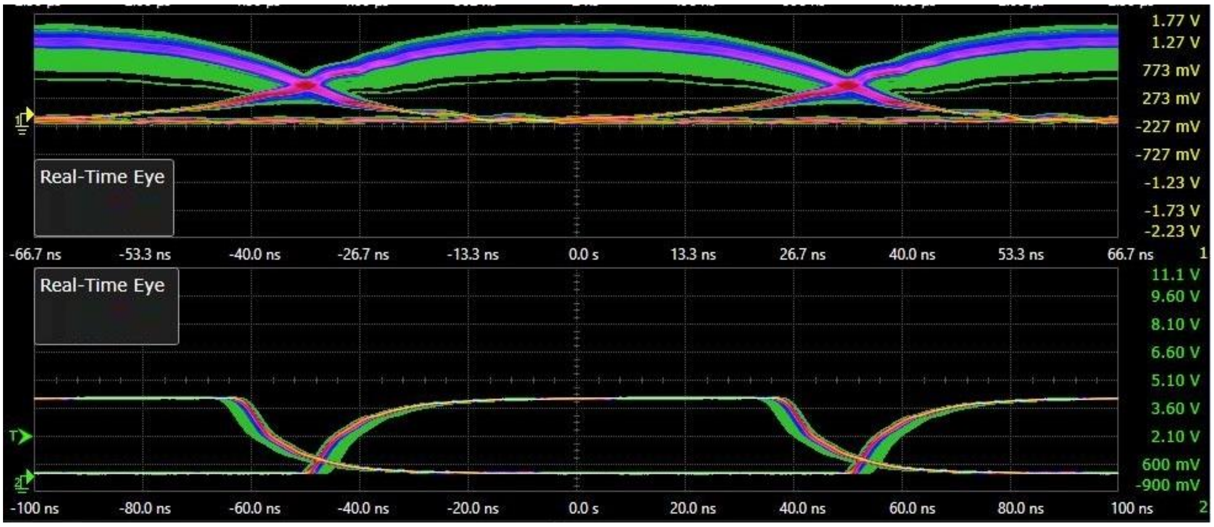

Fig.6.64. Eye Diagram of Photodetector Signal & Comparator Signal of 980nm laser during the scintillation of 10^{-14}

Consequently, for higher scintillation regime ($5x10^{-12}$) range, the signal eye voltage is around 82 mV for 808 nm Laser, where as for 980 nm Laser, 112 mV signal strength has been obtained. As the comparator threshold (0.15 V) is well above the above-mentioned signal voltage level, so the comparator is not worked properly in this regime.

Fig.6.65. and fig.6.66. show the Eye Diagram of Photodetector Signal & Comparator Signal of 808 nm & 980 nm Laser during the scintillation of $5x10^{-12}$.

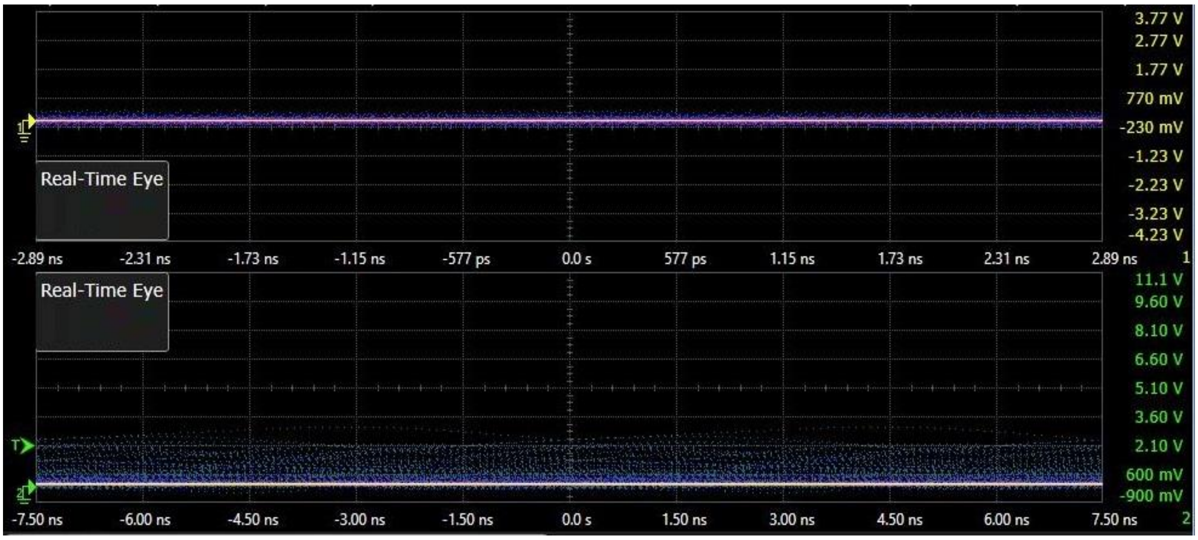

Fig.6.65. Eye Diagram of Photodetector Signal & Comparator Signal of 808nm laser during the scintillation of $5x10^{-12}$

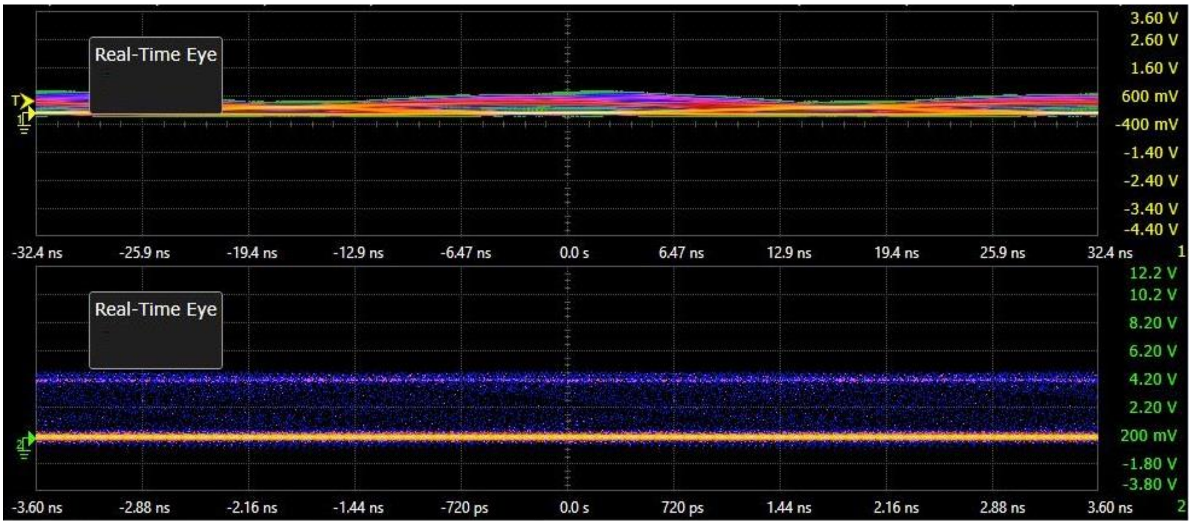

Fig.6.66. Eye Diagram of Photodetector Signal & Comparator Signal of 980nm laser during the scintillation of $5x 10^{-12}$

For the Scintillation of 10^{-15}, the SNR value for 808 nm is around 24.2 dB and corresponding BER value is around $7x10^{-15}$, similarly, the SNR value for 980 nm is around 24.7 dB and corresponding BER value is around $5.5x10^{-15}$.

Again, For the Scintillation of 10^{-13}, the SNR value for 808 nm is around 22.4 dB and corresponding BER value is around $8.5x10^{-12}$, similarly, the SNR value for 980 nm is around 22.8 dB and corresponding BER value is around $5.45x10^{-12}$.

Consequently, For the Scintillation of $5x10^{-12}$, the SNR value for 808 nm is around 8.9 dB and corresponding BER value is around $6.85x10^{-3}$, similarly, the SNR value for 980 nm is around 14 dB and corresponding BER value is around $1x10^{-3}$. Fig.6.67. and fig.6.68. shows the different Scintillation Index Parameter Structure vs SNR for 808 nm & 980 nm and Different Scintillation Index Parameter Structure vs BER for 808 nm & 980 nm.

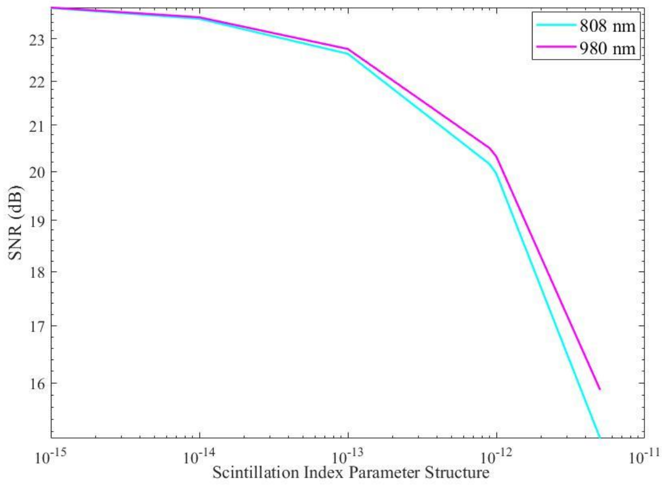

Fig.6.67. Different Scintillation Index Parameter Structure vs SNR for 808 nm & 980 nm

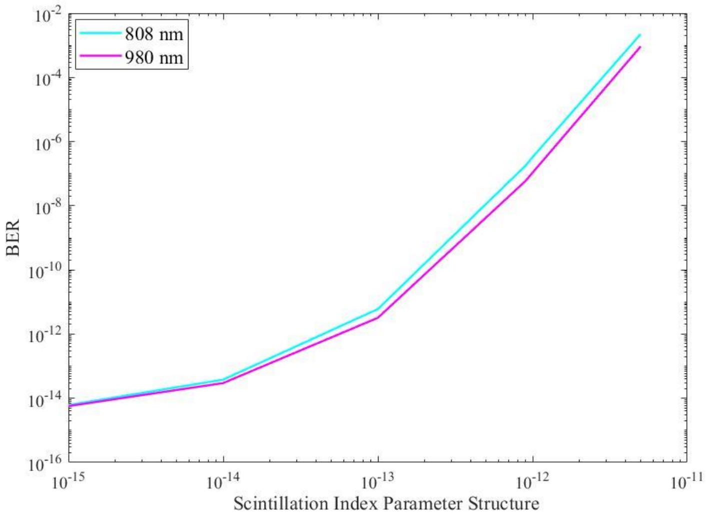

Fig.6.68. Different Scintillation Index Parameter Structure vs BER for 808 nm & 980 nm

6.2.3. Rain Experiment

The rain rate for 5 mm/hr the signal strength is around 1.461 V. As the comparator threshold limit is around 0.15 V, which is well below the signal strength, so the comparator is worked properly. fig.6.69. shows the Eye Diagram of Photodetector Signal & Comparator Signal of 532nm & 650nm laser at a rain rate of 5 mm/hr.

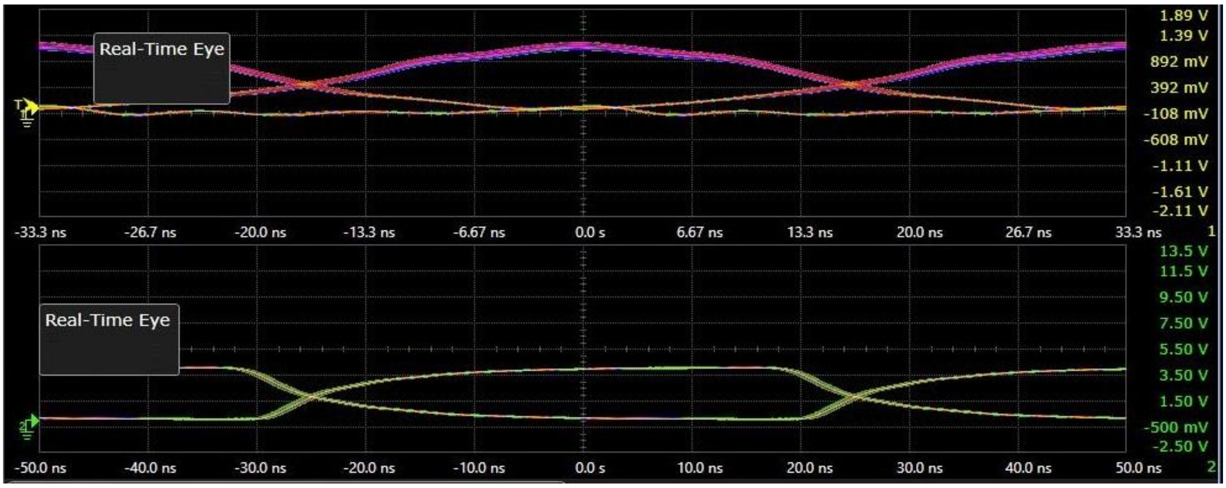

Fig.6.69. Eye Diagram of Photodetector Signal & Comparator Signal of 532nm & 650nm laser at a rain rate of 5 mm/hr

Similarly, for the rain rate of 34 mm/hr, the signal voltage is around 996 mV. This value is also higher than the comparator threshold value, so, it works properly. fig.6.70. shows the Eye Diagram of Photodetector Signal & Comparator Signal of 532nm & 650nm laser at a rain rate of 34 mm/hr.

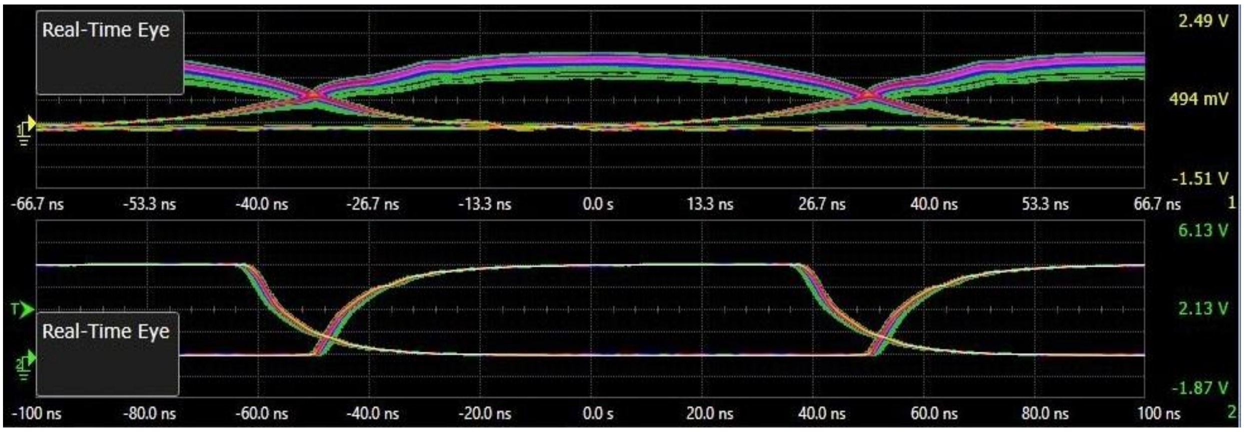

Fig.6.70. Eye Diagram of Photodetector Signal & Comparator Signal of 532nm & 650nm laser at a rain rate of 34 mm/hr

Similarly, for the rain rate of 68 mm/hr, the signal voltage is around 780 mV. This value is also higher than the comparator threshold value, so, it works properly. Fig.6.71. shows the Eye Diagram of Photodetector Signal & Comparator Signal of 532nm & 650nm laser at a rain rate of 68 mm/hr

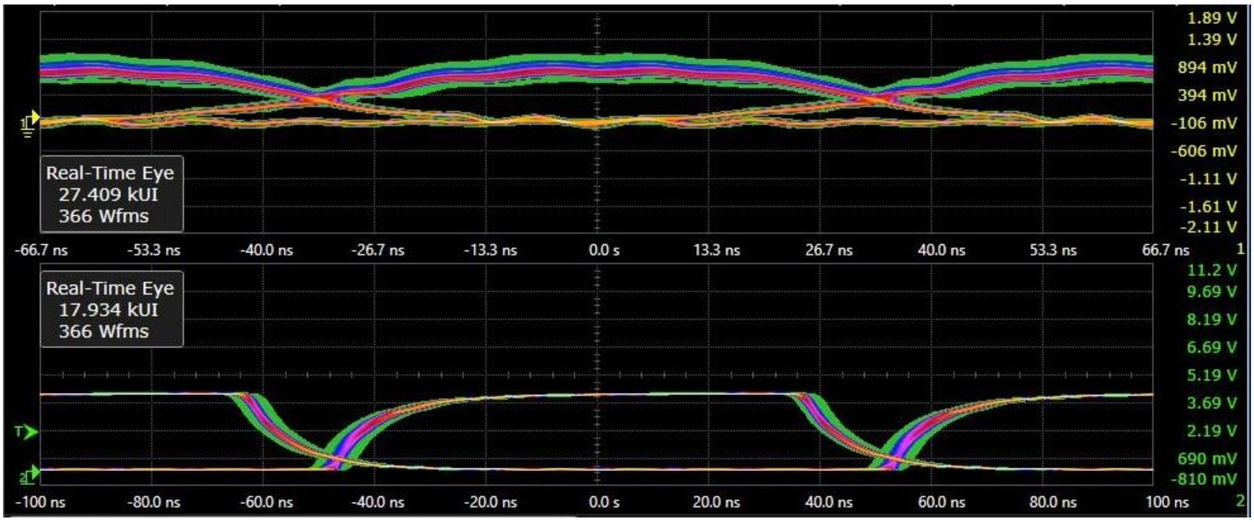

Fig.6.71. Eye Diagram of Photodetector Signal & Comparator Signal of 532nm & 650nm laser at a rain rate of 68 mm/hr

Consequently, for the rain rate of 125 mm/hr, the signal voltage is around 530 mV. This value is also higher than the comparator threshold value, so, it works properly. Fig.6.72. shows the Eye Diagram of Photodetector Signal & Comparator Signal of 532nm & 650nm laser at a rain rate of 125 mm/hr

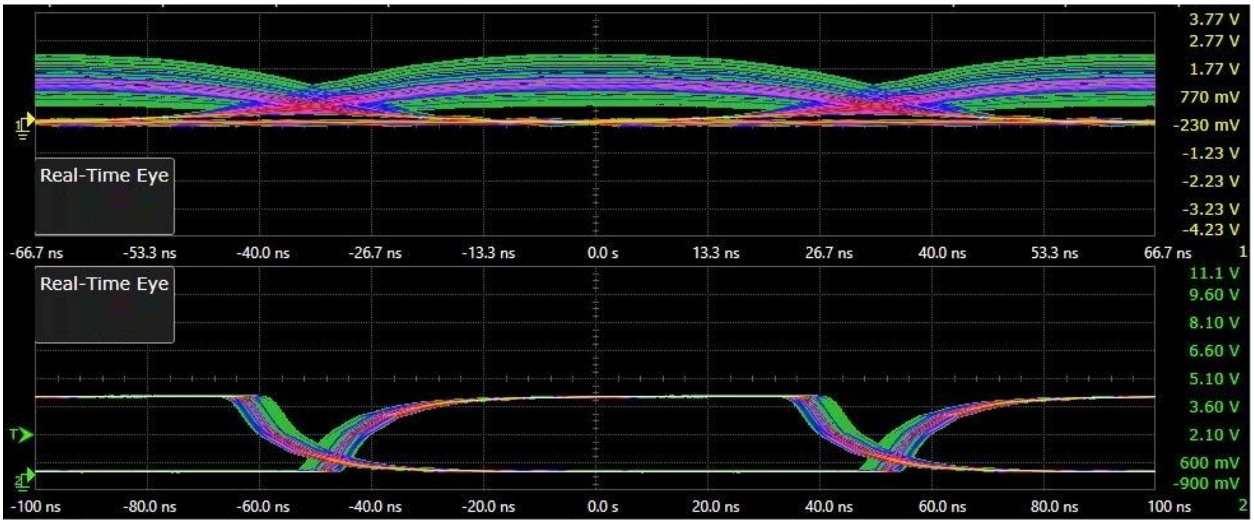

Fig.6.72. Eye Diagram of Photodetector Signal & Comparator Signal of 532nm & 650nm laser at a rain rate of 125 mm/hr

For rain rate 5 mm/hr, the SNR value for the both the wavelengths are almost same. The SNR value for these wavelengths are around 21.5 dB and corresponding BER value are 3.5x10^{-9}. Similarly, for rain rate of 35 mm/hr, the SNR values are 20.2 dB for the both the wavelengths and corresponding BER value is around 9x10^{-8}. Consequently, for the rain rate of 92 mm/hr, the SNR value is around 17.8 dB and corresponding BER value is 6.8x10^{-6}. When the rain rate is very large like 184 mm/hr, the SNR value for 532 nm is around 7.8 dB and for 650 nm value is 8.1 dB respectively and corresponding BER values are 6x10^{-3} and 5.5x10^{-3} respectively. Fig.6.73. show the different SNR value for different rain rates (mm/hr) and fig.6.74. different BER value for different rain rates (mm/hr).

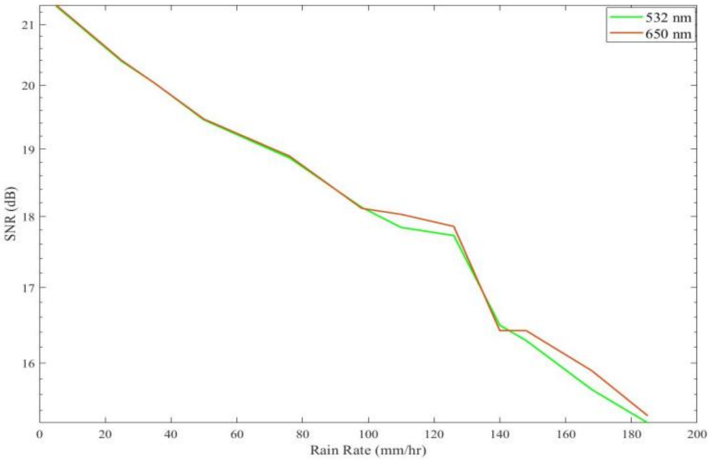

Fig.6.73. Different SNR value for different rain rates (mm/hr)

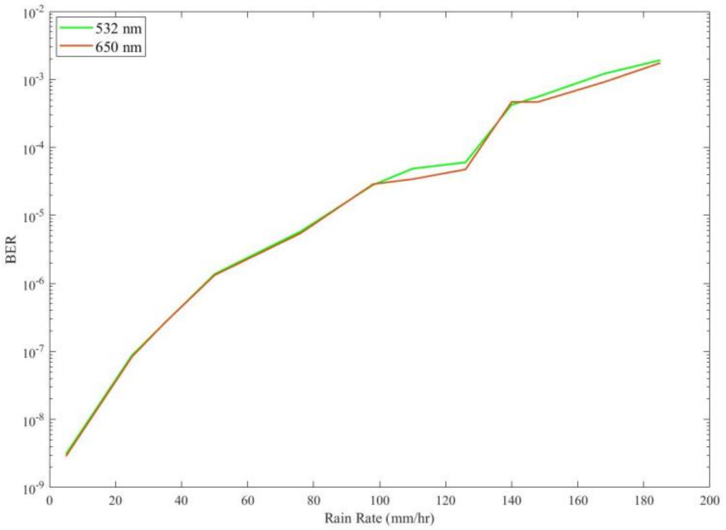

Fig.6.74. Different BER value for different rain rates (mm/hr)

The rain rate for 5 mm/hr the signal strength is around 1.45 V. As the comparator threshold limit is around 0.15 V, which is well below the signal strength, so the comparator is worked properly. Fig.6.75. shows the Eye Diagram of Photodetector Signal & Comparator Signal of 808 nm & 980nm laser at a rain rate of 34 mm/hr.

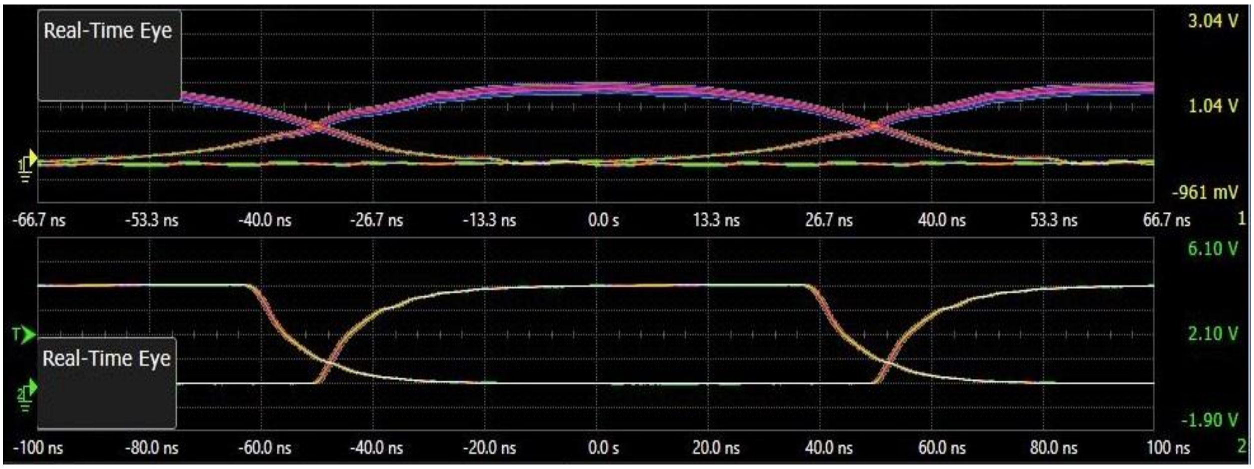

Fig.6.75. Eye Diagram of Photodetector Signal & Comparator Signal of 808nm & 980nm laser at a rain rate of 5 mm/hr

Similarly, for the rain rate of 34 mm/hr, the signal voltage is around 1.266 V. This value is also higher than the comparator threshold value, so, it works properly. Fig.6.76. shows the Eye Diagram of Photodetector Signal & Comparator Signal of 808 nm & 980 nm laser at a rain rate of 34 mm/hr.

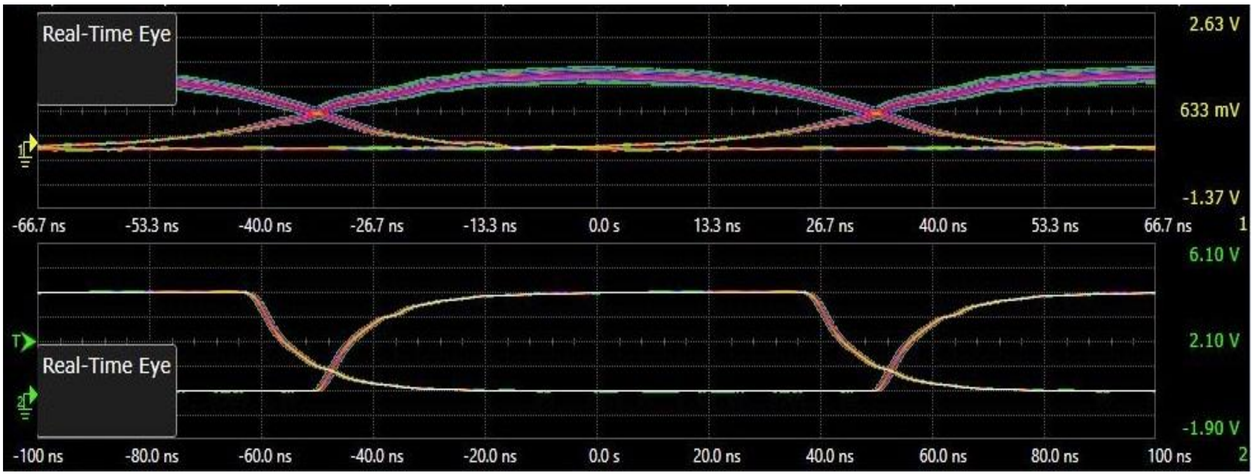

Fig.6.76. Eye Diagram of Photodetector Signal & Comparator Signal of 808nm & 980nm laser at a rain rate of 34 mm/hr

Consequently, for the rain rate of 68 mm/hr, the signal voltage is around 546 V. This value is also higher than the comparator threshold value, so, it works properly. Fig.6.77. shows the

Eye Diagram of Photodetector Signal & Comparator Signal of 808 nm & 980 nm laser at a rain rate of 92 mm/hr.

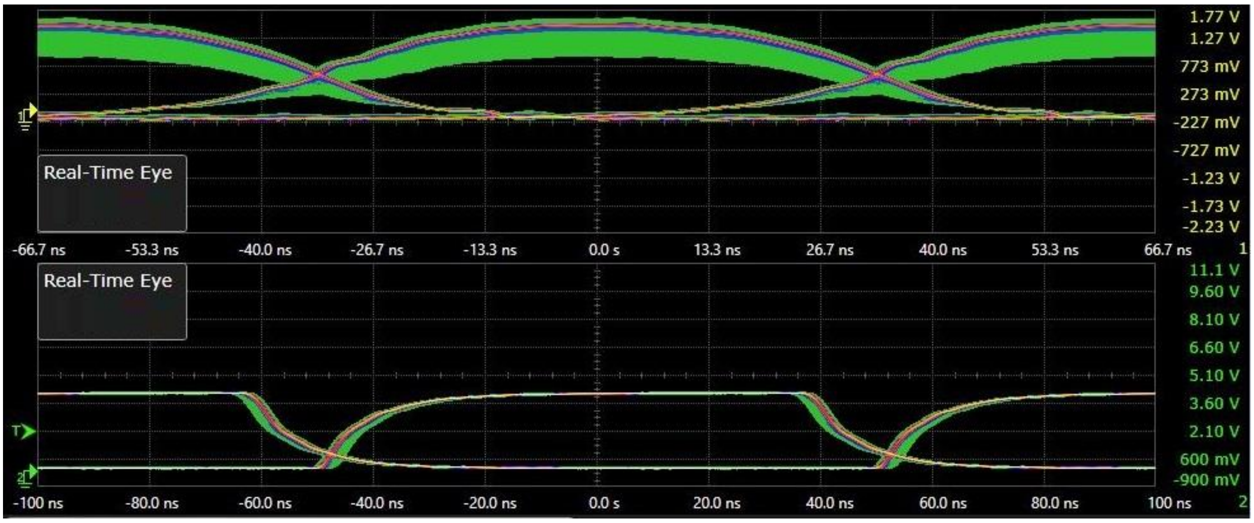

Fig.6.77. Eye Diagram of Photodetector Signal & Comparator Signal of 808nm & 980nm laser at a rain rate of 92 mm/hr

Similarly, for the rain rate of 125 mm/hr, the signal voltage is around 485 mV. This value is also higher than the comparator threshold value, so, it works properly. Fig.6.78. shows the Eye Diagram of Photodetector Signal & Comparator Signal of 808 nm & 980 nm laser at a rain rate of 125 mm/hr.

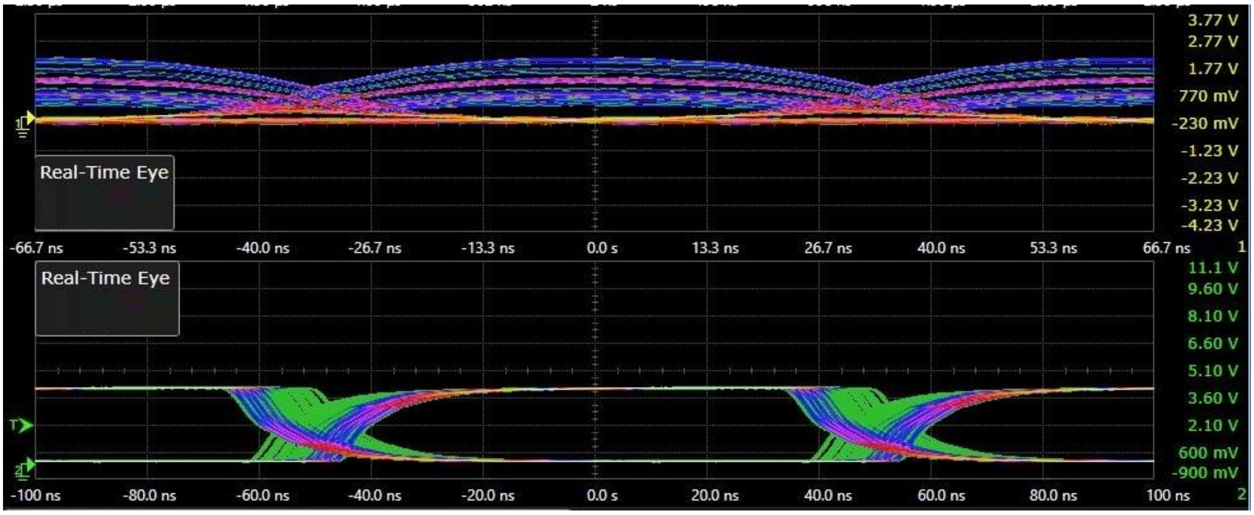

Fig.6.78. Eye Diagram of Photodetector Signal & Comparator Signal of 808nm & 980nm laser at a rain rate of 125 mm/hr

For rain rate 5 mm/hr, the SNR value for the both the wavelengths are almost same. The SNR value for these wavelengths are around 22.7 dB and corresponding BER value are 7x10^{-11}. Similarly, for rain rate of 35 mm/hr, the SNR values are 21.52 dB for the both the wavelengths and corresponding BER value is around 5.3x10^{-9}. Consequently, for the rain rate of 92 mm/hr, the SNR value is around 19.1 dB and corresponding BER value is 4.5x10^{-7}. When the rain rate is very large like 184 mm/hr, the SNR value for808 nm is around 10 dB and for 650 nm value is 10.4 dB respectively and corresponding BER values are 7.84 x10^{-4} and 6.84x10^{-4} respectively. Fig.6.79. show the different SNR value for different rain rates (mm/hr) and fig.6.80. different BER value for different rain rates (mm/hr).

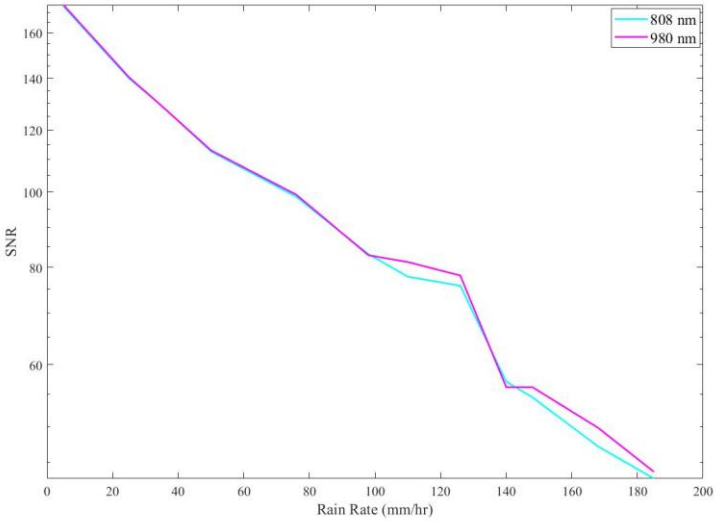

Fig.6.79. Different SNR value for different rain rates (mm/hr)

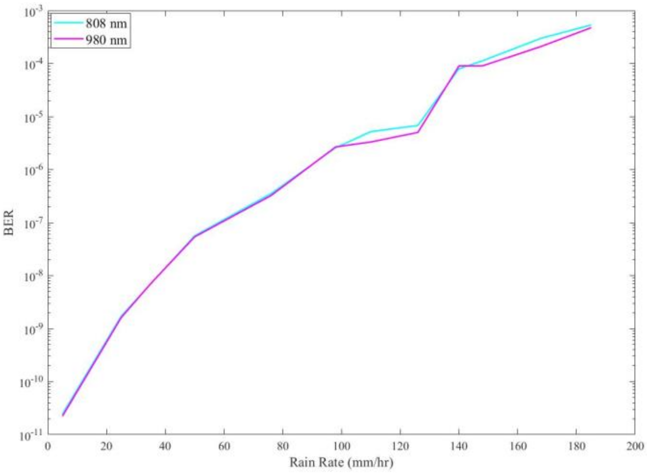

Fig.6.80. Different BER value for different rain rates (mm/hr)

Chapter 7 – MIMO Free-Space Optical Communication

7.1. Introduction

In order to transmit data, optical wireless communication uses light that travels through the atmosphere at distances ranging from a few metres (indoors) to a few kilometres (outdoor terrestrial) to hundreds of kilometres (space/satellite). Outdoor terrestrial/space applications, often known as free-space optical (FSO) communication, produce highly focused beams using infrared coherent sources (such as lasers) [78]. These beams are guided via a line-of-sight link using the appropriate optics in the direction of their intended use. Different impairments are experienced by the high-speed data-carrying optical beam as a result of atmospheric turbulence, misalignment, scattering, absorption, and diffraction. When there is bad weather and/or a lot of turbulence, the FSO channel that is affected by these factors performs erratically and unreliably.

Optical multiple-input multiple-output (MIMO) systems were largely influenced by recent successes of MIMO techniques in radio-frequency (RF) communication, where the use of multiple antennas increases the capacity of the wireless channel and/or improves the reliability of the wireless communication link. An optical MIMO system, as shown in fig.7.1, extends the spatial range of the FSO channel by using multiple transmit apertures (or optical sources) and multiple receive apertures (or photodetector arrays).

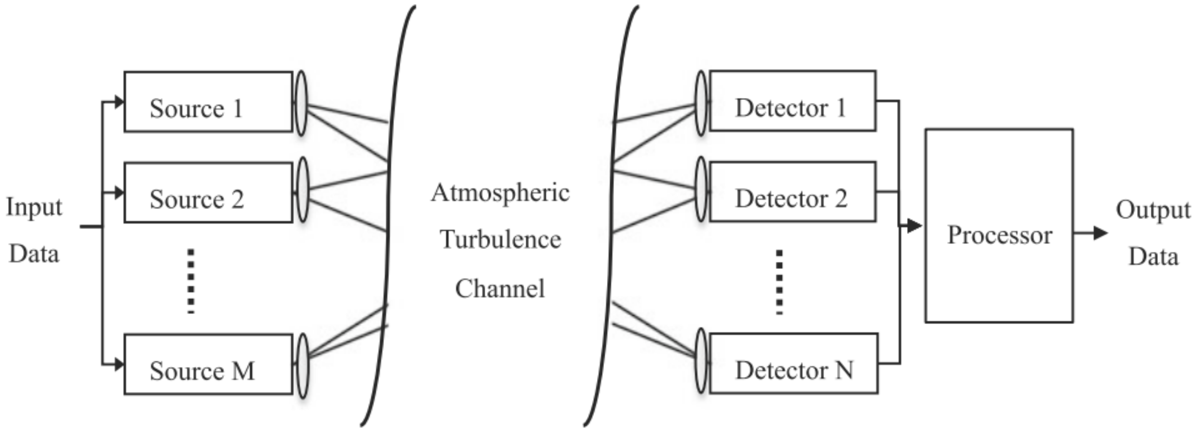

Fig.7.1. Optical wireless MIMO communication with M transmit apertures and N receive apertures

Studies that give asymptotic analysis and capacity bounds have looked at the MIMO FSO systems' capacity [79-81]. The effectiveness of FSO communication systems is greatly hampered by atmospheric turbulence. Fading, which is caused by distortions brought on by turbulence and can result in prolonged outages, especially on longer lines, is a variation in the received signal strength. Error-correcting codes [82,83], maximum-likelihood sequence estimation [87], and spatial diversity [85-93] are a few strategies that have been suggested in the literature to reduce the impacts of fading brought on by turbulence. Spatial diversity is a potent fading-mitigation method for FSO transmission that has been the focus of substantial research in the context of RF wireless communication. This chapter focuses on spatial diversity for MIMO FSO systems, noting that the fundamental difficulty in the design of FSO communication systems is the connection dependability.

Intensity modulation direct detection systems (IMDD), which have been the subject of literature on FSO communication, are taken into consideration throughout this chapter. The most widely used optical communication systems are IMDD systems, in which a photodetector can directly (i.e. incoherently) detect the data, which can only be modified on the intensity of the light (as opposed to phase or frequency). Thus, actual and positive signals are conveyed in IMDD systems.

7.2. Performance of MIMO FSO Systems

On-off keying (OOK) and pulse position modulation are two intensity modulation methods frequently used in Intensity Modulation Direct Detection (IMDD) communication systems (PPM). In comparison to binary PPM (BPPM), OOK offers superior spectrum efficiency, but it need threshold detection and hence CSI at the receiver. Repetition coding with BPPM signalling is taken into consideration in this case because, in contrast to the other approaches covered in the preceding section, it offers a straightforward yet effective transmission system. With the MIMO FSO method shown in Fig. 7.1., the source sends the intensity-modulated signal using repetition coding through M transmit apertures, and the destination node receives the fading signals using direct detection through N receive apertures. The outputs of the receive apertures are then combined by the destination node before decoding.

7.2.1. Average Error Rate

The average BER performance of MIMO FSO systems has been well researched in the literature for both Poisson and Gaussian noise models. Different modulation schemes and fading statistics have been taken into account while analysing the performance of various combining approaches like EGC. The size of the receive aperture in a single-aperture communication is the total of the areas of the N receive apertures, assuming that each laser has a power P=M. According to the Gaussian noise model, the average BER of the MIMO FSO system for EGC with binary signalling is started as,

$$P_e = \int_{\mathbf{h}} f_{\mathbf{h}}(\mathbf{h}) Q\left(\frac{\rho \mathrm{RPT}}{MN\sqrt{2NN_0}} \sum_{n=1}^{N} \sum_{m=1}^{M} h_{mn} \right) \mathbf{dh}$$

$$P_e = \int_{\mathbf{h}} f_{\mathbf{h}}(\mathbf{h}) Q\left(\frac{\rho \mathrm{RPT}}{2MN\sqrt{2N_0}} \sqrt{\sum_{n=1}^{N} \left(\sum_{m=1}^{M} h_{mn} \right)^2} \right) \mathbf{dh} \qquad (1)$$

where h_{mn} is the fading coefficient of each individual diversity path and $f_h(h)$ is the combined probability density function of the log-amplitude fading coefficients, which can be categorised as Gamma-Gamma. The output noise of the EGC combiner is N times more than that of a single-aperture system because it is assumed in the calculations that the thermal-noise-limited domain will exist, in which each of N receivers will produce the same amount of noise as a single receiver[94].It is determined by the formula $h_{mn} = h_a h_l$, where h_l is the route loss brought on by weather circumstances and ha is the turbulence fading coefficient approximated by the gamma-gamma distribution. The probability density function (pdf) for h_a is given as,

$$f_{ha}(h_a) = \frac{2(\alpha_1\beta_1)^{(\alpha_1+\beta_1/2)}}{\Gamma(\alpha_1)\Gamma(\beta_1)} ha^{(\alpha_1+\beta_1/2)-1} \qquad (2)$$

where the parameters α_1 and β_1 refer to the effective number of turbulent eddies on a large- and small-scale respectively, second-kind modified Bessel function. Taking into account a source with a tiny aperture, the propagating signal is described as a spherical wave [95]. In light of this, the values of α_1 and β_1 for a point receiver are provided by,

$$\alpha_1 = [\exp\{\frac{0{\cdot}49\beta_0^2}{\left(1+0{\cdot}56\beta_0^{12/5}\right)^{7/6}}\} - 1]^{-1} \qquad (3)$$

and

$$\beta_1 = [\exp\{\frac{0{\cdot}51\beta_0^2}{\left(1+0{\cdot}69\beta_0^{12/5}\right)^{5/6}}\} - 1]^{-1} \tag{4}$$

where, $\beta_0^2 = 0.5C_n^2k^{7/6}\ z^{11/6}$ is the spherical wave Rytov variance, $C_n^2 = 10^{-15}$the refractive index structure parameter and $k = 2\pi/\lambda$ the optical wave number.

The value of h_l is calculated by the Beer-Lambert's Law as [96]

$$h_l = e^{-\delta z} \tag{5}$$

where the attenuation coefficient δ, calculated using Kim's model [97], is, and z is the connection length. The link visibility V (the distance at which the picture contrast falls to 2% of what it would be if the item were nearby under other weather circumstances), the operating wavelength, and the particle size distribution q all affect the attenuation coefficient,

$$\delta = \left(\frac{17}{V}\right)\left(\frac{\lambda}{550}\right)^{-q} \tag{6}$$

The sum of gamma-gamma variables can be efficiently approximated as a gamma-gamma distribution [98] with parameters α_S and β_S given by,

$$\alpha_S = (S\alpha_1)+\varepsilon_S \tag{7}$$

and

$$\beta_S = S\beta_1 \tag{8}$$

where S = MN. The error term $\varepsilon_S$is approximated as

$$\varepsilon_s = (S-1)\left(\frac{-0.127-0.95\alpha_1-0.0058\beta_1}{1+0.00124\alpha_1+0.098\beta_1}\right) \tag{9}$$

The erfc(.) is expressed as a Meijer-G function to obtain as integrating using,

$$\text{BER} = A_o G_{5,2}^{2,4}\left(B_o \middle| \begin{matrix} \frac{1-\alpha_S}{2}, 1-\frac{\alpha_S}{2}, \frac{1-\beta_S}{2}, 1-\frac{\beta_S}{2}, 1 \\ 0, \frac{1}{2} \end{matrix}\right) \tag{10}$$

where,

$$A_0 = \frac{2^{\alpha_S+\beta_S}}{8\pi^{(3/2)}\Gamma(\alpha_S)\Gamma(\beta_S)} \tag{11}$$

and

$$B_0 = \left(\frac{8\gamma[h_l(MN)]^2}{(\alpha_S*\beta_S)^2}\right) \tag{12}$$

When a result, the benefit of EGC for a MIMO system with M = N grows extremely slowly and frequently remains small as more apertures are added. In [99], the BER performance of MIMO FSO systems in the presence of intense turbulence is investigated.

7.2.2. Diversity Gain

The traditional definition of diversity gain (or diversity order) is the negative asymptotic slope of the performance metric (for example, BER or outage probability) vs SNR on a log-log scale. The performance in log-normal fading channels shows a water-falling tendency, rendering the traditional notion of diversity gain meaningless for this kind of channel. This is due to the fact that the logarithm of the performance curves for log-normal FSO systems decays at high SNR with (log SNR)^2 rather than (log SNR). The diversity gain of log-normal fading channels was quantified as follows inas a means of addressing this problem.

$$D_R = \lim_{\mathrm{SNR}\to\infty} \frac{\partial \log P_{\mathrm{out}} / \partial \log \mathrm{SNR}}{\partial \log P_{\mathrm{out0}} / \partial \log \mathrm{SNR}} \tag{13}$$

where the comparative diversity gains between a benchmark scheme with an outage probability of P_{out0} and a MIMO system with an outage probability of P_{out} is determined. The relative diversity gains in (12) provides the same value as the standard definition of diversity gain first developed for Rayleigh fading channels [100] if the benchmark scheme is taken into account as the single-aperture transmission.

7.2.3. Aperture Averaging, Correlation and Near-Field Effects

In keeping with the simple assumptions, our study has thus far concentrated on the far-field regime, similar to the majority of the present work on MIMO FSO communication. However, these presumptions put restrictions on the geometry of the atmospheric optical connection (e.g., on the size of apertures and aperture separations) and may not adequately account for certain significant effects, such as aperture averaging, turbulence correlation, and any other near-field effects. In many real-world FSO applications, the system shape and parameters result in certain near-field effects, necessitating a more exact method for performance analysis.

When the impact of turbulence-induced fading correlation is taken into account, it is shown that the performance of FSO diversity systems can be severely diminished. To incorporate this impact into a far-field study, nevertheless, an ad hoc method was used. For instance, they presupposed knowledge of the correlation and their model was unable to relate the correlation effect to the physical characteristics of FSO systems. The effect of the spatial correlation of turbulence on the functionality of a multi-aperture FSO system was examined using more exact numerical modelling. For the spatial correlation coefficient in terms of propagation distance, a straightforward scaling algorithm is put forward. In addition, a decaying exponential function is used to quantitatively calculate the correlation coefficient as a function of transmitter separation. Although it takes into account the effects of spatial correlation, it ignores the effects of inter-beam interference by assuming that the optical power received from many beams is superimposed incoherently.

The findings are contrasted with those of the far-field study, which overestimates the BER of the diversity FSO system because it is unable to account for the considerable diversity gain of aperture averaging. Note that despite the fact that the far-field assumptions ignore the deteriorating effects of correlation and inter-beam interference, this overestimation still occurs. analyses a straightforward multiplexing system that uses a number of transmitter apertures and a number of reception detectors. The near-field study of such a system reveals inter-beam interference error floors in BER performance, which are disregarded by the far-field model.

It is generally known that, unlike their RF equivalents, single-aperture FSO communication systems may offer fading-mitigation capabilities through aperture averaging. Such devices offer an aperture average gain that gets better as the aperture area grows. However, by assuming that receiver apertures are modest, this impact has frequently been disregarded in the study of MIMO FSO systems.

Under thermal-noise-limited and background noise-limited regimes, the performance of a single-aperture FSO system and a multiple-aperture receive diversity FSO system based on EGC is evaluated. The aperture averaging effect has also been taken into consideration. The noise of an EGC receiver's output is believed to be equivalent to the noise of a single-aperture receiver with a similar field of view. The output noise of an EGC receiver is N times more than that of a single-aperture receiver, but, in a thermal noise-limited environment.

It has been demonstrated that under background-limited conditions, the multiple-aperture method consistently outperforms the single-aperture system, supposing that the total of the areas of the many apertures is equal to the area of a single aperture. The performance of large single apertures, however, can approach that of a multiple-aperture design under moderate turbulence. The multiple-aperture diversity methods, on the other hand, offer better diversity benefits in the thermal noise-limited domain, but since noise builds up in the EGC receiver, they can only outperform the single-aperture receivers at high SNR.

7.3. Result and Discussion

We calculate the effectiveness of a terrestrial FSO link with a link length z of 5 km, running at wavelengths of 808 nm and 980 nm with MIMO and aperture averaging under the influence of turbulence and different weather conditions. We have taken into account a gamma-gamma distribution-model mild turbulence regime in our study. $8.4 \mathrm{x} 10^{-15}$ $\mathrm{m}^{2/3}$ is used as the value of $C^2{}_n$ for moderate turbulence, and it also reflects an unusually high value of turbulence strength during the daytime close to the ground level [101-103]. Fog conditions can exist with low turbulence, but it is improbable that they would do so in conjunction with severe turbulence. This is because there is a significant inverse link between the strength of the turbulence and the attenuation induced by meteorological conditions. Thin fog conditions may exist simultaneously since in our study, a lower (moderate) turbulence regime has been represented. In MIMO spatial diversity approaches, the receivers must be separated by a distance bigger than the correlation length provided by $(\lambda z)^{0.5}$ in order for the channel gains to be statistically independent. Fig.7.2. shows the variation of BER against Visibility for various combinations of transmitter and receiver under MIMO schemes, the impact of meteorological conditions including very clear air, clear air/drizzle, haze, and thin fog as well as turbulence. No matter the weather, it can be shown that BER improves (decreases) as the number of transmit/receive apertures increases. In contrast to thin fog, the improvement in BER is more noticeable for extremely clear air, clear air/drizzle, and hazy conditions at lower levels of SNR. Given that fog circumstances result in the optical beam's maximum extinction, it is clear that the weather condition with the highest SNR is needed to achieve a given BER. When turbulence and meteorological circumstances such extremely clear air, clear air/drizzle, haze, and thin fog are simultaneously present, similar patterns are seen for the fluctuation in outage probability with the normalised outage threshold for various MIMO systems.

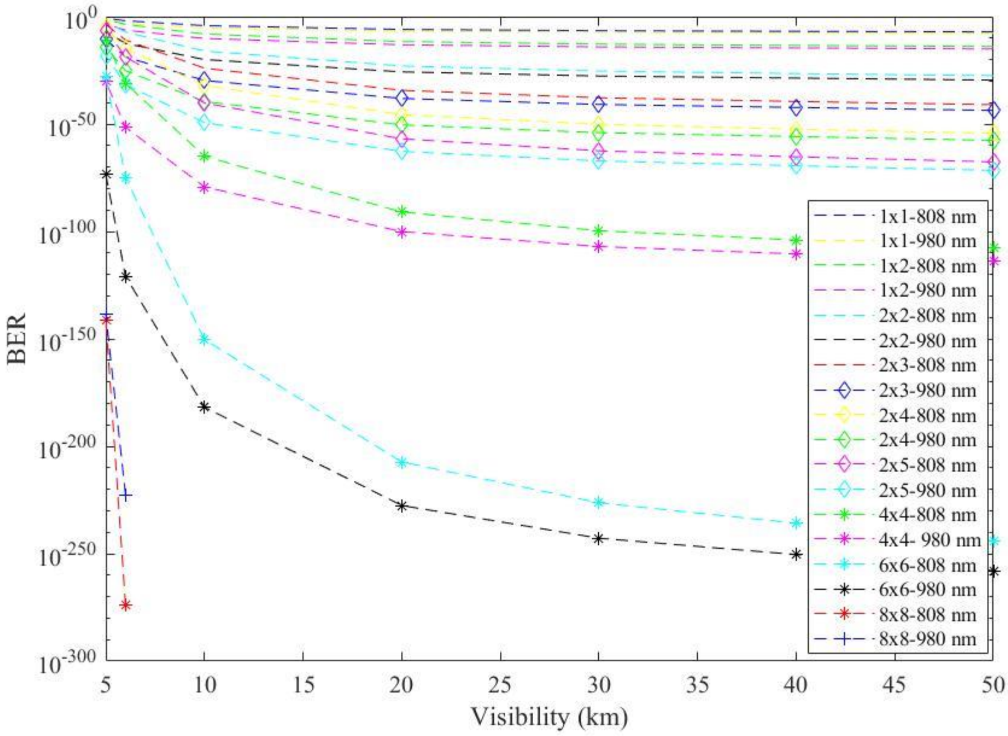

Fig.7.2. Various combinations of Transmitter and Receiver of BER over visibility for 808nm and 980nm Lasers

Another performance criterion for a spatial diversity system using MIMO techniques is diversity gain. It is described as the drop in SNR (in dB) that results from the use of a diversity scheme without any performance loss. The diversity gain is shown to rise as the number of transmit/receive apertures increases. However, regardless of the weather, with a set diversity scheme, the diversity gain is almost constant. This is because the loss brought on by the weather circumstances balances out in the computation of diversity gain and is independent of the quantity of transmit/receive apertures. Thus, despite the fact that the SNR requirement for achieving the same performance for a particular diversity scheme may be worse for fog followed by haze, clear air/drizzle, and the least being in extremely clear air, the diversity benefit stays essentially same.

Additionally, the impact of aperture averaging under various weather situations and turbulence is investigated. Plotting the receiver aperture diameter against the fluctuations in BER (at an SNR of 20 dB) is done. As aperture diameter increases, visibility also grows, whereas BER decreases. Because the rise in background noise places a physical limit on the aperture size, it cannot be extended forever. We have considered diameters upto 0.2 m since commercially available receivers have aperture diameters in the range of 0.25–0.2 m. The ability to achieve performance that may not be attainable with aperture averaging due to the aperture size limitation is found to rise when the number of transmit/receive apertures is increased. Fig.7.3. shows the variation of BER against visibility (km) graph for various diameter of transmitter. From the theoretical analysis it can be said that MIMO approach is much better than SISO approach on the basic of optical power attenuation.

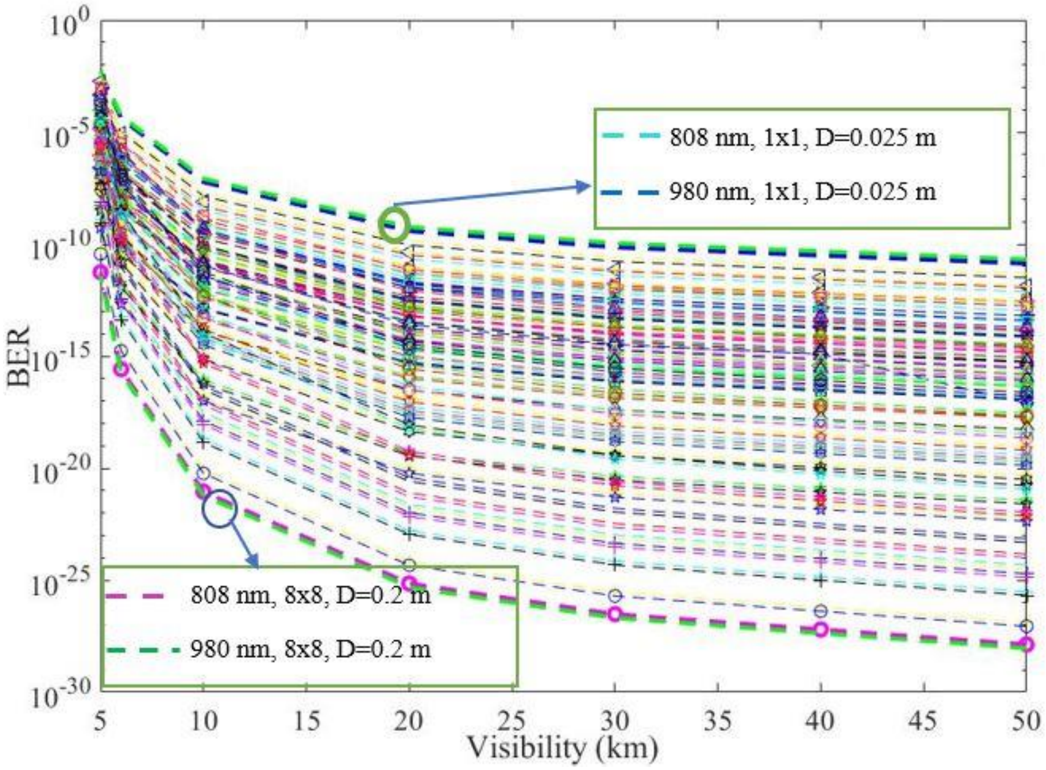

Fig.7.3. Variation of BER against visibility (km) for various diameter of transmitter

Chapter 8 – Conclusion and Future Scope

Free Space Optics (FSO) communication system has a lot of benefits over currently used methods, including optical, radio, and microwave ones. The primary benefits of an FSO system are lower setup costs and setup times. With a few adjustments, optical equipment may be used in an FSO system. The benefits of FSO communication systems and their potential applications make them a popular technology, although the medium's attenuation like fog, rain, temperature, snow etc. have significant drawbacks. FSO systems have various issues, such as attenuation in the medium, which might impair transmission efficiency because there will be power loss, data loss, etc. In this project work we are establish a optical wireless communication channel using different wavelength laser sources like visible wavelength lasers and near-infrared wavelength lasers. Data transmit channel at 5MHz channel frequency and transmit voice at 63 kHz channel frequency through the establish optical wireless communication channel. Testing of the created optical wireless communication channel in different atmospheric conditions like fog, rain and temperature. Evaluation as well as analyzation of the whole system by different communication parameters like Bit Error Rate (BER), optical power attenuation, Signal Noise Ratio (SNR) etc. Here the using lasers are worked with 532nm, 650nm, 808nm and 980nm lasers which are Diode Pump Solid State (DPSS) laser in nature. Among these four lasers 532nm and 650nm are visible wavelength lasers and 808nm and 980nm are near-infrared lasers. We used DPSS laser because this type of laser is easily available in the market and the cost of this type of laser is comparatively cheaper than other types of communication laser. When the high speed operation like Megahertz (MHz) range then DPSS laser used because of this type of laser effectively switches by the modulated signal.

An artificial experimental setup was constructed to examine the established optical wireless communication channel because the main objective of our experiment is to determine how well our established OWC channel performs in the different atmospheric erosion. For that purpose, designed artificial simulation setup of fog, rain and temperature. As the result of our rain artificial experimental setup, from this experiment obtained different rain rates and from these understand how the established OWC channel is behaving at different rain rates. In this experiment, the minimum rain rate is 5 mm/hr and maximum rain rate is 125 mm/hr. For temperature, the scintillation varies between 10^{-15} to 10^{-12} during our experiment where 10^{-15} is the minimum and 10^{-12} is the maximum. Four wavelength lasers have been used on this project, two of these are visible wavelengths (532nm and 650nm) and the other two wavelengths are near-infrared (808nm and 980nm). That's why visible wavelength and near-infrared wavelength are compared differently. It is found that in the case of visible wavelength, for temperature and fog result of the 650nm wavelength laser is better than 520nm wavelength laser. For the near-infrared wavelength, temperature and fog result of the 980nm wavelength laser is better than 808nm wavelength laser. No such difference was observed during the rain experiment in both visible and near-infrared wavelengths. The four wavelengths could not be compared together due to lack of suitable photodetector. From the experiment, it has been shown that the atmospheric effect on OWC channel is different like in case of rain simulation, the attenuation of the optical link is wavelength independent whereas attenuation for fog simulation and temperature simulation are wavelength dependent.

Wavelength diversity is an effective way to mitigate the atmospheric effect on OWC link. To achieve this, higher wavelength like 1550 nm or higher wavelengths may be used. Different modulation technique apart from amplitude modulation (OOK), like Frequency Shift Keying, Phase shift Keying etc. may be used for mitigate the atmospheric effect. Different diversity technique like SIMO, MIMO, aperture diversity, etc. is incorporated in the system to improve the signal fidelity of the system, it has been seen that theoretically, it is worked better than SISO system.

Data is transmitted over long distances using FSO communication systems using light that has long-distance attenuation. The optical beam is subjected to various impairments during propagation due to atmospheric turbulence, diffraction, scattering, and absorption. In bad weather and/or situations with a lot of turbulence, the FSO channel that is affected by these factors acts erratically and inconsistently. Techniques for spatial variety have been suggested as a way to provide redundancy while still improving the dependability of turbulent FSO channels. To create MIMO FSO systems with multiple parallel diversity routes via which multiple copies of data may be delivered at once, a number of transmit/receive apertures are used in conjunction with each other. To offer diversity gain and mitigate atmospheric degradations in FSO channels, distributed MIMO and relaying methods may also be deployed. The success of MIMO RF communication in recent years served as a major inspiration for the use of MIMO methods in FSO systems. The use of MIMO methods in these two technologies differs fundamentally from one another, though. First, transmit diversity gain in FSO systems may be achieved without space-time coding. As long as the aperture is big enough, FSO systems with a single receive would likewise benefit from diversity gain. The use of relays in serial rather than in parallel can yield larger diversity gains in a distributed MIMO FSO system. When designing MIMO FSO systems, all of these variations must be carefully considered. The majority of recent studies has used simpler channel models to analyse MIMO FSO communication. Therefore, additional investigation is necessary to effectively design MIMO FSO systems while taking into consideration more precise models that account for correlation, aperture averaging, and near-field effects.

REFERENCE

[1] Osseiran, A. Boccardi, F. Barun, V. Kusume, K. Marsch, P. Maternia, M. Queseth, O. Schellmann, M. Schotten, H. H. Tullberg, H. Uusitalo, M. Timus, B. Fallgren, M.: scenarios for 5G mobile and wireless communications: the vision of the METIS project. IEEE Commun. Mag. 52(5), 26-35 (2014)

[2] Jungnickel, V. Manolakis, K. Zirwas, W. Panzner, B. Sternad, M. Svensson, T.: The role of small cells, coordinated multi-point and massive MIMO in 5G. IEEE Commun. Mag. 52(5), 44-21 (2014)

[3] Rappaport, T.S. Sun, S. Mayzus, R. Zhao, H. Azar, Y. Wang, K. Wong, G.N. Schulz, J.K. Sammi, M. Guiterrez, F.: Millimeter wave mobile communications for 5G cellular: it will work. IEEE Access 1, 335-349 (2013)

[4] Etkin, R. Parekh, A. Tse, D.: Spectrum sharing for unlicensed bands. IEEE J. Sel. Areas Commun. 25(3), 517-528 (2007)

[5] Arnon, S. Barry, J.R. Karagiannidis, G.K. Schober, R.Uysal, M. (eds.): Advanced Optical Wireless Communication. Cambridge University Press (2012)

[6] Ghassemlooy, Z. Popoola, W.O. Rajbhandari, S.: Optical Wireless Communications – System and Channel Modelling with Matlab. CRC publish, USA (2012)

[7] Tsukamoto, K. Hashimoto, A. Aburakawa, Y. Matsumoto, M.: The case for free space. IEEE Microw. Mag. 10, 84-92 (2009)

[8] Arimoto, Y.: Compact free-space optical terminal for terminal for mulyi-gigabit signal transmissions with a single-mode fiber. In: Proceedings of SPIE, Free-Space Laser Communication Technologies, vol. XXI, pp. 719908(1)-(9) (2009)

[9] Nakajima, A. Sako, N. Kamemura, M. Wakayama, Y. Fukuzawa, A. Sugiyama, H. Okada, N.: A visible light communication experimental micro-satellite. In. Proceedings of the International Conference on Space Optical Systems and Application (ICSOS) 2012, 12-1. Ajaccio, Corsica, France, October 9-12 2012

[10] Eswaravaka Mahesh Reddy, A. Brintha Therese, Analysis of Atmospheric Effects on Free Space Optical Communication, IEEE, 2017

[11] Abu Bakar Mohammad, Optimization of FSO System in Tropical Weather using Multiple Beams, Proc. Of 2014 IEEE 5th International Conference on Photonics (ICP), Kuala Lumpur, 2-4 Sept. (2014)

[12] Maged Abdullah Esmail, Habib Fathallah, Mohamed-Slim Alouimi, Outdoor FSO Communication Under Fog: Attenuation Modeling and Performance Evaluation, IEEE Photonics Journal, 2016

[13] Yamac Dikmelik, Jacob B. Khurgin, Matthew D. Escarra, Peter Q. Liu, Anthony J. Hoffman, Kale J. Franz, Claire F. Gmachl, Jenyu Fan and Xiaojun wang, IEEE (2009)

[14] Martin Grabner, Vaclav Kvicera, Multiple Scattering in Rain and Fog on Free-Space Optical Links Vol. 32, IEEE, 2014

[15] Milica I. PETKOVIC, Goran T. DORDEVIC, Dejan N. Milic, BER Performance of IM/DD FSO System with OOK using APD Receiver, Aleksandra Medvedeva 14, 18000 Nis, Serbia, IEEE, 2016

[16] Dhanya Devarajan, Dr. Sakuntala, S. Pillai, Optimization of Laser Satellite Communication Syatem through Link (2010)

[17] T. Tolker-Nielsen and G. Oppenhauser, “In-orbit test result of an operational intersatellite link between ARTEMIS and SPOT 4,” in Proc. SPIE, Free-Space Laser Commun. Technol. XIV, San Jose, CA, USA, Jan. 2002, vol. 4639, pp. 1–15.

[18] R. Lange, B. Smutny, B. Wandernoth, R. Czichy, and D. Giggenbach, “142 km, 5.625 Gb/s free-space optical link based on homodyne BPSK modulation,” in Proc. SPIE, Free-Space Laser Commun. Technol. XVIII, 2006, vol. 6105, p. 61050A.

[19] B. Smutny et al., “5.6 Gbps optical intersatellite communication link,” in Proc. SPIE, Free-Space Laser Commun. Technol. XVIII, Feb. 2009, vol. 7199, p. 719 906.

[20] N. Karafolas and S. Baroni, “Optical satellite networks,” J. Lightw. Technol., vol. 18, no. 12, pp. 1792–1806, Dec. 2000.

[21] H. Hemmati, Deep Space Optical Communications. Hoboken, NJ, USA: Wiley-Interscience, 2006.

[22] F. E. Goodwin, “A review of operational laser communication systems,” Proc. IEEE, vol. 58, no. 10, pp. 1746–1752, Oct. 1970.

[23] Ghassemlooy, Z. and Popoola, W.O. , “Terrestrial Free-Space Optical Communications”, Optical communications research group, NCR Lab, Northumbria University, Newcastle upon Tyne, UK.

[24] C. Kachris and I. Tomkos, “A survey on optical interconnects for data centers,” IEEE Commun. Surveys Tuts., vol. 14, no. 4, pp. 1021–1036, Oct. 2012.

[25] F. Hanson and S. Radic, “High bandwidth underwater optical communication,” Appl. Opt., vol. 47, no. 2, pp. 277–283, Jan. 2008.

[26] S. Lee, J. K. Kwon, S.-Y. Jung, and Y.-H. Kwon, “Evaluation of visible light communication channel delay profiles for automotive applications,” EURASIP J. Wireless Commun. Netw., vol. 2012, no. 1, pp. 370:1–370:8, Dec. 2012.

[27] V. W. S. Chan, “Optical satellite networks,” J. Lightw. Technol., vol. 21, no. 11, pp. 2811–2827, Nov. 2003.

[28] Bohren, Craig F.; Donald R. Huffman (1983). Absorption and Scattering of Light by Small Particles. Wiley. ISBN 0-471-29340-7.

[29] Colton, David; Rainer Press (1998). Inverse Acoustic and Electromagnetic Scattering Theory. Springer. ISBN 978-0-8194-1924-7.

[30] V. W. S. Chan, “Free-space optical communications,” J. Lightw. Technol., vol. 24, no. 12, pp. 4750–4762, Dec. 2006.

[31] K. Majumdar and J. C. Ricklin, Free-Space Laser Communications: Principles and Advances. New York, NY, USA: Springer-Verlag,Dec. 2010.

[32] H. Yuksel, S. Milner, and C. C. Davis, “Aperture averaging for optimizing receiver design and system performance on free-space optical communication links,” J. Opt. Netw., vol. 4, no. 8, pp. 462–475, Aug. 2005.

[33] C. Z. Çil, Y. Baykal, H. T. Eyyuboˇglu, and Y. Cai, “Beam wander characteristics of cos and cosh-Gaussian beams,” Appl. Phys. B, vol. 95, no. 4, pp. 763–771, Jun. 2009.

[34] Y. Ren, A. Dang, B. Luo, and H. Guo, “Capacities for long-distance freespace optical links under beam wander effects,” IEEE Photon. Technol. Lett., vol. 22, no. 14, pp. 1069–1071, Jul. 2010.

[35] S. Arnon, “Effects of atmospheric turbulence and building sway on optical wireless communication systems,” Opt. Lett., vol. 28, no. 2, pp. 129– 131, Jan. 2003.

[36] H. Willebrand and B. S. Ghuman, Free Space Optics: Enabling Optical Connectivity in Today’s Networks. Indianapolis, IN, USA: Sams, 2001.

[37] I. Kim, B. McArthur, and E. Korevaar, “Comparison of laser beam propagation at 785 nm and 1550 nm in fog and haze for optical wireless communications,” in Proc. SPIE, Opt. Wireless Commun. III, Boston, MA, USA, Nov. 2001, vol. 4214, pp. 26–37.

[38] M. Grabner and V. Kvicera, “The wavelength dependent model of extinction in fog and haze for free space optical communication,” Opt. Exp., vol. 19, no. 4, pp. 3379–3386, Feb. 2011.

[39] H. Weichel, Laser Beam Propagation in the Atmosphere, SPIE, Bellingham WA, 1990.

[40] J. M. Wallace and P. V. Hobbs, Atmospheric Science: An Introductory Survey, Academic Press, Orlando, 1977.

[41] W. K. Pratt, Laser Communication Systems, J. Wiley & Sons, New York, 1969.

[42] M. Aharonovich and S. Arnon, “Performance improvement of optical wireless communication through fog with a decision feedback equalizer,” J. Opt. Soc. Amer. A, Opt. Image Sci., vol. 22, no. 8, pp. 1646– 1654, Aug. 2005.

[43] M. Grabner and V. Kvicera, “Multiple scattering in rain and fog on freespace optical links,” J. Lightw. Technol., vol. 32, no. 3, pp. 513–520, Feb. 2014.

[44] L. C. Andrews and R. L. Phillips, Laser Beam Propagation Through Random Media, 2nd ed. Bellingham, WA, USA: SPIE, 2005.

[45] L. C. Andrews, R. L. Phillips, C. Y. Hopen, and M. A. Al-Habash, “Theory of optical scintillation,” J. Opt. Soc. Amer. A, Opt. Image Sci., vol. 16, no. 6, pp. 1417–1429, Jun. 1999.

[46] L. C. Andrews, R. L. Phillips, and C. Y. Hopen, Laser Beam Scintillation with Applications. Bellingham, WA, USA: SPIE, 2001.

[47] Ghassemlooy, Z. and Popoola, W.O. , “Terrestrial Free-Space Optical Communications”, Optical communications research group, NCR Lab, Northumbria University, Newcastle upon Tyne, UK.

[48] A. K. Majumdar and J. C. Riclkin, *Free-Space Laser Communications: Principles And Advances*. New York, NY, USA: Springer-Verlag, 2007.

[49] A. K. Majumdar and J. C. Ricklin, *Free-Space Laser Communications: Principles and Advances*. New York, NY, USA: Springer-Verlag, Dec. 2010.

[50] Garg Nitin, Singh Vivek, “Free Space optical communication link using optical Mach-Zehnder modulator and analysis at different parameters”, ICICT, IEEE conference, pp 192-195, 2014.

[51] http://www.laseroptronics.com/index.cfm/id/57-66.htm.

[52] A. K. Rahman, M. S. Anuar, S. A. Aljunid, and M. N. Junita,“Study of rain attenuation consequence in free space optic transmission,” in Proceedings of the 2ndMalaysia Conference on Photonics Telecommunication Technologies (NCTT-MCP ’08), pp. 64–70, IEEE, Putrajaya, Malaysia, August 2008.

[53] S. A. Al-Gailani, A. B. Mohammad, and R. Q. Shaddad, “Enhancement of free space optical link in heavy rain attenuation using multiple beam concept,” *Optik*, vol. 124, no. 21, pp.4798–4801, 2013.

[54] M. Ijaz, Z. Ghassemlooy, J. Pesek, O. Fiser, H. Le Minh, and E. Bentley, “Modeling of fog and smoke attenuation in free space optical communications link under controlled laboratory conditions,” *Journal of Lightwave Technology*, vol. 31, no. 11, Article ID 6497447, pp. 1720–1726, 2013.

[55] Z. Ghassemlooy, J. Perez, and E. Leitgeb, “On the performance of FSO communications links under sandstorm conditions,” in *Proceedings of the 12th International Conference on Telecommunications (ConTEL ’13)*, pp. 53–58, IEEE, Zagreb, Croatia, June 2013.

[56] K. Rammprasath and S. Prince, “Analyzing the cloud attenuation on the performance of free space optical communication,” in *Proceedings of the 2nd International Conference on Communication and Signal Processing (ICCSP ’13)*, pp. 791–794, Melmaruvathur, India, April 2013.

[57] S. A. Al-Gailani, A. B. Mohammad, R. Q. Shaddad, and M. Y. Jamaludin, “Single andmultiple transceiver simulationmodules for free-space optical channel in tropical malaysian weather,” in *Proceedings of the IEEE Business Engineering and Industrial Applications Colloquium (BEIAC ’13)*, pp. 613–616, Langkawi, Malaysia, April 2013.

[58] H. A. Fadhil, A. Amphawan, H. A. B. Shamsuddin et al., “Optimization of free space optics parameters: an optimum solution for bad weather conditions,” *Optik*, vol. 124, no. 19, pp.3969–3973, 2013.

[59] D.O. Caplan, M.L. Stevens, and D.M. Boroson, "Variable-rate communication system with optimal filtering," in US Pat. 6,694,104, 2004, (filed 1998).

[60] D.O. Caplan, M.L. Stevens, D.M. Boroson, and J.E. Kaufmann, "A multi-rate optical communications architecture with high sensitivity," in LEOS, 1999.

[61] M.L. Stevens, D.M. Boroson, and D.O. Caplan, "A novel variable-rate pulse-position modulation system with near quantum limited performance," in LEOS, 1999.

[62] D.O. Caplan and WA. Atia, "A quantum-limited optically-matched communication link," in Optical Fiber Conference (OFC), 2001.

[63] D.O. Caplan and W.A. Atia, "Methods of achieving optimal communications performance," in US Pat. 7,181,097, 2007.

[64] D.O. Caplan, B.S. Robinson, R.J. Murphy, and M.L. Stevens, "Demonstration of 2.5-Gslotls optically-preamplifier M-PPM with 4 photons/bit receiver sensitivity," in Optical Fiber Conference (OFC): Paper PDP23, 2005.

[65] A Comparison of FSO Wavelength System Designs, LightPointe White Paper, 2002. [Online]. Available: http://www.lightpointe.com/support/ whitepapers.html

[66] H. Manor and S. Arnon, “Performance of an optical wireless communication system as a function of wavelength,” *Appl. Opt.*, vol. 42, no. 21, pp. 4285–4294, Jul. 2003.

[67] Z. Xu and B. M. Sadler, “Ultraviolet communications: Potential and state-of-the-art,” *IEEE Commun. Mag.*, vol. 46, no. 5, pp. 67–73, May 2008.

[68] “Free Space optical communication”. Hemani Kaushal, V.K.Jain and Subrat Kar. Springer.

[69] Sanjib Kumar Mandal, Bholanath Bera and G.G. Dutta, “Free Space Optical (FSO) Communication Link Design Under Adverse Weather Condition”, IEEE 2020, International Conference on Computer, Electrical & Communication Engineering (ICCECE).

[70] B.L. Edwards, et. al., "Overview of the Mars laser communications demonstration project," in American Institute of Aeronautics and Astronautics, Space 2003 Conference & Exposition,2003.

[71] S.A. Townes, et. al., "The Mars laser communication demonstration," presented at IEEE Aerospace Conf., 2004.

[72] D.O. Caplan, M.L. Stevens, and D.M. Boroson, "Variable-rate communication system with optimal filtering," in US Pat. 6,694,104, 2004, (filed 1998).

[73] D.O. Caplan, M.L. Stevens, D.M. Boroson, and J.E. Kaufmann, "A multi-rate optical communications architecture with high sensitivity," in LEOS, 1999.

[74] M.L. Stevens, D.M. Boroson, and D.O. Caplan, "A novel variable-rate pulse-position modulation system with near quantum limited performance," in LEOS, 1999.

[75] D.O. Caplan and WA. Atia, "A quantum-limited optically-matched communication link," in Optical Fiber Conference (OFC), 2001.

[76] D.O. Caplan and W.A. Atia, "Methods of achieving optimal communications performance," in US Pat. 7,181,097, 2007.

[77] D.O. Caplan, B.S. Robinson, R.J. Murphy, and M.L. Stevens, "Demonstration of2.5-Gslotls optically-preamplifier M-PPM with 4 photons/bit receiver sensitivity," in Optical Fiber Conference (OFC): Paper PDP23, 2005.

[78] Khalighi, M.A., Uysal, M.: Survey on free space optical communication: a communication theory perspective. IEEE Commun. Surveys Tuts. 16, 2231–2258 (2014)

[79] Haas, S.M., Shapiro, J.H.: Capacity of wireless optical communications. IEEE J. Sel. Areas Commun. 21, 1346–1357 (2003)

[80] Haas, S.M.: Capacity of and coding for multiple-aperture wireless optical communications. Ph.D. Dissertation, Massachusetts Institute of Technology (2003)

[81] Chakraborty, K., Dey, S., Franceschetti, M.: Outage capacity of the MIMO poisson fading channels. IEEE Trans. Info. Theory 54, 4887–4907 (2008)

[82] Zhu, X., Kahn, J.M.: Performance bounds for coded free-space optical communications through atmospheric turbulence channels. IEEE Trans. Commun. 51, 1233–1239 (2003)

[83] Uysal, M., Navidpour, S.M., Li, J.: Error rate performance of coded free-space optical links over strong turbulence channels. IEEE Commun. Lett. 8, 635–637 (2004)

[84] Zhu, X., Kahn, J.M.: Markov chain model in maximum-likelihood sequence detection for free-space optical communication through atmospheric turbulence channels. IEEE Trans. Commun. 51, 509–516 (2003)

[85] Wilson, S.G., Brandt-Pearce, M., Qianling, C., Leveque, J.H.: Free-space optical MIMO transmission with Q-ary PPM. IEEE Trans. Commun. 53, 1402–1412 (2005)

[86] Wilson, S.G., Brandt-Pearce, M., Cao, Q., Baedke, M.: Optical repetition MIMO transmission with multipulse PPM. IEEE J. Sel. Areas Commun. 23, 1901–1909 (2005)

[87] Razavi, M., Shapiro, J.H.: Wireless optical communications via diversity reception and optical preamplification. IEEE Trans. Wireless Commun. 4, 975–983 (2005)

[88] Lee, E., Chan, V.: Part 1: optical communication over the clear turbulent atmospheric channel using diversity. IEEE J. Sel. Areas Commun. 22, 1896–1906 (2004)

[89] Navidpour, S.M., Uysal, M., Kavehrad, M.: BER performance of free-space optical transmission with spatial diversity. IEEE Trans. Wireless Commun. 6, 2813–2819 (2007)

[90] Safari, M., Uysal, M.: Do we really need OSTBC for free-space optical communication with direct detection? IEEE Trans. Wireless Commun. 7, 4445–4448 (2008)

[91] Tsiftsis, T.A., Sandalidis, H.G., Karagiannidis, G.K., Uysal, M.: Optical wireless links with spatial diversity over strong atmospheric turbulence channels. IEEE Trans. Wireless Commun. 8, 951–957 (2009)

[92] Bayaki, E., Schober, R., Mallik, R.K.: Performance analysis of MIMO free-space optical systems in gamma-gamma fading. IEEE Trans. Commun. 57, 3415–3424 (2009)

[93] Safari, M., Hranilovic, S.: Diversity and multiplexing for near-field atmospheric optical communication. IEEE Trans. Commun. 61, 1988–1997 (2013)

[94] Fenton LF (1960) The sum of lognormal probability distributions in scatter transmission systems. IRE Trans. Commun. COM-8:57–67

[95] Andrews, L.C., Phillips, R.L., Hopen, C.Y.: ‘Laser beam scintillation with applications’ (SPIE Press, 2001)

[96] Naboulsi, M.A., Sizun, H., Fornel, F.: ‘Fog attenuation prediction for optical and infrared waves’, Opt. Eng., 2004, 43, (2), pp. 319–329

[97] Ghassemlooy, Z., Popoola, W., Rajbhandari, S.: ‘Optical wireless communication’ (CRC Press, 2012)

[98] Chatzidiamantis, N.D., Karagiannidis, G.K., Michalopoulos, D.S.: ‘On the distribution of the sum of gamma-gamma variates and application in MIMO optical wireless systems’. Proc. IEEE Global Telecommunications Conf. (GLOBECOM), Hawaii, USA, 30 November–4 December 2009, pp. 1–6

[99] Gappmair, W., Hranilovic, S., Leitgeb, E.: ‘Performance of PPM on terrestrial FSO links with turbulence and pointing errors’, IEEE Commun. Lett., 2010, 14, (5), pp. 468–470

[100] Safari, M., Uysal, M.: Cooperative diversity over log-normal fading channels: performance analysis and optimization. IEEE Trans. Wirel. Commun. 7, 1963–1972 (2008)

[101] Majumdar, A.K., Riclkin, J.C.:‘Free-space laser communications: principles andadvances’(Springer-Verlag, 2007)

[102] hassemlooy, Z., Popoola, W., Rajbhandari, S.:‘Optical wireless communication’(CRC Press, 2012)

[103] Uysal, M., Li, J., Yu, M.:‘Error rate performance analysis of coded free-spaceoptical links over gamma-gamma atmospheric turbulence channels’,IEEE Trans.Wirel. Commun., 2006,5, (6), pp. 1229–1233

Appendix A

Instruments used for Data and Voice communication under different atmospheric conditions.

A.1. 33600A Series Trueform Waveform Generators (AWG)

- Easily generate the full range of signals you need for the most demanding measurements
- Test your devices with confidence that the waveform generator is outputting the signals you expect
- Select just the capabilities you need now, then upgrade easily when your needs change

Fig.1. Front view of AWG

Table.1. Features of 33600A Series Trueform Waveform Generators (AWG)

100 MHz PULSE	High-bandwidth pulse, 100 MHz, DDS pulse limited to 50 MHz Set leading and trailing edge times independently
PRBS Patterns	Provides standard PRBS patterns, PN3 through PN32 Select PN type, set bit rate, set edge times
2-Channel Coupling	Dual-channel coupling, frequency and amplitude, and tracking Set start phase for each channel, phase shift between channels
Combining Signals	Sum two signals together, frequency and amplitude independent 2-tone (4-tone on 2-ch), square-sine, noise on pulse, and others
Trueform Arbs	Create up to 4 million samples standard, 64 million optional Connect arb segments together, with up to 512 segments
Low Voltage Settings	Lower voltage range at 1 mVpp, DDS is only 10 mVpp Set high and low voltage limits to prevent overload on DUT
Band-Limited Noise	Adjust bandwidth to concentrate the energy of the noise Noise source goes to full 120 MHz bandwidth

A.2. D C Power Supply – GPD 4303S

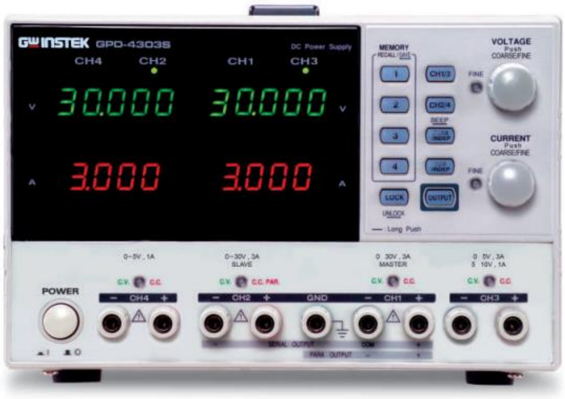

Fig.2. Front view of DC Power Supply

Features of D C Power Supply – GPD 4303S

- 2,3,and 4 Independent Isolated Output
- Digital Panel Control (Rotary Encoder Switch, Rubber Key With Indicator)
- User-Friendly Operation, Coarse / Fine Volume Control
- 4 Sets Save / Recall
- PC Software & USB Driver
- The tracking series and parallel mode can be selected with a single touch
- Indicators embedded in the keys provide an instant view of the power supply status; the Key Lock feature prevents improper operation
- Smart cooling fan control offers a well-balanced cooling mechanism, ensuring quiet operation

A.3. Keysight Infiniium S-Series Mixed Signal Oscilloscope – MSOS054A

Table.2. Specification of Keysight Infiniium S-Series Mixed Signal Oscilloscope – MSOS054A

Bandwidth	500 MHz – 8 GHz
Optimized for	Signal integrity
Max memory (2 ch)	820 Mpts
ADC Bits	10
Inputs	50 Ω, 1 MΩ
Operating System	Windows 10
Hard drive	256 GB Removable SSD
Motherboard	Quad core i5, 8 GB RAM
Data offload	USB 3.0, 1000BASE-T LAN

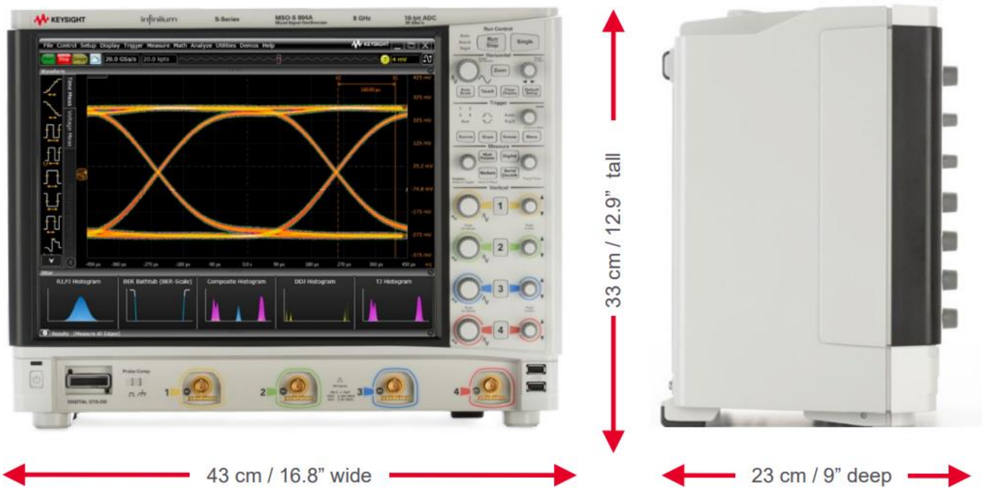

Fig.3 Front and Side view of MSO

Table.3. Features of Keysight Infiniium S-Series Mixed Signal Oscilloscope – MSOS054A

Bandwidth (-3 dB)	50 Ω - 500 MHz
	1 MΩ - 500 MHz
Vertical Resolution	10 bits, up to 16 bits with high-resolution mode
Typical rise/fall time	10/90% - 860 ps
	20/80% - 620 ps
Input Impedance	50 Ω ± 3.5% (typically +1% at 25 °C)
Input Sensitivity	1 MΩ: 1 mV/div to 5 V/div
Input Coupling	50 Ω : DC
Bandwidth Limit Filters	Digital: 18.3 MHz up to scope bandwidth, in increments of 100 kHz (under 1 GHz) or 10 MHz (1 GHz and above). Filter options: Brick Wall, 4th Order Bessel, or Bandpass
Channel-to-channel Isolation	100 MHz to 1 GHz: 40 dB
DC gain accuracy	± 2% full scale (± 1% typical)
Max input voltage	1 MΩ: 30 V_{RMS} or ± 40 V_{MAX} (DC+V_{PEAK}). Probing technology allows for testing of higher voltages; the included N2873A 10:1 probe supports 300 V_{RMS} or ± 400 V_{MAX} (DC+V_{PEAK}).
Offset range	1 MΩ
Offset accuracy	≤ 2 V: ± 0.1 div ± 2 mV ± 1%
Dynamic range	+4 divisions from centre screen
DC voltage measurement accuracy	Dual cursor: ± [(DC gain accuracy) + (resolution)]
	Single cursor: ± [(DC gain accuracy) + (offset accuracy) + (resolution/2)]

A.4. Ophir Vega Laser Power Meter (7Z01560) & Sensor (3A-P-THz)

Fig.4. Front and back view of laser power meter 7Z01560

Table.4. Specifications of Ophir Vega Laser Power Meter

Power Meter Features	Brilliant color TFT 320 x 240 pixel graphics LCD. Large 16mm digits. High resolution analog needle also can be chosen. Many screen features including power with multicolor bar graph, energy, average, exposure, frequency, graphs, scaling, special units, and more. Complete on line context sensitive help screens.
Outputs	USB, RS232 and user selectable 1, 2, 5 and 10 Volt full scale analog output.
Screen Refresh	15 times/sec
Case	Molded high impact plastic with optimized angle two level kickstand. Rubberized sides for easy grip and protection against damage.
Size	Folds to a compact 210mm L x 109mm W x 36mm H
Battery	Rechargeable NiMH batteries with typically 18 hours between charges. The charger can be ordered from your local distributor. The charger also functions as an AC adapter.
Data Handling	Data can be viewed on board or transmitted to pc: On Board: Non-volatile storage of up to 250,000 data points in up to 10 files. Max onboard data logging rate 4000 points/s and Max data logging rate to the PC 2000 points/s.
Sensor Features	Works with Thermopile, Beam Track, Pyroelectric (PE-C series) and Photodiode sensors.
Program Features	Preferred start up configuration can be set by user. User can recalibrate power, energy, response time and zero offset.
Compliance	CE, UKCA, China RoHS

Fig.6 shows front view of 3A-P-THz High Sensitivity Thermal Sensors.

Fig.6. 3A-P-THz High Sensitivity Thermal Sensors

Table.5. Specifications of 3A-P-THz High Sensitivity Thermal Sensors

Absorber Type	P type
Spectral Range µm	0.1THz - 30THz
Aperture mm	Ø12mm
Maximum Beam Divergence	NA
Power Mode	
Power Range	15µW - 3W
Power Scales	3W to 300µW
Power Noise Level	4µW
Thermal Drift (30min)	5 - 30µW
Maximum Average Power Density kW/cm2	0.05
Response Time with Meter (0-95%) typ. s	2.5
Calibration Uncertainty ±%	1.9
Power Accuracy ±%	8
Linearity with Power ±%	1
Energy Mode	
Energy Range	20µJ - 2J
Energy Scales	2J to 200µJ
Minimum Energy	20µJ
Maximum Energy Density J/cm2	
<100ns	1
0.5ms	1
2ms	1
10ms	1
Cooling	Convection
Weight kg	0.2
Fiber Adapters Available	ST, FC, SMA, SC
Compliance	CE, UKCA, China RoHS

A.5. Diode Pumped Solid State (DPSS) LASER

Fig.8. DPSS LASERs

Table.6. DPSS LASERs Technical Specification

Wavelength Range	± 1nm
Stability (RMS)	5% standard
	3% and 1% optional
Optical Noise	Standard 10%
	Low noise version at 1% optional
Laser Spectrum Width	0.2nm
Beam Diameter (Transverse Mode – TEM00)	1.2mm
Beam Diameter (Transverse Mode – nearTEM00)	3-4mm
Beam Divergence (Transverse Mode – TEM00)	<0.7mrad
Beam Divergence (Transverse Mode – nearTEM00)	<2mrad
Polarization Ratio	100:1
Pointing Stability	<0.05
Modulation	TTL or Analog, 300kHz – 5MHz
Warm Up Time	10 minutes
Operational Temperature range	10°C - 35°C
Power Supply	90 – 260VAC
Life Time	10,000 Hours

A.6. UltraSonic Nebulizer WH2000

Fig.9. Front view of UtraSonic Nebulizer WH-2000

Table.7. Specification of UtraSonic Nebulizer WH-2000

Particlediamer	1-5 um and with 1 year manufacturer Warranty
Max nebulizing rate	> 2ml /min
Medicine cup capacity	50 ml
Setting of Nebulization time	Continuously or from 0 to 60 min for time setting
Product size (mm)	250 x150 x 225mm Suggested Application : Clinical, Nursing Home, Home Care

A.7. Digital Thermometer TP-101

Fig.11. TP101 digital thermometer

Specifications of TP101 digital thermometer

Measuring Temperature Range: -50-300 degree (-58-572 Fahrenheit)
Fit for your kitchen, laboratory, factory or BBQ
Stainless Steel Temperature Probe
Accurate temperature display
Low battery sensation and display
Measures in Fahrenheit or Celsius
Memorizes the last measuring data
Weight: 48g

A.8. Variac

.

Fig.12. Variac

Table.8. Specifications of Variac

Power	2 Amp- 300 Amp
Phase	Three Phase
Voltage	0 - 230 Volts
Usage/Application	Testing Purpose
Cooling Type	Dry Type/Air Cooled, Oil Cooled
Ambient Temperature	45 Degree Celsius Above Ambient
Input Voltage	230 Volts
Frequency	50 Hz
Output Voltage	0-270 Volts/ 0-300 Volts
Winding	Copper
Usage	Industry, Laboratory

A.9. Fluke 115 True RMS Multimeter

Fig.13. Fluke 115 True RMS Multimeter

Table.9. Specifications of Fluke 115 True RMS Multimeter

Maximum voltage (between any terminal and earth ground)	600 V rms
Safety	IEC 61010-1, Pollution Degree 2 IEC 61010-2-033 CAT III 600 V, 10 A EMC IEC 61326-1: Portable
Fuse for A input	11 A, 1000 V, IR 17 kA (Fluke PN 803293)
Display	Digital: 6,000 counts, updates 4/sec; Bar Graph: 33 segments, updates 32/sec
Temperature	
Operating	-10 °C to +50 °C
Storage	-40 °C to +60 °C
Humidity	0 % to 90 % to 35 °C; 75 % to 40 °C; 45 % to 50 °C
Temperature coefficient	0.1 x (specified accuracy/°C) (< 18 °C or > 28 °C)
Operating altitude	2,000 meters
Battery	9 Volt Alkaline (IEC 6LR61)
Battery life	400 hours typical, without backlight
Certifications	CE, CSA, RCM
IP rating (dust and water protection)	IP42

A.10. Rain Gauge

Fig.14. Rain Gauge

Table.10. Specification of rain gauge

Item Thickness	5.00 millimetres
Material	Plastic
Item Weight	600 g
Product Dimensions	12.7 x 12.7 x 30.5 cm

Appendix B

Intergraded circuits used for Data and Voice communication under different atmospheric conditions.

B.1. TL082 – OPAMP

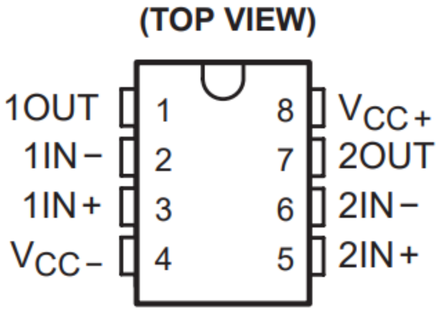

Fig.15. Top view of TL082

Table.2. Specifications of TL082

Internally Trimmed Offset Voltage	15 mV
Low Input Bias Current	50 pA
Low Input Noise Voltage	16nV/√Hz
Low Input Noise Current	0.01 pA/√Hz
Wide Gain Bandwidth	4 MHz
High Slew Rate	13 V/µs
Low Supply Current	3.6 mA
High Input Impedance	$10^{12}\Omega$
Low Total Harmonic Distortion	≤0.02%
Low 1/f Noise Corner	50 Hz
Fast Settling Time to 0.01%	2 µs

B.2. LM358 – OPAMP

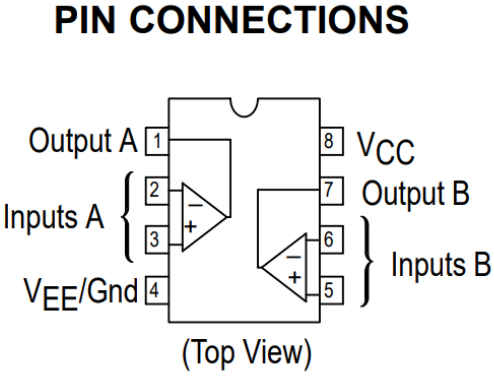

Fig.18. Top view of LM358

Table.3. Specifications of LM358

Total supply voltage (Max) (+5V=5, +/-5V=10)	32
Total supply voltage (Min) (+5V=5, +/-5V=10)	3
Rail-to-rail	In to V-
GBW (Typ) (MHz)	0.7
Slew rate (Typ) (V/us)	0.3
Vos (offset voltage @ 25 C) (Max) (mV)	7
Iq per channel (Typ) (mA)	0.35
Vn at 1 kHz (Typ) (nV/rtHz)	40
Operating temperature range (C)	0 to 70
Offset drift (Typ) (uV/C)	7
Input bias current (Max) (pA)	150000
CMRR (Typ) (dB)	80
Output current (Typ) (mA)	30
Features	Standard Amps

B.3. OP462 – OPAMP

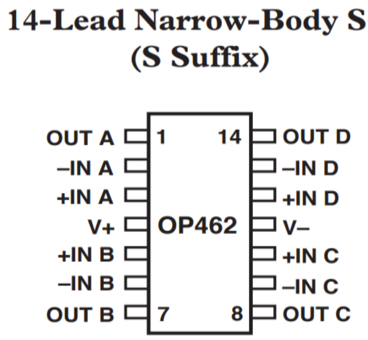

Fig.20. Top view of OP462

Table.4. Specifications of OP462

Wide Bandwidth	15 MHz
Low Offset Voltage	325 µV max
Low Noise	9.5 nV/$\sqrt{\text{Hz}}$ at 1 kHz
Single-Supply Operation	+2.7 V to +12 V
Rail-to-Rail	Output Swing
Low TCV$_{OS}$	1 µV/^{0}C typ
High Slew Rate	13 V/µs

B.4. LM393 – OPAMP

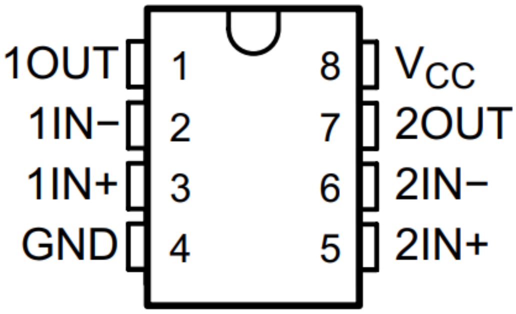

Fig.22. Top view of LM393

Specifications of LM393

- Maximum rating: up to 38 V
- ESD rating (HBM): 2k V
- Low input offset: 0.37 mV
- Low input bias current: 3.5 nA
- Low supply-current: 200 µA per comparator
- Faster response time of 1 µsec
- Extended temperature range for LM393B
- Available in tiny 2 x 2mm WSON package
- B-version is drop-in replacement for LM293, LM393 and LM2903, A and V versions
- Common-mode input voltage range includes ground
- Differential input voltage range equal to maximum rated supply voltage: ±38 V
- Low output saturation voltage
- Output compatible with TTL, MOS, and CMOS

B.5. L78L05ACZ – Voltage Regulator

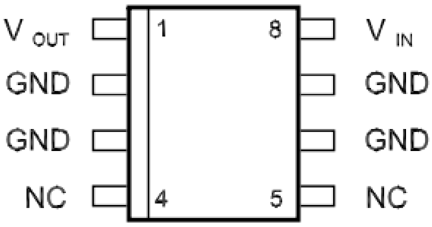

Fig.23. Top view of L78L05ACZ

Specifications of L78L05ACZ

- Output current up to 100 mA
- Output voltages of 3.3; 5; 6; 8; 9; 10; 12; 15; 18; 24 V thermal overload protection
- Short-circuit protection
- No external components are required
- Available in either ± 4% or ± 8%

B.6. BF256 – JFET

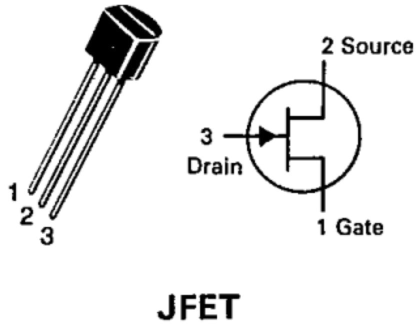

Fig.25. PIN diagram of BF256

Specifications of BF256

- Drain-Gate Voltage (Vdg): 30V.
- Gate-Source Voltage (Vgs): 30V.
- Gate-Source Voltage (Vgs-off): 8V.
- Drain Current (Idss): 18mA.
- Power Dissipation (Ptot): 350mW.
- Type: N-Channel.

B.7. CD4069 – Hex Inverter

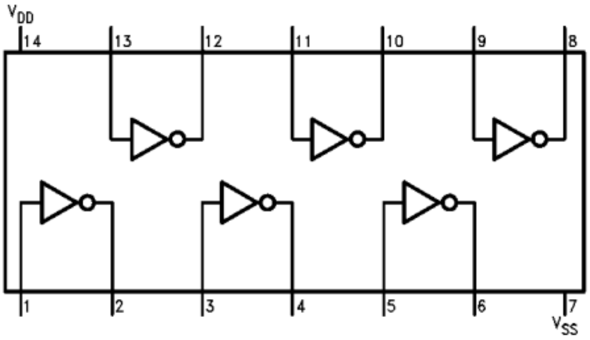

Fig.26. Pin configuration of CD4069

Specifications of CD4069

- Wide supply voltage range: 3.0V to 15V
- High noise immunity: 0.45 VDD typ.
- Low power TTL compatibility: Fan out of 2 driving 74L or 1 driving 74LS
- Equivalent to MM74C04

B.8. OP484 – OPAMP

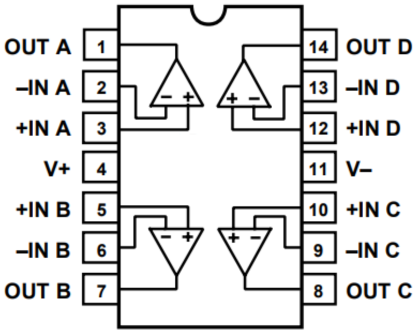

Fig.28. PIN configuration of OP484

Specifications of OP484

- Single-supply operation
- Wide bandwidth: 4 MHz
- Low offset voltage: 65 µV
- Unity-gain stable High
- slew rate: 4.0 V/µs
- Low noise: 3.9 nV/√Hz

B.9. FOD8001 – Optocoupler

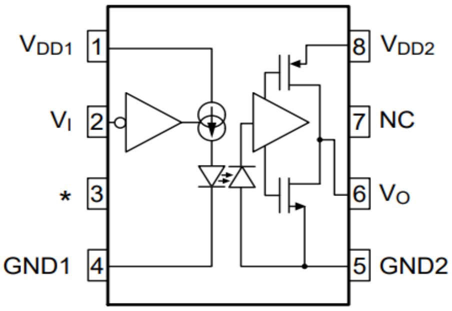

Fig.30. PIN configuration of FOD8001

Specifications of FOD8001

- High Noise Immunity characterized by Common Mode Rejection (CMR) and Power Supply Rejection (PSR) Specifications
  20 kV/s Minimum Static CMR @ Vcm = 1000 V
  25 kV/s Typical Dynamic CMR @ Vcm = 1500 V, 20 MBaud Rate
  PSR in Excess of 10% of the Supply Voltages across Full Operating Bandwidth
- High Speed:
  25 Mbit/s Date Rate (NRZ)
  40 ns max. Propagation Delay
  6 ns max. Pulse Width Distortion
  20 ns max. Propagation Delay Skew
- 3.3 V and 5 V CMOS Compatibility
- Extended Industrial Temperate Range, −40°C to 105°C Temperature Range
- Safety and Regulatory Pending Approvals:
  UL1577, 3750 VACRMS for 1 min.
  IEC60747−5−2 (pending)146

B.10. MIC4421 – MOSFET Driver

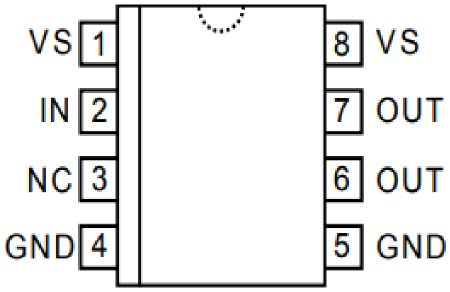

Fig.31. Pin configuration of MIC21

Specifications of MIC4421

- High peak-output current: 9 A peak (typical)
- Wide operating range: 4.5 V to 18 V (typical)
- Minimum pulse width: 50 ns
- Latch-up proof: fully isolated process is inherently immune to any latch-up.
- Input will withstand negative swing of up to 5 V
- High capacitive load drive: 47,000 pF
- Low delay time: 15 ns (typical)
- Logic high input for any voltage from 2.4 V to V_S
- Low equivalent input capacitance (typical): 7 pF
- Low supply current: 500 µA (typical)
- Output voltage swing to within 25 mV of ground or V_S

B.11. BSR202N – MOSFET

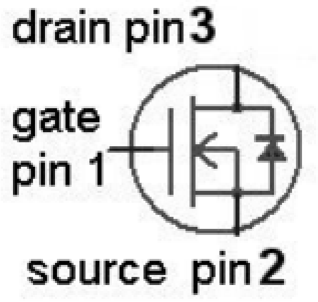

Fig.33. PIN configuration of BSR202N

Table.8. Specifications of BSR202N

C_{iss}	863 pF
C_{oss}	278 pF
I_D (at 25°C) max	3.8 A
I_{Dpuls} max	15.2 A
Operating Temperature	-55 °C to 150 °C
P_{tot} max	0.5 mW
Package	SC59
Polarity	N
Q_G (typ at 4.5V) max	5.8 nC
$R_{DS\ (on)}$ (at 4.5V LL) max	21 mΩ
$R_{DS\ (on)}$ (at 4.5V) max	21 mΩ
$R_{DS\ (on)}$ (at 2.5V) max	33 mΩ
$R_{DS\ (on)}$ max	21 mΩ
R_{thJA} max	250 K/W
V_{DS} max	20 V
$V_{GS(th)}$ min & max	0.7 V & 1.2 V

B.12. AD8039 – Voltage Feedback Amplifier

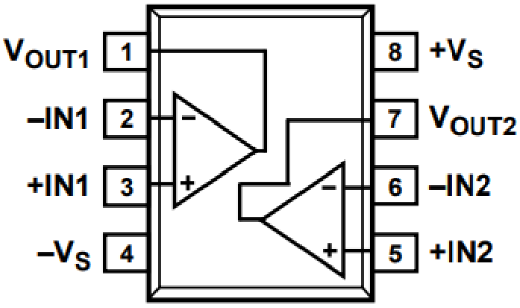

Fig.34. PIN configuration of AD8039

Specifications of AD8039

- Low power: 1 mA supply current/amp
- High speed
  350 MHz, −3 dB bandwidth (G = +1)
  425 V/µs slew rate
- Low cost
- Low noise
  8 nV/√Hz at 100 kHz
  600 fA/√Hz at 100 kHz
- Low input bias current: 750 nA maximum
- Low distortion
  −90 dB SFDR at 1 MHz
  −65 dB SFDR at 5 MHz
- Wide supply range: 3 V to 12 V

B.13. TL3016 – Ultra fast low-power precision comparators

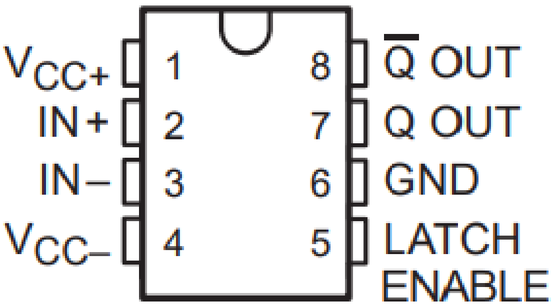

Fig.36. PIN configuration of TL3016

Specifications of TL3016

- Ultrafast Operation 7.6 ns (Typ)
- Low Positive Supply Current 10.6 mA (Typ)
- Operates from a Single 5-V Supply or from a Split ±5-V Supply
- Complementary Outputs
- Low Offset Voltage
- No Minimum Slew Rate Requirement
- Output Latch Capability
- Functional Replacement to the TL1016